Convective Cloud Parameterization

Evaluation of the mass-flux approach through observations

By

ALESSANDRO SAVAZZI

Department of Environmental Engineering
TU DELFT

Research conducted in collaboration with the School of Atmosphere and Environment at Monash University (Melbourne, Australia).

DECEMBER 2019

Assessment committee:
Prof. dr. Pier Siebesma (chair)
Prof. dr. Christian Jakob
Dr. Louise Nuijens
Prof. dr. ir. Herman Russchenberg

Abstract

In the context of climate modelling, convective clouds in tropical regions play a major role in determining the climate sensitivity. The vertical transport of mass and energy associated with this type of clouds is often represented with so called mass-flux parameterization schemes. In this work the aim is to evaluate the relationship between mass-flux and large scale environmental conditions using observations in a tropical region, over a period of 13 wet seasons. A uniquely comprehensive data set from the C-band polarimetric radar (CPOL) in Darwin, Australia, is used to estimate vertical velocity inside precipitating convective clouds. Ultimately, mass-flux is derived over a domain size similar to that of a general circulation model (GCM) grid box. Five parameters (RH_{500}, CAPE, CIN, Ω_{500} and $\overline{\chi_{\text{crit}}}$) are selected to describe environmental conditions and with these, the magnitude and shape of mass-flux is analysed. $\overline{\chi_{\text{crit}}}$ appears to be the most valid parameter to represent both the shape and magnitude of mass-flux. All other selected parameters strongly influence only one of the two aspects of the profile. Additionally, fractional entrainment is retrieved from mass-flux profiles and partitioned into two terms: one dependent on area fraction and the other on vertical velocity. Under all environmental conditions, the layer between 4.5 and 7 km experiences detrainment. It can be inferred that a stable layer, known as the freezing level, is present at 4.5 km. Below the freezing level, the vertical velocity and the mass-flux shape are most relevant to determine entrainment rates leading to the conclusion that the vertical velocity should not be disregarded when parameterizing convection.

ACKNOWLEDGEMENTS

"Non sum tam ingratus ut non intellegam quid mihi praestiteris quom cotidie in viam me veram inducere et oculos aperire".
"I am not so ungrateful not to understand the help you gave me when you daily put me on the right path and opened my eyes".
Fronto. Marcus Cornelius Epistulae ad Caesarem 3.19

I am deeply thankful to all who helped me during this long journey.

Prof. dr. Christian Jakob, your extraordinary support, the precious data and resources you made available, allowed me to embrace this challenging project with confidence and ambition. I am tremendously grateful.

Prof. dr. Pier Siebesma, thank you for your wise, inspiring and constant guidance. Your approachability and enthusiasm made the learning process pleasant and productive.

Dr. Louise Nuijens, for proposing interesting variations to the methods and suggesting, in a clear manner, a way to add details to the research. Thank you.

Prof. dr. ir. Herman Russchenberg, your critical point of view was crucial to ensure a good quality of the work. Thank you.

The reciprocal support of all my fellow students made working on this project pleasant and fun. Thank you Ashwini, Manuel and Pooja for making, not only the final eight months but, the entire two years of study an amazing journey.

Thanks to my family on whom I have relied during emotionally hard times. You made sure this work was not affected by any imbalance within different aspects of my life.

Thank you all.

Table of Contents

List of Tables

List of Figures

CHAPTER 1

INTRODUCTION AND MOTIVATION

Convective clouds arise as a result of the destabilising effects of warming and moistening of the near-surface layer. Rising moist air that originates in the lower part of the troposphere (boundary layer) can undergo condensation with associated release of latent heat. In favourable circumstances, this can make rising air parcels or streams of air buoyant with respect to the environment and gives rise to cumulus clouds. Turbulent transport processes associated with these type of clouds are considered to be of primary importance for the distribution of energy in the atmosphere at local and global scales (Arakawa, 2004). For this reason current General Circulation Models (GCMs) try to account for it.

Climate models are mathematical, simplified representations of the climate system and they are widely employed for projecting climate change. They are also extremely valuable for understanding complex mechanisms governing the atmosphere and for testing theories and solutions. However, models are dependent on the available knowledge of atmospheric processes and they can only take into account what has been included by the developer. Models are subject to numerical approximations and they will always be simplifications of reality.

The general scope of many studies, in the field of atmospheric convection, is to unveil and understand environmental mechanisms, in order to gain insights on how convective clouds form and in turn, improve their representation in models.

One of the greatest limitations of atmospheric and climate models is the inability to fully represent and solve physical processes with dynamics smaller than the model' spatial resolution. Convective transport of energy, humidity and mass from low to high levels of the atmosphere are examples of processes often occurring at spatial scales not captured by GCMs grid sizes.

Modellers have to rely on simplified parametric equations to include the overall effect of narrow and vertical convective processes into numerical weather predictions (NWPs).

Parameterization schemes make use of simplified equations: functions of resolved prognostic variables. In principle, conceptual equations used in parameterization should have a physical basis and support from observational studies. Ideally, they would be derived from basic relations by a well-defined limit process, but this degree of mathematical rigor is rarely possible in practice (Mcfarlane, 2011). The application of simplified or idealised models usually gives rise to a number of quantities that are not known, therefore, may need to be determined empirically or through 'closure' assumptions. When the appropriate conceptual model is hard to find, empirical relationships derived from observations or process studies are exploited for parameterization. Current convective cloud parameterizations schemes often result in far too large uncertainties (Shutts and Pallarés, 2014).

Solid scientific understanding of the physical processes linked to convective cloud formation and dynamics is essential to build a reliable and accurate parameterization.

This need drives the current research. Here, the vertical mass-flux inside precipitating convective clouds over a large domain in the tropical region of Darwin (Australia) is an analysed. A validity check of the state of the art is performed and new relationships with large scale conditions are investigated. The use of an extensive observational radar data set constitute one of the strengths of this work.

1.0.1 Subgrid-scale representation problem

An ever increasing computational power allows to increase the spatial resolution of models without having to reduce their domain size. Despite this, it is still difficult to imagine a GCM with grid size able to capture narrow convection.

The Subgrid-Scale Representation (SSR) problem can be seen as made of two parts: downscaling and parameterization. The first is a retrieval of details of the subgrid-scale processes, the second is an estimation of the feedbacks of the subgrid-scale processes onto the resolved scale. Downscaling and parameterization schemes are often developed separately although they are part of the same problem (Yano, 2010). Small scale processes can affect the global atmospheric dynamics but local scale features are also affected by the larger conditions (Rockel, 2015).

In the past decades numerous research studies aimed at developing simple parameterizations to describe the mean effect of small scale processes as a function of larger scale quantities and empirical parameters. In recent years, a growing number of studies have made use of the so called super-parameterization technique. This framework was first introduced by Khairoutdinov

and Randall (2001) following a research from Grabowski and Smolarkiewicz (1999).

The main idea behind a super-parameterization is the coupling of a two dimensional cloud system-resolving model to an atmospheric GCM. This offers a compromise between a coarse resolution GCM with traditional parameterizations and a global cloud-resolving GCM. Super-parameterization is promising but is not free of limitations. It is substantially more computationally expensive than a conventional GCM. Furthermore, it shows biases and unrealistic features such as excessive precipitation in tropical regions due to overestimation of convective columns.

Conventional parameterization techniques are still largely needed and employed to represent the effect of convective clouds. Resources should be allocated to improve the physical understanding of convective processes and accordingly refine their parameterizations.

1.1 Outline

In the next chapter (Chapter 2) some background knowledge and the state of the art literature on which this work sets its basis are explained. Chapter 3 reports the specific goals of the research. The description of study area and available data (Chapter 4) is kept separate from a detailed explanation of the methods, assumptions and limitations (Chapter 5). Results are presented and analysed in Chapter 6 and a comparison with the literature is completed separately in Chapter 7. Lastly, Chapter 8 addresses the main conclusions and recommendations.

CHAPTER 2

LITERATURE

The present thesis strongly relies on works by Kumar et al. (2015, 2016), for this reason it is crucial to understand and show the methods of these articles. In a context of ever improving knowledge, it has to be noted that assumptions and approximations of these works will have an impact on the results of the present thesis. Nevertheless, one of the goals is to help identifying weak points of previous research and suggest improvements.

The Department of Earth, Atmosphere & Environment at Monash University is already investigating and testing the validity of the results shown by Kumar et al. (2015, 2016) using machine learning techniques.

2.1 Background

2.1.1 Mass-flux

It has long been recognised that organised deep convective systems play a key role in regulating the large scale circulations and thermal structure of the atmosphere in tropical oceanic regions (de Rooy et al., 2008; Labbouz et al., 2018). Despite this, the underlying physical processes connected to convective clouds and their response to a warmer climate are yet not clear.

Cumulus convection organises into strong narrow updrafts which cover a small horizontal fraction of the atmosphere. When a cumulus cloud becomes sufficiently high to sustain intense precipitation, strong saturated downdraft can also occur and, sometimes, result in so called cold pools (Whiteman et al., 2004).

Before 1969, convection parameterizations were convective adjustment schemes: when air becomes oversaturated cumulus convection acts to bring temperature back to its saturated profile and the excess moisture is removed through precipitation. In 1969 a new cumulus convection parameterization was introduced by Akio Arakawa and then further improved in 1974 (Arakawa et al., 1974). It is known as the mass-flux parameterization and it describes how cumulus clouds modify the environmental properties while condensation takes place only inside the clouds.

For a simple description, the cumulus parameterization can be seen as the combination of a representation and closure assumptions. The representation makes use of conceptual models, such as the simplified entraining plume model, and often involve undetermined quantities (parameters). The closure problem is to determine these parameters in terms of the resolved prognostic variables, the assumptions used to solve the closure problems are particularly critical in cumulus parameterization and are constantly been tested. (Mcfarlane, 2011).

The mass-flux parameterization is based on three main assumptions. First, the fractional area covered by convection is considerably smaller than the total grid box area. Second, the fluctuations of a generic variable ϕ within the convective plumes and the environment are negligible compared to the difference between the convective and environmental averages of ϕ (top-hat approximation). Third, the averaged grid box vertical velocity is negligible compared to the vertical velocities within the convection.

The mentioned assumptions and approximations allow to write the turbulent flux of ϕ as

$$\rho\overline{w'\phi'} \approx \rho A_c w_c(\phi_c - \overline{\phi}), \tag{2.1}$$

where the subscript c indicates convection properties, ρ is the air density, A_c the area fraction covered by convection and w_c the vertical velocity inside the convection.

Defining the mass-flux by convection (M_c) as

$$M_c \equiv \rho A_c w_c, \tag{2.2}$$

Equation 2.1 becomes

$$\rho\overline{w'\phi'} \approx M_c(\phi_c - \overline{\phi}). \tag{2.3}$$

In light of this equation, it is possible to explain the closure problem of convection as the process of determining M_c without having to define A_c or w_c. To solve the closure problem of convection,

large scale parameters are used to describe mass-flux.

Standard commonly used bulk mass-flux schemes (Tiedtke, 1989; Bechtold et al., 2001; Kim and Kang, 2012) do not explicitly represent the spectrum of convective clouds but aim to represent its collective effect on the large scale through gridbox-mean mass-fluxes with height-dependent entrainment and detrainment rates. A common purpose of bulk models is to reduce complexity. More ambitious decomposition of the basic mass-flux model presented above are possible. For example, in contrast to Equation 2.3 referred to as bulk mass-flux model, a spectral mass-flux model can be defined as follows:

$$\rho\overline{w'\phi'} \approx \sum_{i}^{n} M_{\mathrm{c},i}(\phi_{\mathrm{c},i} - \overline{\phi}), \tag{2.4}$$

where the cloud ensemble is divided into n sub-ensembles of clouds labelled by the subscript i. These are often obtained by grouping convective cells (clouds) according to their height, an example is the definition of four cumulus cloud modes given by Kumar et al. (2013): shallow cumulus, congestus, deep convective and overshooting convective. Spectral convective parameterizations aim at representing a population of convective clouds in a deterministic (Arakawa et al., 1974; Moorthi and Suarez, 1992; Wagner and Graf, 2010; Yoshimura et al., 2015) or stochastic way (Plant and Craig, 2008).

2.1.2 Entrainment and detrainment

It is hard to believe that a convective plume rises without any mixing with the environment. This exchange of properties takes the name of entrainment, when environmental air becomes part of the turbulent flow, and detrainment, when air from a convective cloud is injected into the environment. Current convection schemes commonly include parameterizations of entrainment and detrainment with different ranges of complexity.

In general, it is possible to analytically understand the entrainment (detrainment) process with the continuity equation. Considering two horizontal planes infinitely close to each other and naming the mass-flux across the first plane M_1 and the mass-flux across the second plane M_2, for the continuity equation:

$$M_2 = M_1 + \frac{\partial M_1}{\partial z} dz, \tag{2.5}$$

where dz is the distance between the two planes. It is evident that any change of mass-flux in the vertical direction involves a lateral inflow or outflow (entrainment or detainment). It is then possible to define the overall mixing process as:

$$\frac{\partial M_c}{\partial z} = E - D, \tag{2.6}$$

where E refers to the effective entrainment rate and D to the effective detrainment rate. The right hand side of the equation is positive if entrainment (E) dominates over detrainment (D), negative if detrainment controls the net effect. In Equation 2.6 the two complementary mixing processes are defined together to underline the coexistence of entrainment and detrainment and the difficulties in measuring them separately.

More conveniently, mass-flux parameterizations make use of slightly different quantities for the entraining plume model: fractional entrainment (ϵ) and fractional detrainment (δ).

$$\epsilon \equiv \frac{E}{M_c}, \qquad \delta \equiv \frac{D}{M_c}. \tag{2.7}$$

Accurate observations of entrainment and detrainment are difficult to attain, an example of field campaign with aircraft is given by Warner (1955) but more quantitative descriptions of the processes come from water tank experiments (Morton et al., 1956).

In 1951 Houghton and Cramer (1951) firstly made a further distinction and introduced the terms dynamical entrainment (or detrainment) and turbulent entrainment (or detrainment). The first (ϵ_{dyn} or δ_{dyn}) caused by large scale organised flow and mainly occurring at cloud base or cloud top, the second (ϵ_{turb} or δ_{turb}) driven by turbulent mixing at the cloud edge. The change of mass-flux with height (or net fractional entrainment) can then be written as:

$$\frac{1}{M_c}\frac{\partial M_c}{\partial z} = \epsilon_{\text{dyn}} + \epsilon_{\text{turb}} - \delta_{\text{dyn}} - \delta_{\text{turb}}, \tag{2.8}$$

where $\epsilon = \epsilon_{\text{turb}} + \epsilon_{\text{dyn}}$ and $\delta = \delta_{\text{turb}} + \delta_{\text{dyn}}$. Equation 2.8 implies that the shape of the mass-flux is entirely determined by entrainment and detrainment processes. It can be further argued that the turbulent processes are not relevant to the shape of M_c since ϵ_{turb} and δ_{turb} are symmetric.

2.1.3 Vertical gradient of mass-flux

As showed by de Rooy et al. (2008), a good representation of detrainment can be more important than its counterpart for obtaining realistic mass-flux profiles in cumulus convection. This is in line with the results from research stating the greater importance of area fraction compared to vertical velocity in determining the mass flux (Kumar et al., 2015). From Equation 2.2 follows that the normalised derivative of mass-flux can be written as the sum of two components.

$$\frac{1}{M}\frac{\partial M}{\partial z} = \frac{1}{A}\frac{\partial A}{\partial z} + \frac{1}{\rho w}\frac{\partial(\rho w)}{\partial z}. \tag{2.9}$$

While the first term on the right hand side of Equation 2.9 is controlled by the area fraction profile, the second is controlled by the vertical velocity profile. Under the assumption of monotonically decreasing cloud size, the first term on the right hand side of 2.9 is always negative (always detraining). The second term on the right hand side can be positive or negative (entraining or detraining). de Rooy et al. (2008) also showed that, in shallow convective clouds, the mean fractional detrainment rate is mainly influenced by cloud height and by the critical fraction of environmental air needed to make a rising air parcel neutrally buoyant (χ_{crit}).

2.2 Methodology in previous studies

An evaluation of cumulus mass-flux schemes through a zeroth-order observational reference is conducted by Kumar et al. (2015). Using observations from two wind profilers and a weather radar (CPOL), the study derives convective mass-fluxes and their constituent on a GCM scale. Kumar et al. (2015) make use of an algorithm described by Williams (2012) to derive vertical velocity from dual-frequency profilers. One wind profiler (50-MHz) measures simultaneously Bragg and Rayleigh scatter, the outcome vertical velocity includes signals from air parcels and hydrometeors. A second wind profiler (920-MHz) is mainly sensitive to hydrometeors and is used to remove Rayleigh echo returns from the spectra of the first profiler. The filtered air parcel's vertical velocity is then processed according to Carter et al. (1995). This technique is applied to a data set of two wet seasons (2005/06 and 2006/07) collected in Darwin, Australia. A time-space conversion is finally used to study mass-flux at GCM grid box scale. This last conversion relies on the assumption that convection at a point derived from a long time series is a good sample of that occurring in the entire domain over the same sampling time. In their work, Kumar et al. (2015) determined convective area fraction as the ratio between the times CPOL identifies convection above the profiler and the total sampling time.

A second study from Kumar et al. (2016) puts forward an empirical equation to retrieve vertical velocity inside convection from radar measurements and to produce quantitative estimates of mass-flux. Wind profilers are only used to evaluate the estimates. This second study explores the feasibility of the method and also gives some insights on the role of mass-flux components: area fraction and vertical velocity. Using the same data set as in Kumar et al. (2015), in combination with reflectivity measurement from the CPOL radar in Darwin, this second study finds the 0-dBZ echo top height (ETH) to be a good proxy for cumulus modes and uses it to parameterize vertical velocity inside convection. The large variability in column mean velocity within each cumulus mode is then taken into account through a height weighted sum of reflectivity: Z_{HWT}. This parameter is chosen among others because it is related to where the convective cell is in its life cycle and because it has the highest correlation with vertical velocity over the 0-dBZ ETH range.

2.2.1 Parameterized vertical velocity profiles

A parametric equation of vertical velocity which separates the contribution of updrafts (w_{U}) from downdrafts (w_{D}) inside convection is proposed by Kumar et al. (2016). The total vertical velocity reads

$$w(z) = w_{\mathrm{U}}(z) T_{\mathrm{z}}(z) + w_{\mathrm{D}}(z), \tag{2.10}$$

where z is the vertical coordinate and the parameter T_{z} is a dimensionless quantity, function of Z_{HWT} and it is used to add variability to w_{U}, mimicking storm development.

w_{U} and w_{D} are obtained applying a least squares fit to the mean updraft and downdraft profiles measured by the wind profilers. In the first case the method is used separately for three cloud modes: congestus, deep and overshooting resulting in the following equation.

$$w_{\mathrm{U}}(z) = \begin{cases} 0.404z + 0.9922, & \text{for congestus} \\ -0.0016z^4 + 0.0519z^3 - 0.571z^2 + 2.7z - 2.7351, & \text{for deep} \\ -0.0454z^2 + 1.0889z - 0.8963 & \text{for overshooting} \end{cases} \tag{2.11}$$

While the downdraft is represented sufficiently well by a single equation for all cloud modes and for all values of Z_{HWT}.

$$w_{\mathrm{D}}(z) = 0.0339z^2 + 0.4109z - 1.6852. \tag{2.12}$$

Less trivial is the formulation of T_{z}. This parameter is expressed through a residual vertical velocity (w_{res}) which is the difference between vertical velocity measured by wind profilers and vertical velocity derived using Equation 2.10 with $T_{\mathrm{z}} = 1$. w_{res} appears to be linearly related to Z_{HWT} and the slope of the linear fit increases with 0-dBZ ETH. The y intercepts is also related to 0-dBZ ETH so that w_{res} is modeled as follow:

$$w_{\mathrm{res}} = a + bZ_{\mathrm{HWT}}, \tag{2.13}$$

with $a = 4.3911 - 1.2381\mathrm{ETH}$ and $b = -0.06064 + 0.02095\mathrm{ETH}$.

An additional factor plays a role in defining T_{z}, this mimics the joint increase in magnitude and height of the updraft velocity peak with increasing Z_{HWT}. T_{z} is finally defined as

$$T_{\mathrm{z}}(z) = \left(\frac{w_{\mathrm{res}} + \overline{w_{\mathrm{U}}}}{\overline{w_{\mathrm{U}}}} \right) \left(\frac{w_{\mathrm{U}}(z)^{0.5}}{\overline{w_{\mathrm{U}}}^{0.5}} \right). \tag{2.14}$$

Figure 2.1, retrieved from Kumar et al. (2016), shows profiles of mean updraft and downdraft vertical velocity associated with different cumulus cloud modes. The black lines refer to the wind profiler measurements, while the red lines to the parametric equation (Equation 2.10).

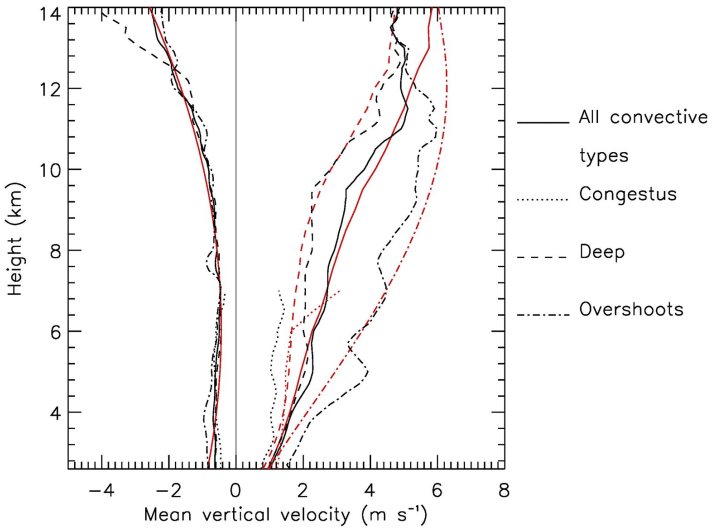

FIGURE 2.1. Figure retrieved from Kumar et al. (2016). Mean vertical velocity from 246 10-min convective profiles observed by wind profilers (black lines) and mean velocity profiles modeled with Equation 2.10 (red lines).

A comparison of the mass-flux (not shown here) obtained using vertical velocities from wind profilers and mass-flux obtained with the parametric equation shows a slight overestimation in congestus clouds for the parametric approach. The best performance is registered between 8 and 12 km from the surface.

2.3 Results in previous studies

2.3.1 Mass-flux and its components

Results from Kumar et al. (2015) show a dominant role of area fraction compared to vertical velocity in regulating mass-flux: a strong reduction of total mass-flux above 8 km is relatable to the reduction in area fraction. The authors also mention an exception to this finding at low levels. They point out that in-cloud vertical velocities are significant for cloud depth and that the increase in vertical velocity combined with a small decrease in area fraction produces an increase of mass-flux between 2 and 5 km.

Another relevant study (Giangrande et al., 2016) explores convective vertical velocity, area fraction and mass-flux in a tropical area and tries to give insights to improve GCM convective

parameterization. Their data set comes from the Observations and Modeling of the Green Ocean Amazon (GoAmazon2014/5 field campaign) and shows similar results to the one presented by Kumar et al. (2015). Giangrande et al. (2016) also investigate the role of updrafts and downdrafts: updrafts and downdrafts are found to increase in magnitude with height to the mid-levels.

2.3.2 Large scale conditions and cumulus convection

Understanding the role played by environmental conditions in determining the convective mass-flux is of crucial importance for an effective parameterization of the latter. Previous studies have investigated this relationships in the tropics. An example is given by Kumar et al. (2015). The already mentioned work uses CAPE, CIN, column mean relative humidity between 0 and 5 km and large scale vertical motion at 500 hPa to examine the relationship between environmental condition and updraft mass-flux, area fraction and vertical velocity.

- Small differences are observed between mass-flux profiles occurring under strong CAPE and the one observed with low CAPE. Low CAPE are associated with higher area fractions but shallower clouds. Weaker vertical velocity are also registered with low CAPE.
- The large difference in mass-flux between large and small values of CIN is mainly caused by area fraction. CIN is, indeed, a predictor of the existence of convection rather than of its strength.
- Large differences are exhibited between dry and moist conditions. When RH is high, smoother and deeper mas-fluxes are registered. Dry environments are associated with small area fractions but stronger velocities. Under this condition stronger updrafts are needed to penetrate through the dry atmosphere.
- Large scale vertical motion is mainly influencing the existence of convection. The few convective systems occurring with strong downward motion have strong vertical velocities at high levels and very small area fractions.

The weak relationship between CAPE and convection had been already noticed by Davies et al. (2013). In their study, also based on the Darwin area, convection is taken into account in terms of precipitation rate. Davies et al. (2013) also point out a great dependency of the area covered by precipitation to environmental conditions, in particular moist convergence and mid-level vertical motion. Strong relationships with variables related to stability, such as CAPE, are neither found with convective precipitation area nor with convective precipitation intensity. Nevertheless, this does not imply that vertical velocity is not relevant for any other characteristics of convection.

A final relevant study, which builds up from most of the above mentioned, is a work from Louf et al. (2019a). One of its strength is the extensive data set, spanning over 13 wet seasons

in the tropical area of Darwin. According to Louf et al. (2019a), the division of convective area fraction into cell number and cell area, provides additional insight to convective behaviour. The largest area fractions are achieved when there is a moderate number of cells of moderate size in the domain.

2.3.3 Critical fraction of environmental air

It is mentioned above that convective cloud parameterization should account for the influence of environmental conditions. Nevertheless, many schemes infer lateral mixing between cloud and the environment through constant values of entrainment and detrainment. (Morton et al., 1956). Not only the mass-flux as such is dependent on large scale conditions but its rate of change with height is too (de Rooy et al., 2008).

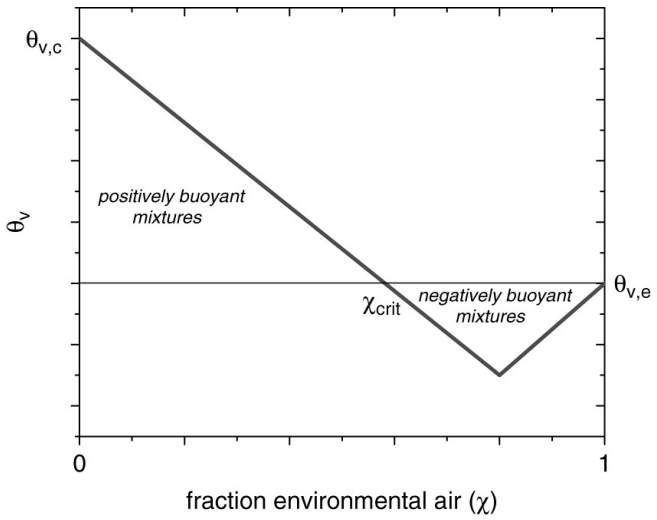

FIGURE 2.2. Figure retrieved from de Rooy et al. (2012). Virtual potential temperature of a mixture of cloudy and environmental air as a function of the fraction, χ, of environmental air. $\theta_{v,c}$ and $\theta_{v,e}$ are virtual potential temperature of cloudy and environmental air respectively. χ_{crit} is the fraction of environmental air needed to make the mixture neutrally buoyant.

Kain et al. (1990) firstly introduced the buoyancy sorting concept to entrainment parameterization in order to take into account environmental conditions. The fundamental assumption of their one-dimensional entraining/detraining plume (ODEDP) model is that any mixture that becomes negatively buoyant detrains from the cloud while mixtures that remain positively buoyant entrain into the cloud. Negatively buoyant mixtures can occur due to evaporative cooling and are characterised by values of virtual potential energy (θ_v) lower than the virtual potential energy of purely environmental air ($\theta_{v,e}$). Figure 2.2 sketches θ_v as a function of the fraction, χ, of environmental air in the mixture. χ_{crit} is the threshold between positively and negatively

buoyant mixtures.

Figure 2.2 suggests that the detrainment rate increases with decreasing values of χ_{crit} and this has been confirmed with large scale eddy simulations (Böing et al., 2012). Analytical expressions of χ_{crit} (see Appendix A) proposed by de Rooy et al. (2008) further suggest that χ_{crit} increases with a more unstable atmosphere and with increasing humidity. Large values of $\Delta\theta_{\mathrm{v}}$ ($\Delta\theta_{\mathrm{v}} = \theta_{\mathrm{v,c}} - \theta_{\mathrm{v,e}}$) and RH usually support strong cloud updrafts with large vertical extent and small detrainment rates (i.e. small decrease of mass-flux with height). Although χ_{crit} was introduced to link entrainment to the mean environmental conditions, a clear relationship between the two is far from being established.

2.4 Knowledge gaps

Tropical regions are subjects to numerous studies about precipitating convection because of the great occurrence of these systems at low latitudes. Nevertheless, long observational data sets are difficult to find and large part of the theoretical knowledge comes from model results. Furthermore, the analysis of mass-flux inside convection is hardly conducted with a clear distinction between shape and magnitude of the profile.

To the author's knowledge, this is the first study where mass-flux estimates spanning over 13 wet seasons are analysed in relation to the environmental condition. In particular it is hard to find relevant literature where the parameter χ_{crit} is used to characterise the atmosphere and where its relationship with mass-flux is investigated.

The current work also presents the probability distribution of fractional entrainment at the tropics between 2.5 and 13 km. For the first time, this is obtained from profiles of mass-flux retrieved from measurements and it is decomposed in two components, in order to improve the limited knowledge about the role of area fraction and vertical velocity to entrainment processes.

CHAPTER 3

PROBLEM STATEMENT AND OBJECTIVE

Previous chapters showed how convective cloud parameterization is far from being satisfactory and how a reduction of its uncertainties is needed to improve climate (and weather) models. Limited amount of studies based on observations and difficulties in measuring properties inside convection (e.g. vertical velocity and lateral mixing) are among the main reasons why the understanding of convective processes improves slowly.

The first step and objective of this research is to produce, through radar measurements, a long term, observational data set of convective mass-flux over an area relevant to the parameterization of convection in GCMs.

The second, broader aim of the study is to provide a reliable and in depth analysis of the relationship between environmental condition and mass-flux starting from observed values of mass-flux and using an inverse modelling approach.

The vertical mass-flux is analysed in relation to some of the most common environmental properties and the results are used to understand convection in tropical regions. In order to achieve this goal, magnitude and shape of bulk profiles are investigated separately in relation to RH, CAPE, CIN, Ω and χ_{crit}. Furthermore, the relative importance of area fraction and vertical velocity is investigated to improve the general understanding of mass-flux and its components.

The reason for decoupling magnitude and shape of mass-flux profiles is to learn about some of the parameters involved in current convective parameterization, namely entrainment and detrainment. For this purpose, the quantity $\frac{1}{M}\frac{\partial M}{\partial z}$ is used to determine altitudes and conditions

where entrainment dominates over detrainment or vice versa.

The goal of this thesis can be divided into sub-questions and intermediate objectives. Here is a summary list:

- Evaluate and further investigate the state of the art knowledge regarding the role of large scale forcing and meteorological conditions on in-cloud mass-flux.
- Test the relationship between the parameter χ_{crit} and mass-flux.
- Separately investigate mass-flux magnitude and shape and determine which of the two is more dependent on environmental conditions.
- Characterise mass-flux shape through mass-flux components: area fraction and vertical velocity.
- Find a link between the shape of mass-flux and the entrainment process.
- Investigate the relative importance of different cloud modes to the overall mass-flux.

CHAPTER 4

STUDY AREA AND DATA

4.1 Darwin region

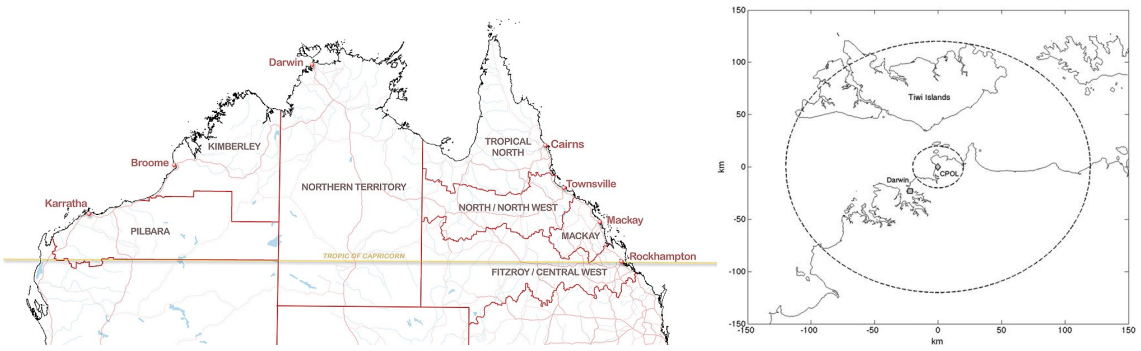

FIGURE 4.1. Study area.

The city of Darwin (12°26S, 130°50E) is the capital of the Northern Territory in Australia, is situated on the Timor Sea and is the most northerly of all the Australian capital cities. It experiences a tropical climate with a dry and a wet season, the latter typically starts in late November or early December and lasts until late April. Wet season brings with it heavy monsoonal downpours and cyclone activity. In this period, average temperatures range from 25 to 32 °C and humidity can become greater than 80%. Over the wet season a wide variety of convective systems can be observed in the greater Darwin region. The annual average rainfall is about 1,690 mm with the wettest month being January, with an average of 426 mm. For comparison, in The Netherlands the mean annual precipitation is about 800 mm and the wettest month is October with an average of 88 mm of precipitation. (En.climate-data.org, 2012).

The area of Darwin is unique for its complex terrain and topography of coastlines, islands and oceanic areas. Convective systems can be observed on land or over the ocean and the effect of land cover on cloud formation and development can be studied. (Kumar et al., 2012; Davies et al., 2013). These facts, together with the availability of a comprehensive long-term observational record, make the Darwin region an ideal location to investigate the relationships between convective activity and large-scale meteorological condition.

4.2 Data

The present work relies on two data sets, the first obtained from radar measurements and the second from variational reanalysis of a numerical weather prediction (NWP). These are described in the next sections.

4.2.1 CPOL data set

Information inside convective cells are derived from a C-band Dual- Polarization radar (CPOL) located at Gunn Point (-12°25' S; 131°05' E), about 25 km northeast of Darwin International Airport (Keenan et al., 1998). CPOL is a Doppler radar, working at a frequency of 5.6 GHz with a pulse repetition frequency of 1000 Hz (i.e. a maximum range of 150 km) and a beam width of 1°. It performs a set of scans with an update time of 10 min (Kumar et al., 2012).

The CPOL data set underwent recently a series of calibration, quality control, and processing that are described in details in Louf et al. (2019b). These pre-processing phase results in a data set with spatial domain of 70.000km^2, temporal resolution of 10 minutes and temporal domain of 13 years: from 26-10-2001 to 14-4-2015 with one year of gap in 2008. The CPOL radar provides information only during the wet season because of the greater amount of convective systems.

In this study, all parameters associated with the CPOL data set are derived from the reflectivity profiles ($Z(z)$). The reflectivities obtained from CPOL are interpolated onto a cubic grid with horizontal grid size of 2.5 km × 2.5 km and a vertical grid size of 0.5 km. The first measurement is taken at 2.5 km from the ground and the last measurement used is at 13.5 km.

From the radar reflectivities three parameters are attained and made available for this study: convective-stratiform classification, 0-dBZ echo-top height (ETH), height-weighted column reflectivity index (Z_{HWT}).

Convective-stratiform classification

The Steiner algorithm (Steiner et al., 1995) is used to partition the radar pixels and identify the convective ones at 2.5 km. The whole vertical profile is then assigned the same classification as that at the base. Reflectivities from cirrus anvils above the convective towers are filtered out. The Steiner algorithm has already been successfully employed in previous studies (Kumar et al., 2013; Penide et al., 2013) and its output is not questioned here. Figure 4.2 shows the domain area covered by a radar scan and the output of the Steiner classification at 2.5 km for the date 07-12-2010 09:30. The yellow colour shows areas with convection, green highlights stratiform clouds and the purple is for clear sky.

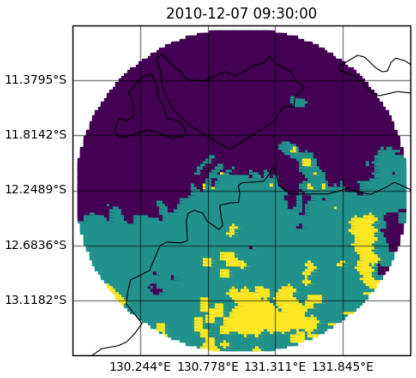

FIGURE 4.2. Output of Steiner classification algorithm applied at 2.5 km from the surface on the instance of time 07-12-2010 09:30. Yellow pixels are convective, green pixels are stratiform, purple pixels are of clear sky or not defined cloud cover.

0-dBZ echo-top height

The 0-dBZ ETH (or ETH for brevity) corresponds to the height where the reflectivity is the closest to 0 dBZ with the requirement that there is vertical continuous signal between 2.5 km and the 0-dBZ ETH. This height coincide with the highest level at which precipitation occurs. Studies have shown that, for cumulus clouds, the 0-dBZ ETH from C-band radars are usually within 1 km from cloud tops estimates by ground (Darwin) and spaceborne (CloudSat) millimetre cloud radars (Casey et al., 2012; Kumar et al., 2013). In this work the ETH is also used to classify convective cells as congestus, deep or overshooting as done by Kumar et al. (2013, 2014, 2015, 2016) and explained in Chapter 5. In Figure 4.3 the 0-dBZ ETH of convective pixels is shown for the same instance of time used in Figure 4.2. Pixels classified as not-convective are filtered out.

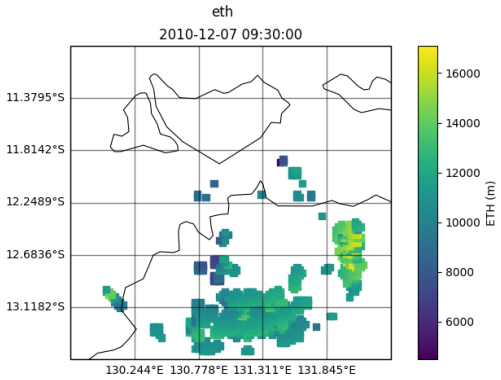

FIGURE 4.3. 0-dBZ echo top height over the domain area for the instance of time 07-12-2010 09:30. Only pixels classified as convective at 2.5 km are shown.

Height-weighted column reflectivity index

Thanks to its high correlation with vertical velocity, the height-weighted column reflectivity index (Z_{HWT}) is chosen by Kumar et al. (2016) to parameterize the variability of vertical velocity profiles in convective clouds. Z_{HWT} is defined as follow:

$$Z_{\mathrm{HWT}} = 10log\sum Z(z)z, \tag{4.1}$$

where z is in kilometres. Compared to a simple sum of reflectivities over the whole column, this index allows for the ice part of the reflectivity profile to contribute more.

The starting point of the CPOL data set is summarised in the Table 4.1, which refers to an ideal instance of time.

Table 4.1: Initial data set for an hypothetical instance of time.

Longitude	Latitude	Convective classification	0-dBZ ETH	Z_{HWT}
131.69 E	13.11 S	1	8 km	60 dB
131.71 E	13.11 S	1	4 km	45 dB
131.73 E	13.11 S	0	–	–
131.75 E	13.11 S	0	–	–
:	:	:	:	:

4.2.2 Large scale data set

Observational estimates of key environmental parameters are available in a large scale data set of the Darwin region (Davies et al., 2013). This is produced using a hybrid approach developed

by Xie Shaocheng et al. (2004): a NWP variational budget analysis is used as a replacement for radiosonde observations (Zhang and Lin, 1997). The analysis data are combined with surface and TOA observations. Through a comparison with the Tropical Warm Pool International Cloud Experiment (May et al., 2008), this technique was proven to be better performing than the direct use of analyses from NWP centres (e.g. ECMWF).

Large scale quantities obtained from the radiosonde-model reanalysis have outputs at fixed pressure levels. The first measurement point is at pressure 1015hPa. This measurement is here replaced with a value at surface pressure, obtained with linear extrapolation. The result is a data set where large scale quantities, such as temperature, are defined every six hours at surface pressure and at other 40 fixed pressure levels, the lowest of which is 990hPa.

CHAPTER 5

METHODS

This chapter presents a detailed description of the steps followed to produce the results of the work. The main focus is given to a so called "bulk approach". This can be ideally visualised as one, big, convective cloud for each instance of time. As mentioned in Chapter 2.1.1, this approach lumps together all convective pixels in the domain and tries to represent the overall bulk effect of convection. A second section titled "spectral approach" aims at separating the effect of convection into three major cloud modes (i.e. congestus, deep and overshooting). With this method three big clouds can be imagined at each instance of time.

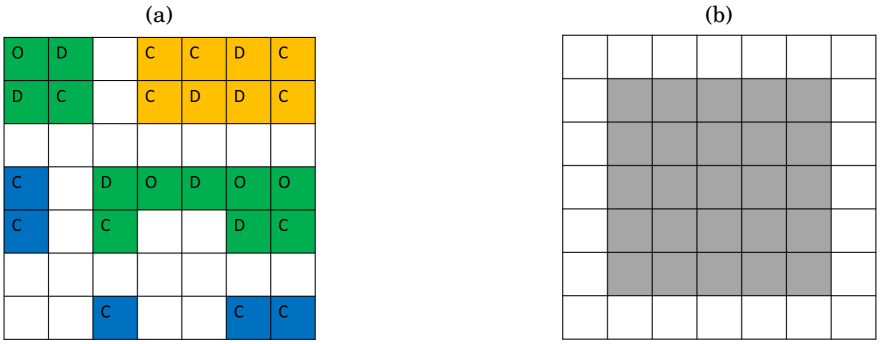

FIGURE 5.1. On the left, a simplified representation of the domain at one instance of time. Every pixel is labelled as congestus (C), deep (D) or overshooting (O) according to its ETH. The greatest ETH of a cloud defines its mode: blue for congestus, yellow for deep and green for overshooting. On the right, all pixels are lumped together in a bulk approach.

Figure 5.1 depicts a simplified situation for one instance of time where convective pixels are

labelled using their ETH as congestus (C), deep (D) or overshooting (O). The colours highlight individual clouds according to their mode (defined by the greatest ETH within the cloud): blue for congestus, yellow for deep and green for overshooting. A bulk approach (Figure 5.1(b)) groups together the effect of all convective pixels in the domain, whereas a spectral approach (not shown) groups together the effect of all clouds belonging to one mode.

5.1 Mass flux estimation

As mentioned in Chapter 2.1.1, the mass flux is defined as the product of three components: density, area fraction and vertical velocity.

Density

In this work a constant density profile is used. Firstly, a profile for each measurement time (every six hours) is calculated using the large scale temperature and the gas law equation as follow:

$$\rho = \frac{P}{R_{\mathrm{d}} T}, \tag{5.1}$$

where the pressure P is expressed in Pa, R_{d} is the specific gas constant for dry air with units J/(kg K) and the temperature T is in K. Density at the surface is obtained using independent measurements of the surface pressure (available every six hours) and values of surface temperature linearly extrapolated, from the radiosonde reanalysis data set, to the levels of surface pressure.

Secondly, using a simple first order discretization of the hydrostatic equation, the pressure levels are converted into height above the surface:

$$\begin{cases} z_{i+1} = z_i - \frac{P_{i+1} - P_i}{\rho_{i+\frac{1}{2}} g}, \\ z_0 = 0, \\ P_0 = P_{\mathrm{srf}}. \end{cases} \tag{5.2}$$

In Equation 5.2 the subscript i refers to the pressure levels, z_i is the height above the surface at a given pressure level and the surface pressure (P_{srf}) is given at all times.

The density profiles are then interpolated to fixed height levels: from 2.5 km to 13.5 km with spacing of 0.5 km. Lastly a temporal mean is performed to obtain a climatological density profile at the fixed heights above ground.

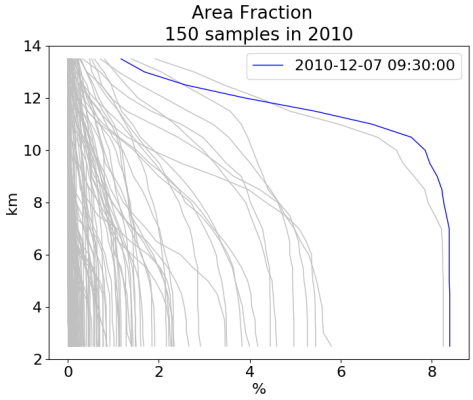

FIGURE 5.2. Samples of bulk area fraction profiles. Profiles from 150 sample instances of time in 2010 are presented in grey, the blue line refers to 07-10-2010 09:30, the red dashed line is the mean profile.

Area fraction

The area fraction (A) is retrieved from the radar measurements using the Steiner echo classification (Steiner et al., 1995) at 2.5km and the 0-dBZ echo top height (ETH). It is defined as the number of convective pixels (N_c) over the total number of pixels covered by the radar ($N = \sum p_i$):

$$A(z) = \frac{N_c(z)}{N} = \frac{\sum p_{c,i}(z)}{\sum p_i}, \tag{5.3}$$

where p_i refers to one pixel of the domain and $p_{c,i}$ to one convective pixel of the domain and the relation $p_c \subset p$ holds. The dependency of N_c and A from the height z, shown in Equation 5.3, is inferred through the ETH measurements. At each measurement level the number of convective pixels is given by the sum of convective pixels with ETH greater or equal to the current level. This method implies that N_c can only decrease with height. Although the 0-dBZ echo top height does not correspond to the actual cloud top and the Steiner method classifies a pixel as cloudy-convective only if precipitation is occurring, in this work the area fraction is not corrected to take into account cloudy-convective pixels (or levels) where precipitation is not occurring. It is also important to notice that the area fraction depends on the spatial domain considered, especially when looking at the area fraction of a single cloud.

Figure 5.2 shows some examples of bulk area fraction profiles. A mean value can be obtained at every level from the scenes that show convection (positive area fraction) at the considered level. $T(z)$ is defined as the number of times convection is measured at height z, it is important to notice that this number decreases with height because convection stops at different heights in the different instances of time. The following equation shows how the mean area fraction profile is computed.

$$\overline{A(z)} = \frac{1}{T(z)} \sum_{t=1}^{T(z)} A(z,t), \tag{5.4}$$

where $A(z,t)$ tells that area fraction is a function of height z and time t. The levels and instances of time with no convection ($A(z,t) = 0$) are not taken into account in computing the mean, as indicated by $T(z)$, function of height.

Vertical velocity

Recent works from Kumar et al. (2015, 2016) suggest a method to retrieve vertical velocity wind profiles in convective conditions; as mentioned in Chapter 2, the method uses the 0-dBZ echo top height to classify convective pixels into three cumulus modes and assign to each mode an idealised vertical wind profile. Variability to these profiles is introduced with the parameter $T_z(Z_{HWT})$, function of the height-weighted column reflectivity index. Differently from what proposed by Kumar et al. (2016), here the downdraft vertical velocity is disregarded when calculating the total vertical velocity of each pixel. The reason for this choice is that the downdraft equation in the mentioned paper shows a typo or a coefficient approximation which results in values of the downdraft vertical velocity of different signs at different height. From Equation 2.10 the following is obtained:

$$w_c(z) = w_U(z) T_z(z). \tag{5.5}$$

Where $w_c(z)$ is the vertical velocity in a convective pixel at height z. For a similar reason the updraft vertical velocity profile of a convective pixel ($w_U(z)$) is here defined with slightly different coefficients compared to the definition given by Kumar et al. (2016).

$$w_U(z) = \begin{cases} 0.404z + 0.9922, & \text{for ETH} \leq 7\text{km} \\ -0.0016z^4 + 0.0519z^3 - 0.571z^2 + 2.7z - 2.7351, & \text{for } 7 < \text{ETH} \leq 15\text{km} \\ -0.0454z^2 + 1.0889z - 0.8963 & \text{for ETH} > 15\text{km} \end{cases} \tag{5.6}$$

The correct coefficients of Equation 5.6 are retrieved from the original code and manuscript made available by the author. Figure 5.3 visually represent Equation 5.6.

Recalling what described in Chapter 2.2, the parameter $T_z(Z_{HWT})$ introduces variability to the updraft profiles described in Equation 5.6 and it is defined as

$$T_z(z) = \left(\frac{w_{res} + \overline{w_U}}{\overline{w_U}} \right) \left(\frac{w_U(z)^{0.5}}{\overline{w_U}^{0.5}} \right). \tag{5.7}$$

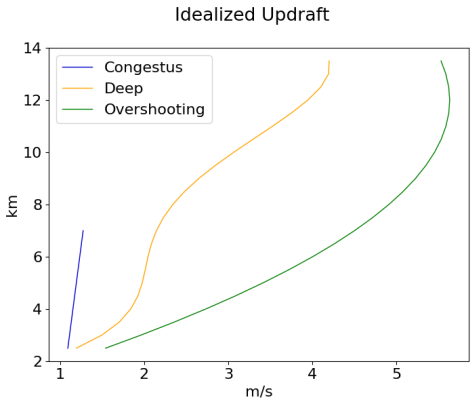

FIGURE 5.3. Updraft velocity profiles obtained from Equation 5.6

In Equation 5.7, $\overline{w_U}$ is the column-mean updraft velocity and w_{res} is called residual vertical velocity, it correspond to the amount by which $\overline{w_U}$ should be adjusted and it is modelled as a linear function of Z_{HWT}:

$$w_{res} = a + bZ_{HWT}, \tag{5.8}$$

with $a = 4.3911 - 1.2381\text{ETH}$ and $b = -0.06064 + 0.02095\text{ETH}$. The residual vertical velocity is the difference between the column-mean vertical velocity obtained from a wind profiler and the one derived using Equation 5.5 with $T_z = 1$. Kumar et al. (2016) studied the relationship of this quantity with Z_{HWT} for 246 convective profiles measured during two wet season (2005-2006 and 2006-2007) in the Darwin region and used these data to derive Equation 5.8.

Currently the use of machine learning is being tested at Monash University to estimate vertical velocity profiles inside convective clouds. Although moving away from the above mentioned simplified profiles seems to give more reliable and realistic results, the present research relies only on literature published before the start of this research.

From the vertical velocity of each convective pixel a domain mean profile is obtained at each instance of time:

$$w(z) = \frac{\sum w_{c,i}(z)}{N_c(z)}, \tag{5.9}$$

where the subscript i refers to one pixel as in Equation 5.5. The dependency of N_c from z shows that a lower amount of velocity profiles are available to calculate the mean velocity (w) high above the surface compared to the number of profiles available at low levels. Indeed, as shown above, N_c is monotonically decreasing with height. Figure 5.4 shows some examples of bulk vertical

velocity profiles.

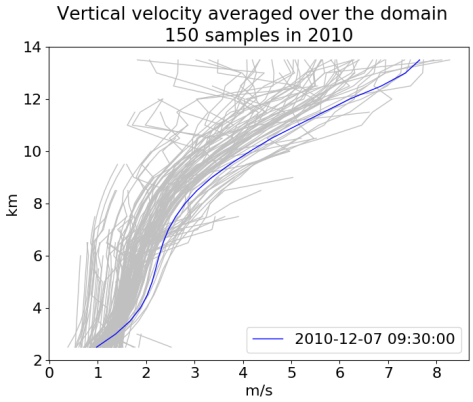

FIGURE 5.4. Samples of bulk vertical velocity profiles. Bulk vertical velocity profiles from 150 sample instances of time in 2010 are presented in grey, the blue line refers to 07-10-2010 09:30, and the red dashed line is the mean profile.

All instances of time are then put together and a mean velocity profile is computed as done for area fraction, taking care that the number of values available reduces with height.

$$\overline{w(z)} = \frac{1}{T(z)} \sum_{t=1}^{T(z)} w(z,t), \tag{5.10}$$

Mass flux

The mass-flux profiles are obtained using the definition of mass-flux given in Equation 2.2. Using the variables' name introduced above, the following equation is implemented.

$$M(z) = \rho(z) A(z) w(z). \tag{5.11}$$

Equation 5.11 defines a bulk mass-flux profile for each instance of time. An artefact linked to the choice of disregarding downdrafts (negative vertical velocities) is that mass-flux is always positive in this work. Indeed, all factors on the right hand side of Equation 5.11 are always positive. It must be noticed that the decrease of density with height also affects mass-flux profiles: constant area fraction and velocity still imply a reduction of mass-flux.

Figure 5.5 shows 150 random profiles taken from 2010. Following the same way of time averaging the profiles used for area fraction and vertical velocity, the mean bulk mass-flux, at each level, is obtained as follow:

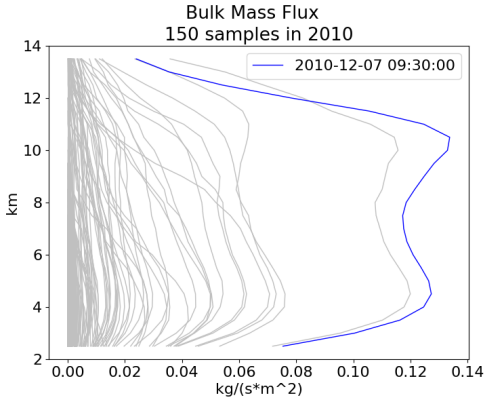

FIGURE 5.5. Samples of bulk mass-flux profiles. Bulk mass-flux profiles from 150 sample instances of time in 2010 are presented in grey, the blue line refers to a particularly strong profile and the red dashed line is the mean profile.

$$\overline{M(z)} = \frac{1}{T(z)} \sum_{t=1}^{T(z)} M(z,t), \tag{5.12}$$

The obtained mean profile helps answering the question of what is the mean mass-flux at height z given the fact that convection is occurring at that level.

5.2 Spectral approach

When considering a spectral approach, it has to be defined how the bulk effect is decomposed into the contribution of different cloud modes and how convective pixels are grouped together in order to form sub-ensembles.

5.2.1 Object identification

Neighbouring convective pixels are firstly grouped together into objects conceptually representing clouds. The grouping is done using a maximum distance from the centroid of each pixel which allows to have in the same group, diagonally neighbouring pixels. Figure 5.6 shows the outcome of the grouping algorithm on a specific instance of time.

Once the convective pixels are grouped into objects, the mass-flux of each object is obtained as follow:

$$M_j(z) = \rho(z) A_j(z) w_j(z), \tag{5.13}$$

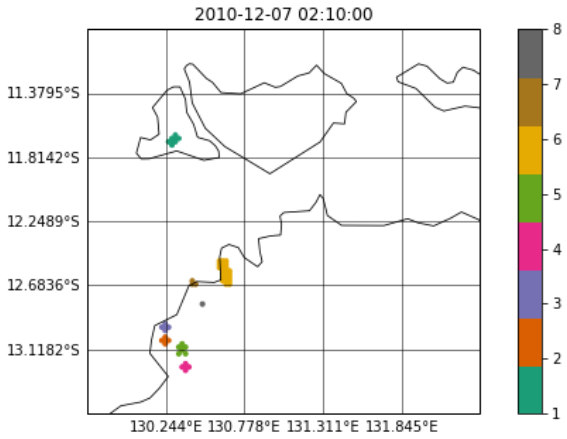

FIGURE 5.6. The same colour is given to neighbouring convective pixels to indicate the eight objects recorded in the Darwin region on 07-12-2010 at 02:10 UTC. Size of the objects is taken at 2.5 km according to the Steiner classification.

where the subscript j refers to one object and the components of Equation 5.13 are described next.

Density

To calculate the mass-flux of single objects, the same climatological density as in Equation 5.11 is used.

Area fraction

When calculating the area fraction of a single object, the domain area (total number of pixels N) remains the same as in Equation 5.3; differently, the convective area of interest (area covered by the j-th object) is a subset of the total convective area. For this reason, the area fraction of a single object is obtained as follow:

$$A_j(z) = \frac{N_{c,j}(z)}{N} = \frac{\sum p_{c,(i \in j)}(z)}{\sum p_i}. \tag{5.14}$$

In this equation, j refers to one object (defined above as a group of pixels), so $\sum p_{c,(i \in j)}$ gives the number of pixels that make up the j-th object ($N_{c,j}$).

Vertical velocity

Similarly to what done for the area fraction, the vertical velocity of a single object is defined as in the bulk approach but considering only a subset (j) of pixels.

$$w_j(z) = \frac{\sum w_{c,(i\in j)}(z)}{N_{c,j}(z)}. \tag{5.15}$$

It is important to notice that, differently from the area fraction, the sum of the vertical velocities of all objects in an instance of time does not give the bulk vertical velocity obtained with Equation 5.5. The relationship between Equation 5.5 and Equation 5.15 is given by a weighted mean:

$$w(z) = \sum_j w_j(z) \frac{A_j(z)}{A(z)}. \tag{5.16}$$

Mass flux

The equation for mass flux of a single object is already presented in Equation 5.13. It has to be noticed that the collective effect of all objects in an instance of time is equivalent to the bulk effect. Indeed the following equation holds.

$$M(z) = \sum_j M_j(z). \tag{5.17}$$

5.2.2 Cloud mode subdivision

After identifying objects based on neighbouring pixels, these are grouped to form sub-ensembles. At each instance of time, the 0-dBZ ETH is used to identify three convective modes: congestus (ETH < 7 km), deep (7 ≤ ETH ≤ 15 km), overshooting (ETH > 15 km). The thresholds are consistent with the one used by Kumar et al. (2015).

For each object only the highest ETH among its pixels is taken as representative. As a result, an object is classified as congestus if the highest value of ETH among its pixels is lower than 7 km. An illustration of the grouping method and subsequent cloud mode subdivision is presented in Figure 5.7.

Figure 5.7(a) is a view from the top of a simplified domain at one instance of time. Three objects are identified and a cross section passing from two of these is shown in Figure 5.7(b). For illustrative purposes it is assumed that the yellow pixel not involved in the cross section has ETH lower than any other yellow pixel. The yellow object is then classified as deep cloud. The blue object is classified as congestus.

Object size could also be used to provide a spectrum of clouds. Although less common, the expected result is similar as suggested when plotting the radius of an object against its ETH (see Figure 5.8).

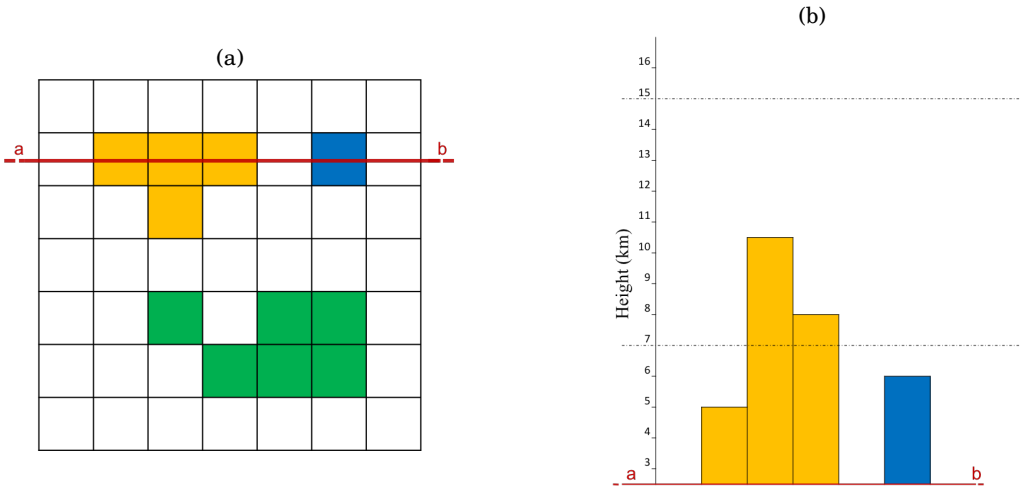

FIGURE 5.7. Representation of how convective pixels are grouped into objects. The example shows three objects: yellow object, blue object (single pixel object), green object (one pixel is only diagonally neighbouring with another convective pixel). On the right panel 5.7(b) a cross section taken as suggested by the red line. The dashed lines mark the 7 and 15 km levels used to classify objects.

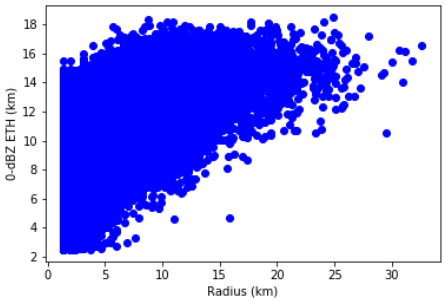

FIGURE 5.8. Relationship between radius and ETH of all objects in the period 07-12-2010 to 31-12-2011. The radii are obtained assuming circles with the same are as the objects.

For each cloud mode group ($mode = \{\text{cong}, \text{deep}, \text{over}\}$) it is possible to define the mass flux and its components at every instance of time.

$$\begin{cases} M_{mode}(z) = \sum_j M_{j|mode}(z), \\ A_{mode}(z) = \sum_j A_{j|mode}(z), \\ w_{mode}(z) = \frac{M_{mode}(z)}{\rho(z) A_{mode}(z)}. \end{cases} \tag{5.18}$$

Where the subscript in $M_{j|mode}$ tells that the j-th object has to be classified as the selected mode. It is also possible to define the relationships between sub-ensembles (spectral approach) and bulk approach:

$$\begin{cases} M(z) = \sum_{mode} M_{mode}(z), \\ A(z) = \sum_{mode} A_{mode}(z), \\ w(z) = \sum_{mode} w_{mode}(z) \frac{A_{mode}(z)}{A(z)}. \end{cases} \tag{5.19}$$

It is clear that in the spectral approach three mass-flux profiles are obtained for each scene (instance of time): one for each cloud mode.

5.3 Large scale quantities estimation

To answer the research questions, introduced in the objectives (Chapter 3) of this thesis, five large scale quantities (or parameters) are taken into consideration to describe the environmental condition; these are: relative humidity (RH), convective available potential energy (CAPE), convective inhibition (CIN), large scale vertical motion (Ω) and critical fraction of environmental air (χ_{crit}). These key parameters have frequently been associated with the behaviour of convective ensembles (Kumar et al., 2016; de Rooy et al., 2012) and are here used, one at the time, to analyse mass flux profiles. Apart from CAPE and CIN, the other parameters change with height; for simplicity and consistency with previous works (Kumar et al., 2016), their value at 500 hPa is taken during the analysis unless otherwise specified. χ_{crit} is a less common parameter and it's definition is not as trivial as for the other parameters. Its column mean value is used in this work.

5.3.1 Relative humidity

The relative humidity (RH) is obtained from the large scale data set using the measurements of water vapour mixing ratio (r) and temperature (T). First, the temperature profiles are used to calculate the saturation vapour pressure (e_{s}) with the following equation.

$$e_{\text{s}}(z) = e_0 \exp\left(-\frac{L}{R_{\text{v}}} \left(\frac{1}{T(z)} - \frac{1}{273.15} \right) \right), \tag{5.20}$$

where $e_0 = 6.1094$ hPa is the saturation vapour pressure at $T = 0$ °C, $L = 2.5 * 10^6$ J/kg is the latent heat of vaporisation, $R_{\text{v}} = 461.39$ J/(kg K) is the specific gas constant for water vapour and T is expressed in Kelvin. Next, the saturated water vapour mixing ratio (r_{s}) is obtained:

$$r_{\text{s}}(z) = \frac{R_{\text{d}}}{R_{\text{v}}} \frac{e_{\text{s}}(z)}{P(z) - e_{\text{s}}(z)}, \tag{5.21}$$

where $R_d = 287.058$ J/(kg K) is the specific gas constant for dry air. The relative humidity is then defined as the ratio of r and r_s:

$$\mathrm{RH}(z) = \frac{r(z)}{r_s(z)} 100. \tag{5.22}$$

5.3.2 Convective available potential energy

CAPE (J/kg) is defined as the positive area between the vertical profile of environmental temperature and the adiabat of a parcel; the greater this area, the greater the potential energy available for convection (see Figure 5.9). The large scale data set includes measurements of CAPE but a check is performed and all instances of time with a negative CAPE are excluded from the analysis.

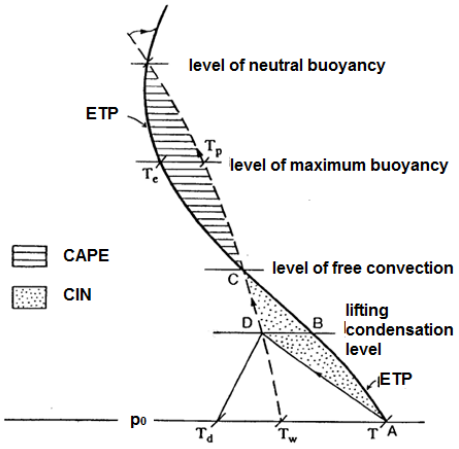

FIGURE 5.9. Illustration and CAPE and CIN. The two quantities are defined as the positive and negative area between the environmental temperature profile (ETP) and the adiabat of a lifted parcel.

5.3.3 Convective inhibition

Opposite to CAPE, CIN (also expressed in J/kg) indicates the amount of energy needed to overcome the negative buoyancy exerted from the environment on an air parcel. CIN is the negative area between the vertical profile of environmental temperature and the adiabat of a parcel (see Figure 5.9). For this reason, the more negative is CIN, the more difficult it is for a parcel to reach the level of free convection. All instances of time with a positive CIN in the large scale data set are excluded a priori.

5.3.4 Large scale vertical motion

The large scale vertical motion (or Ω) is expressed in hPa/hour and it is also a parameter available every six hour at different vertical levels in the large scale data set. Negative values of Ω refers to upward motion, while positive values are registered when large scale subsidence is in place.

5.3.5 Critical fraction of environmental air

The fraction of environmental air needed to make a parcel neutrally buoyant can be calculated both numerically and analytically (see Chapter 2 and Appendix A). In this work the analytical derivation presented by de Rooy et al. (2008) is followed and the approximation of χ_{crit} used is:

$$\chi_{\text{crit}}(z) = \frac{\Delta\theta_{\text{v}}}{\beta\Delta\theta_{\text{l}} + \frac{(\beta-\alpha)L}{c_{\text{p}}\pi}\Delta q_{\text{t}}}. \tag{5.23}$$

In Equation 5.23, the operator Δ refers to the difference between a quantity measured in the convection and the same quantity measured in the environment. $\Delta\theta_{\text{v}} = \theta_{\text{v,c}} - \theta_{\text{v,e}}$ is the difference between the virtual potential temperature of the adiabatic lifted parcel (subscript c) and the virtual potential temperature in the environment (subscript e). θ_{l} refers to the liquid potential temperature and q_{t} to the total specific humidity. c_{p} = 1004 J/kg K is the specific heat capacity of dry air, $\pi(h) = (\frac{p_0}{p})^{(-R_{\text{d}}/c_{\text{p}})}$ is the Exner function and α and β are parameters. A full description of Equation 5.23 can be found in Appendix A. The general approach, used to derive χ_{crit} is to obtain environmental quantities from the large scale data set and use a conceptual model of a lifted parcel, to obtain quantities inside the convection. At the surface, an air parcel is considered to have the same properties (temperature and specific humidity) of the environment and it is ideally lifted following a pseudo-adiabatic process. The dry adiabatic lapse rate (Γ_{d} = 9.7676 K/km) is followed up to the saturation level ($q_{\text{s,c}} = q_{\text{t,c}}$) and the moist adiabatic lapse rate (Γ_{m}) is followed above this level:

$$\Gamma_{\text{m}} = \Gamma_{\text{d}}\left[T_{\text{c}} - \frac{1 + \frac{Lq_{\text{s,c}}}{R_{\text{d}}T_{\text{c}}}}{1 + \frac{L^2 q_{\text{s,c}}}{c_{\text{p}}R_{\text{v}}T_{\text{c}}^2}}\right], \tag{5.24}$$

where $q_{\text{s,c}}$ is the saturation specific humidity of the convective air parcel. All excess water that condenses is considered to rain out so that above the saturation level $q_{\text{t,c}} = q_{\text{s,c}}$.

The right panels in Figure 5.10 show two examples of χ_{crit} profiles for two different instances of time. Because of its physical meaning, only the values between the level of free convection (dotted line) and the 0-dBZ ETH (upper solid line) are shown. The layer between the cloud base (lower solid line) and the level of free convection (LFC) can vary in thickness and is characterised by a negative buoyancy. This can be seen in the left panels of Figure 5.10 where $\Delta\theta_{\text{v}}$ and $\Delta\theta_{\text{l}}$ are

plotted. Below the level of free convection χ_{crit} can assume negative values and is disregarded for the purpose of this work . It is important to notice that, in both the instances of time in Figure 5.10, cloud base and LFC are below 2.5 km. This tells that the radar measurements often miss important information below 2.5 km and it is wrong to assume this level as the cloud base.

Equation 5.23 is an approximated form and can also return values of χ_{crit} greater than one. Although physically meaningless, this mathematical artefact is here corrected forcing χ_{crit} to have the unity value as upper boundary.

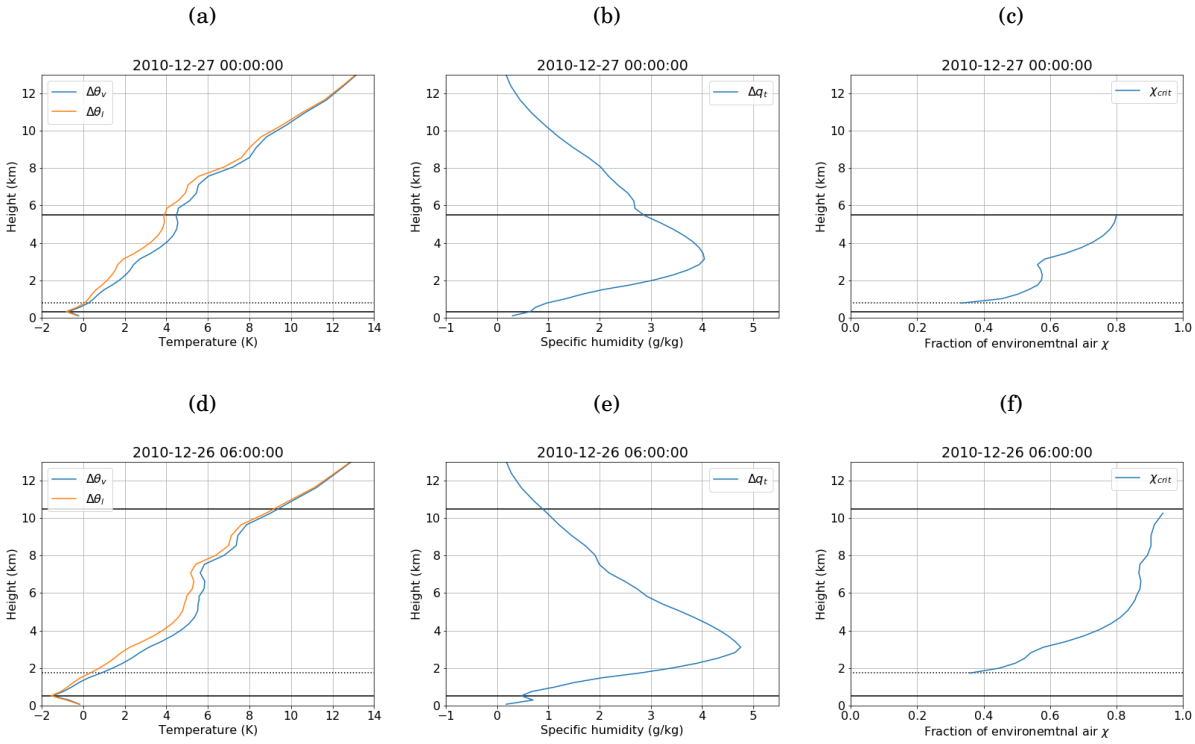

FIGURE 5.10. $\Delta\theta$,Δq and χ_{crit} for two example dates (27-12-2010 00:00 in the upper row, 26-12-2010 06:00 in the lower row). The solid horizontal lines represent the liquid condensation level (LCL) and the maximum 0-dBZ ETH, the dotted line is the level of free convection (LFC). The upper panels show an instance of time where the highest ETH measured is at around 6.5 km. In the lower panels some pixels remain convective up to around 10.5 km.

Differently from the other large scale quantities used in this work, χ_{crit} has not been previously used to analyse the Darwin data set. For this reason, there is less constrain in choosing a measurement level that well represent this parameter. The 500 hPa level (about 5.7 km from the ground) can be misleading when considering instances of time with maximum ETH below 7 km. Furthermore, χ_{crit} is a parameter that takes into account in-cloud conditions, information

regarding the vertical location of the cloud should not be disregarded. In light of this, the column mean $\overline{\chi_{\text{crit}}}$ is used during the analysis of the data set. This is the mean value of χ_{crit} between the LFC and the ETH.

5.4 Procedure

In this work mass flux is studied using the large scale quantities presented above. Firstly, values of large scale quantities at 500 hPa are obtained through linear interpolation between the available measurements at 515 and 490 hPa. In the next step, large scale quantities are temporally interpolated to 10 minutes resolution. If a large scale measurement is missing, no interpolation is performed between the last and the next available measurement. The resulting empty time window is disregarded from both the large scale data set and the CPOL data set. In order to have two data sets with the same instances of time, only dates where convection occurred at 2.5 are included in the analysis. This means that the distribution of large scale parameters used in this work (see Figure 5.11) is not representative of the entire wet season but only of the days in the wet season when precipitation is occurring.

Instances of time and the relative mass flux profiles are subsequently binned using the quartiles of large scale parameters. For each parameter three groups are obtained: one for dates with value of the parameter lower than the first quartile, another for dates with value of the parameter between the first and the third quartile and a final group for instances of time showing values of the parameter higher than the third quartile. It is important to notice that with this subdivision the second bin has double the amount of data compared to the first and the third. The choice mirrors the need to isolate instances of time with particularly low (or high) values of a parameter from most of other dates. Furthermore, it has to be mentioned that, although some of the parameters are correlated to each other, an instance of time might belong to different bins when sorted using different parameters.

5.4.1 Large scale quantities correlation

From the large scale data set alone, it is possible to see relationships between the five parameters selected for this study. Figure 5.12 shows these relationships using the Pearson correlation coefficient. Each dot refers to an instance of time and its location is given by the parameters' value at that time.

From Figure 5.12 it is already possible to notice that RH_{500} and CIN are positively well correlated: the Pearson coefficient is 0.6 as shown in Figure 5.12(c). It is expected that, the higher the correlation, the more similar is the dependency of mass-flux on the two parameters. Ideally, two perfectly correlated parameters (Pearson coefficient: 1), split the data set in exactly the same way.

(a) RH_{500} (%)

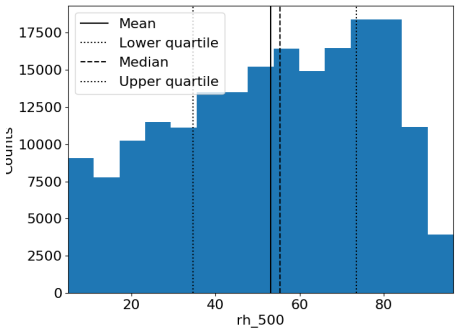

(b) CAPE (J/kg)

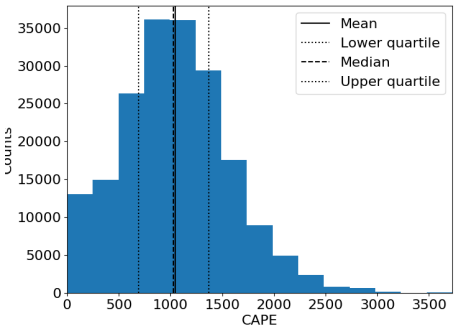

(c) CIN (J/kg)

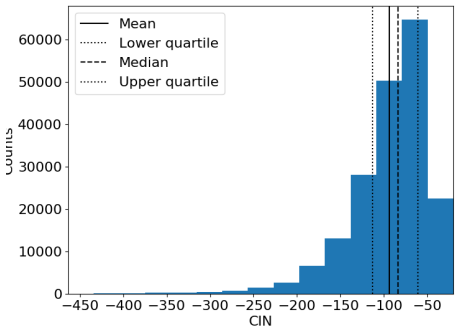

(d) Ω_{500} (hPa/hour)

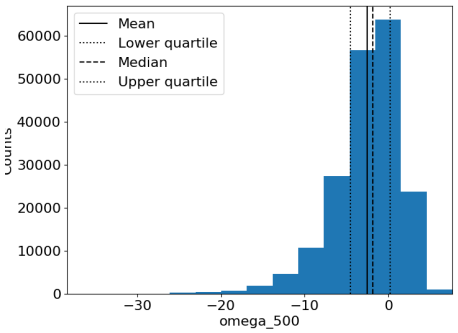

(e) $\overline{\chi_{\text{crit}}}$ (-)

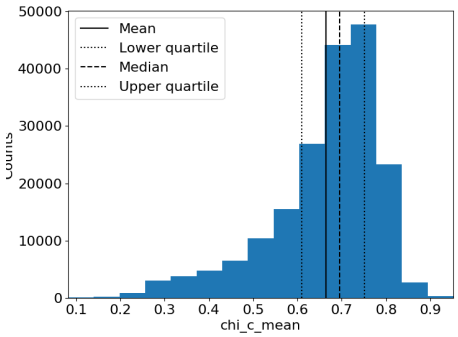

FIGURE 5.11. Probability distribution of selected environmental parameters for the dates with precipitating convection.

RH_{500} shows a reasonable correlation also with $\overline{\chi_{\text{crit}}}$ (Figure 5.12(j)) as expected considering the dependency of χ_{crit} on Δq_{t}. Less strong is the correlation between $\overline{\chi_{\text{crit}}}$ and CAPE although they are both linked to $\Delta\theta_{\text{v}}$.

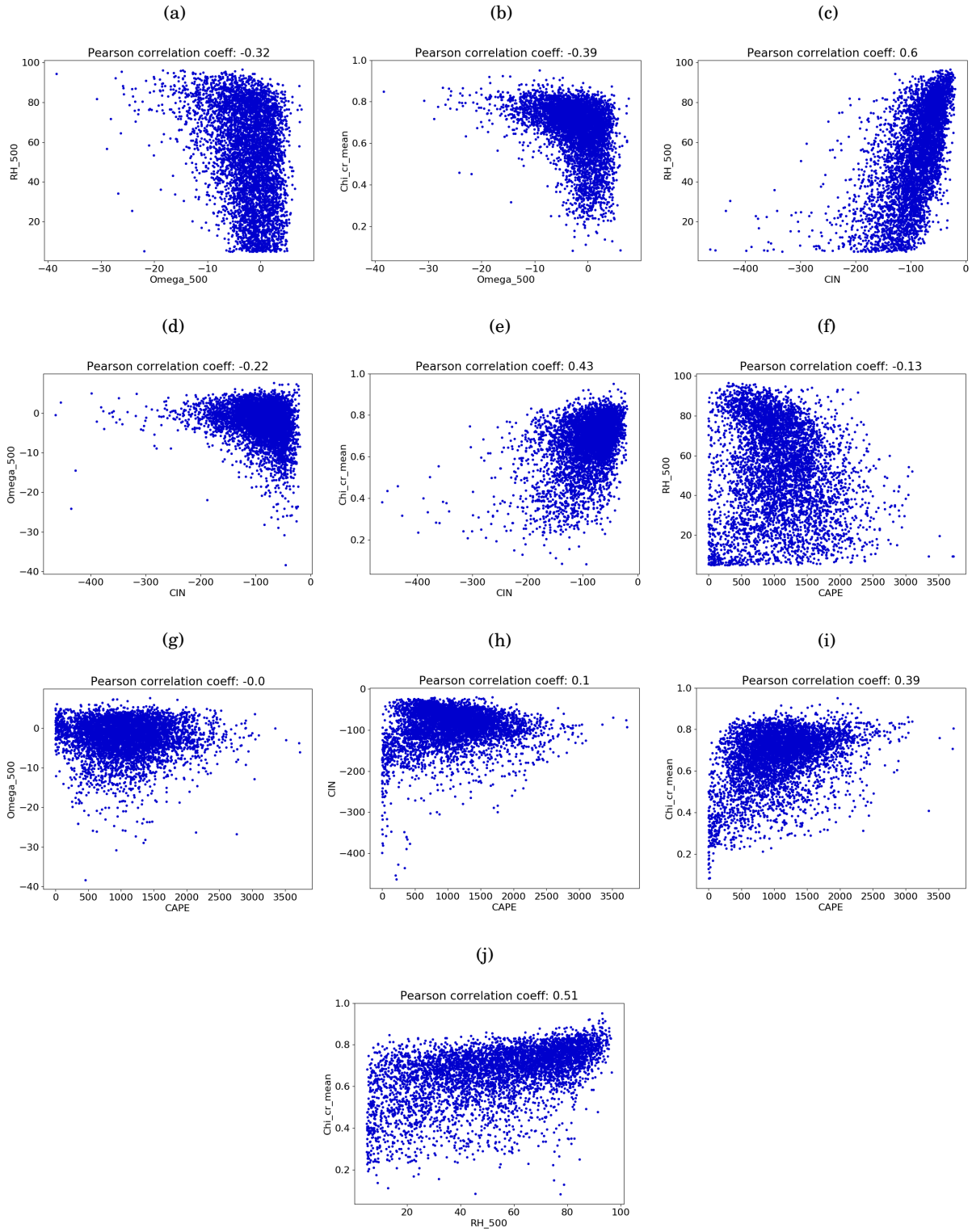

FIGURE 5.12. Scatter plots showing the correlation among large scale parameters.

5.4.2 K-means clustering

After dividing the data set using the distribution of large scale quantities, a different approach is also used to gain more insight. Here, the data set is not divided into equally sized bins but an unsupervised machine learning algorithm (K-means clustering) is used to identify groups with similar mass-flux profiles. The distribution of large scale quantities is then studied for each group.

The K-means clustering algorithm (Hartigan and A., 1975; Hartigan and Wong, 1979) aims at dividing M points in N dimensions into K clusters so that the within-cluster sum of squares is minimised. The algorithm requires as input a matrix of M point and a number K of cluster centres. The algorithm returns the mean of each cluster and labels all points with their cluster name. Although this algorithm can fall into local minima, it is very fast and can be easily applied to the large data set used in this thesis.

For this work, four cluster centroids are identified setting the maximum number of iterations to 10,000 and the relative tolerance with regards to declare convergence to 10^{-7}. The matrix M is made by the bulk mass-flux profiles so it has the number of instances of time as the first dimension and the number of vertical levels (z) as second dimension. The outputs of the algorithm are four, differently sized, groups of mass-fluxes, where each profile is closer to the mean of its group than to the mean of any other group. Figure 5.13 shows the mean mass-flux profile for each of the group (or cluster) identified by the K-means algorithm.

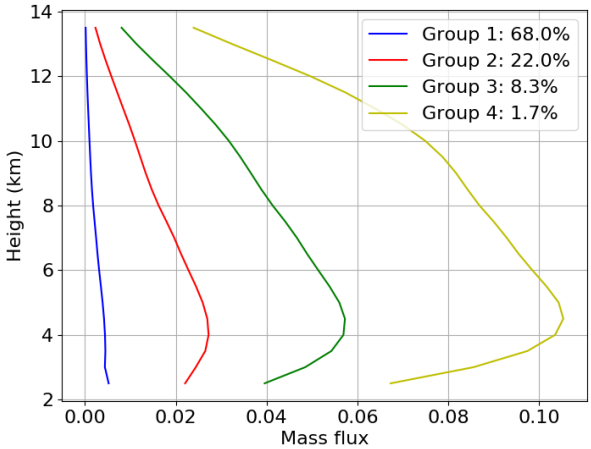

FIGURE 5.13. Mean mass-flux profiles resulting from the K-means clustering algorithm. The amount of bulk profiles belonging to each group (cluster) is specified by the percentage in the legend. Not all profile have the same height, causing the group means to be attained from less data at higher levels.

It has to be mentioned that not all profiles of a group reach 13.5 km, although the means do. The ensembles are obtained from a decreasing number of mass-fluxes with height. Of all the profiles included in Group 1, XX % reaches 10 km, while of all the profiles in Group 4, YY % is still active at 10 km.

It is interesting to notice how the four centroids primarily differ in magnitude of the mass-flux and less on the shape. Roughly 68% of the bulk mass-flux profiles in the entire data set is more similar to the blue line than to any other line in Figure 5.13. This means that most of the times convection produces little mass-flux transport. According to the K-means clustering algorithm, only 1.7% of the bulk mass-flux profiles can be associated with the yellow line in Figure 5.13. Although the amount of data in each cluster is very different, the size of the data set (13 wet seasons with 10 minutes resolution) allows to confidently perform statistics within each group of profiles.

5.4.3 Mass-flux shape

To better understand the role of environmental conditions on mass-flux, the vertical shape is decoupled from the magnitude of the latter.

Nondimensionalized mass-flux

The first way to do so is to normalise all bulk mass-flux profiles by their value at 2.5 km. The resulting nondimensionalized profiles are then grouped, as done above, according to the large scale parameters' distribution and using the K-means clustering algorithm. It is important to notice that performing the K-means clustering on the nondimensionalized profiles necessarily splits the data set in different groups compared to the one shown in Figure 5.13. Regardless of the absolute magnitude, here, the algorithm clusters together profiles with similar relative mass-flux. Figure 5.14 shows the mean profiles of the four clusters obtained using the algorithm on the nondimensionalized mass-flux.

From Figure 5.14 it can be seen that almost 26% of the profiles (Group 1) halves their magnitude within the lower 5 km, while in about 11% of the circumstances (Group 4), the mass-flux increases of a factor 1.6 in the same layer. It is also interesting to notice that, on average, profiles of Group 4 have a bimodal shape so that the mass-flux peaks at around 5 and 10 km.

Group 1 (blue line) show a characteristic monotonically decreasing shape, where the strongest value of mass-flux occurs at 2.5 km. This behaviour is typical of shallow cumulus clouds (de Rooy et al., 2008) and together with the fact that the blue line goes to zero at about 8 km, leads to the consideration that instances of time with dominance of congestus convection and perhaps weak mass-fluxes comprise the first group. Of all the profiles in Group 1, XX % goes higher than 10 km,

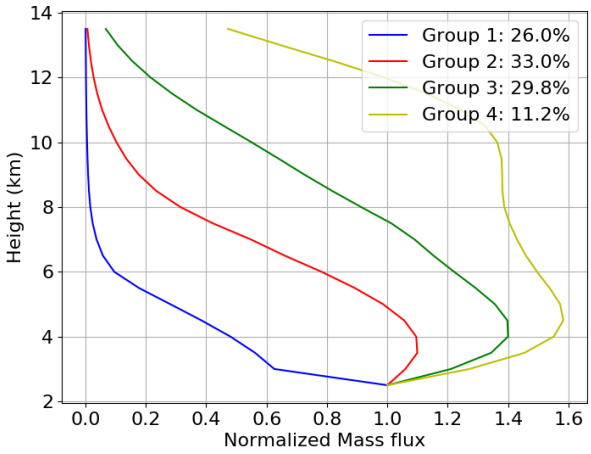

FIGURE 5.14. Mean nondimensionalized mass-flux profiles resulting from the K-means algorithm. The amount of bulk profiles belonging to each group (cluster) is specified by the percentage in the legend.

while YY % of the profiles in Group 4 reaches that level.

The second and the third group (red and green) mainly differ for the relative increase of their mass-flux from 2.5 to 4 km. It has already been mentioned that Group 4 (yellow) shows a bimodal shape; other interesting behaviours are that after 4 km the mass-flux decreases less rapidly than in other groups and the relative increase below 4 km is the strongest for this group.

Mass-flux derivative

Another way of looking at the shape of a profile is through its derivative. In line with what stated in Chapter 2.1.2, the expression $\frac{1}{M}\frac{\partial M}{\partial z}$ is used because of its relation with fractional entrainment processes.

Firstly, the quantity $\frac{1}{M}\frac{\partial M}{\partial z}$ is calculated at every instance of time, subsequently the large scale parameters are used to group the obtained profiles as done for mass-flux and for the nondimensionalized mass-flux. A second order accuracy method is used to discretize the derivative. It is a finite differences function based on central differences in the interior points and sided finite difference at the boundaries. Consistently with what done for area fraction, vertical velocity and mass-flux, the mean value of $\frac{1}{M}\frac{\partial M}{\partial z}$ and of its components is calculated at every height separately, using only the times that show convection at the selected height: $T(z)$.

$$\overline{\left[\frac{1}{M}\frac{\partial M}{\partial z}\right]}(z) = \frac{1}{T(z)}\sum_{t=1}^{T(z)}\left[\frac{1}{M}\frac{\partial M}{\partial z}\right](z,t). \tag{5.25}$$

5.5 Entraining plume equation

Using Equation 5.11 it is possible to write the change of mass-flux with height as the sum of two components. The first component only dependent on area fraction and the second dependent on the product of density and vertical velocity.

$$\frac{1}{M}\frac{\partial M}{\partial z} = \frac{1}{A}\frac{\partial A}{\partial z} + \frac{1}{\rho w}\frac{\partial(\rho w)}{\partial z}. \tag{5.26}$$

In a very straightforward manner, the two components on the right hand side of Equation 5.26 are here called area component of entrainment and velocity component of entrainment. As mentioned in Chapter 2.1.2 it is difficult to measure fractional entrainment and detrainment separately. Nevertheless, it is possible to find an equation to link these with the two components in Equation 5.26.

Knowing that

$$\frac{1}{M}\frac{\partial M}{\partial z} = \epsilon - \delta, \tag{5.27}$$

it is clear that detrainment acts to reduce the value of $\frac{\partial M}{\partial z}$, while entrainment is a positive factor. Linked to the assumption that the area fraction can only monotonically decrease with height is the fact that, in the present thesis, the area component of entrainment is always negative or equal to zero. This makes the area component always a detraining factor. Differently, the sign of the second term on the right hand side of Equation 5.26 can change and depends on the shape of the vertical velocity profile. This makes the velocity component contributing to both entrainment and detrainment processes. As a result, the bulk fractional entrainment and detrainment rates can be written as

$$\begin{cases} \epsilon = H_{\left(\frac{\partial(\rho w)}{\partial z}\right)} \frac{1}{\rho w}\frac{\partial(\rho w)}{\partial z}, \\ \delta = -H_{\left(-\frac{\partial(\rho w)}{\partial z}\right)} \frac{1}{\rho w}\frac{\partial(\rho w)}{\partial z} - \frac{1}{A}\frac{\partial A}{\partial z}, \end{cases} \tag{5.28}$$

where H is the Heaviside function.

With the data available, it is possible to calculate all components in Equation 5.26 and their probability distribution is studied to understand what plays the greatest role in determining the shape of mass-flux. Furthermore, the probability of having net entrainment is investigated at all levels.

5.5.1 Entraining plume equation for spectral approach

In Chapter 5.2 it is shown how sub-ensemble mass-fluxes are obtained for each of the cloud modes considered in the spectral approach. In every scene (instance of time), the sum of mass-fluxes

produced by congestus, deep and overshooting sub-ensembles is equal to the bulk mass-flux. Similarly, when talking about mixing processes, the sum of net fractional entrainment in the three sub-ensembles coincide with the bulk net fractional entrainment. Equation 5.29 shows this relationship.

$$\frac{1}{M}\frac{\partial M}{\partial z} = \frac{1}{M}\frac{\partial M_{\text{cong}}}{\partial z} + \frac{1}{M}\frac{\partial M_{\text{deep}}}{\partial z} + \frac{1}{M}\frac{\partial M_{\text{over}}}{\partial z}. \tag{5.29}$$

For each mode the following equation also holds.

$$\frac{1}{M}\frac{\partial M_{mode}}{\partial z} = \left[\frac{1}{A_{mode}}\frac{\partial A_{mode}}{\partial z} + \frac{1}{\rho w_{mode}}\frac{\partial \rho w_{mode}}{\partial z}\right]\frac{M_{mode}}{M}. \tag{5.30}$$

It has to be noticed that the components on the right hand side of the entraining plume equation are no longer solely dependent on area fraction or vertical velocity when considering a spectral approach. The weighting factor $\frac{M_{mode}}{M}$ is common to both the components and is dependent on both area fraction and vertical velocity. The probability distribution of the net fractional entrainment for each cloud mode is presented in the next chapter.

5.6 Assumptions and limitations

Although not true for increasingly high resolution models, the area fraction covered by convection must be much smaller than the total domain area in order to use the equation of mass flux ($M = \rho a w$) (Yano, 2014). This scale separation principle allows to approximate the grid-box means by the environmental values and is at the base of Arakawa's parameterization (Arakawa et al., 1974).

One of the core simplifications, made in the present work, regarding the physical processes inside convection is the negligence of downdraft velocities. Riehl and Malkus (1958) already pointed out the relevance of convective downdrafts as contributors to the energy transport through deep layers of the atmosphere.

A second assumption is made necessary by the type of data available: the frontier between clouds and environment is thought to be sharp and all parcels can only have cloud properties or environmental properties.

It is mentioned above that a constant climatological density profile is used to calculate mass-flux profile. The error introduced with this decision is not quantified for the present research but a small value of standard deviation justifies the approximation. Linked to temporal variability of physical processes is the assumption that the relationship between environmental properties

and cloud core mass flux stays constant throughout the 13 wet seasons. In a changing climate this might not be true since the behaviour of convective systems has already been proven to be affected by climate change (Sherwood et al., 2010; De Lavergne et al., 2014).

The choice of parameters to describe environmental condition involves numerous assumptions too. First of all, the idea that CAPE, CIN, ω_{500}, RH_{500} and $\overline{\chi_{\text{crit}}}$ well represent the environment is simplistic. The parameter χ_{crit} results from assuming that all negatively buoyant mixtures are detrained while, all positively buoyant mixtures are entrained (de Rooy et al., 2008). Furthermore, the in-cloud quantities are calculated with a pseudo-adiabatic approximation. This implies that all liquid water obtained from condensation rains out instantly.

It should be kept in mind that the results produced in this work follow from taking into account only precipitating convective clouds as contributors to the mass-flux. This limitation comes from the instrument used to measure cloud reflectivity (CPOL radar).

Another limit of the CPOL data set is that, to cover the entire study area, the lower vertical boundary is set at 2.5 km from the surface. It is known (Johnson et al., 1999) that in the tropics cloud spatial organisation follows the trimodal distribution of divergence and cloud detrainment. Peaks in the distributions of cloud types are in close proximity to prominent stable layers: at 2 km (trade stable layer), 4.5 km (freezing level) and 15 km (tropopause). The data set available for this research does not give access to information below 2.5 km and only allows to analyse the 0°C stable layer.

Regarding the spatial resolution provided by CPOL, this becomes critical when dealing with very strong updrafts or rapidly changing profiles. Discretizing a partial derivatives in the vertical direction when consecutive measurements points are excessively far apart can introduce large errors.

As mentioned above, individual pixels in the domain are classified as convective or not convective using the Steiner algorithm. This classification is performed at 2.5 km only. This implies that a grid column can not be intermittently convective and that clouds expanding with height are not captured. Indeed, the area fraction can only decrease with height it the present work.

Another limitation derives from having large scale environmental parameters retrieved from NWP variational reanalysis. These parameters are interpolated from 6 hour resolution to 10 min resolution and only one value is available for the entire domain area.

CHAPTER 6

RESULTS

In this chapter results are shown and described. First, the distribution of bulk mass-flux, area fraction and vertical velocity for the entire data set is presented. Second, the reciprocal influence of bulk mass-flux and environmental parameters is shown using multiple methods (see Chapter 5). Appendix C shows a further variation to the methods, while the influence of parameters on vertical velocity and area fraction can also be seen in independent figures listed in Appendix B. Subsequently, the vertical gradient of bulk mass-flux, area fraction and vertical velocity is analysed in terms of entrainment and detrainment. A final section shows the relative contribution of three cloud modes to the bulk mass-flux, area fraction, vertical velocity and fractional entrainment.

6.1 Processed data

The initial phase of this work aimed at producing a data set of bulk mass-flux profiles. The result of Equation 5.11 is shown in Figure 6.1. This depicts the probability distribution of area fraction (Figure 6.1(a)), vertical velocity (Figure 6.1(b)), mass-flux (Figure 6.1(c)) and nondimensionalized mass-flux (Figure 6.1(d)). A two dimensional histogram is used; on the x-axis is the intensity of mass-flux, on the y-axis is height above the ground and the colour (z-axis) gives the height of the bars as a probability density. In all panels the sum of the probabilities across all height is one so, the fact that some profiles do not reach 13 km is seen as a reduction in the overall probability of the levels. The dotted lines show the first and third quartiles of the distribution, the dashed line the median and the solid line the mean. The higher the probability of one bar, the more profiles fall in that range of mass-flux magnitude at a given height. It is important to recall the fact that the mean is computed at every level among the profiles with positive area fraction. This allows to study the intensity of mass-flux without the bias of instances of time where convection does not

occur.

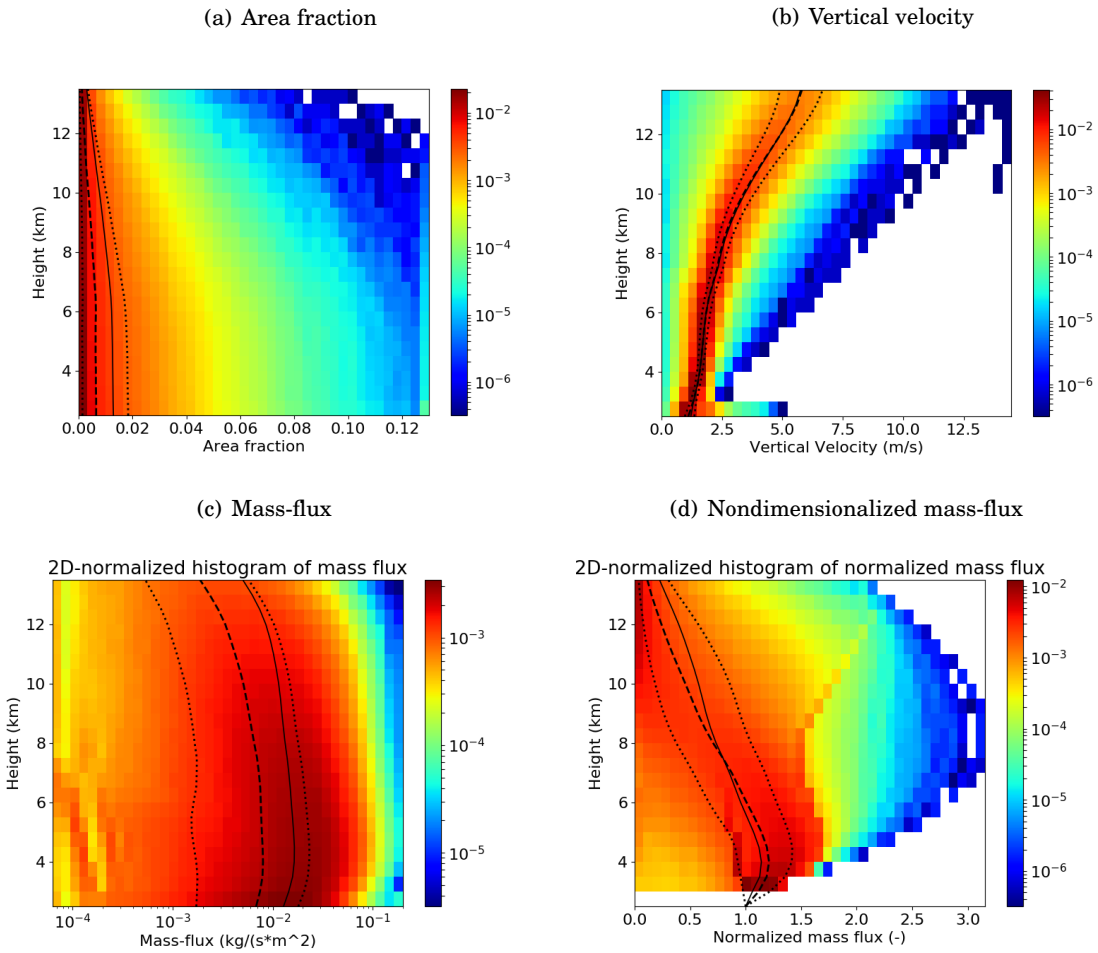

FIGURE 6.1. Probability distribution of bulk mass-flux using all instances of time. Solid line refers to the mean, dashed line to the median and the dotted lines to the first and third quartiles. The amount of data available reduces with height.

Majority of the times, mass-flux is small and, in order to appreciate its distribution, a logarithmic scale is used in Figure 6.1(c). For this reason the profiles seem to be almost straight vertical lines but, when looking at Figure 6.1(d), a clearer shape of convective mass-flux can be seen. Most of the profiles show an increasing magnitude in the lower few kilometres, with a maximum at 4 km highlighted by the mean profile, the median and the third quartile in Figure 6.1(d). Higher than 4 km the overall trend is of decreasing magnitude but the blue area shows that, in some circumstances, the mass-flux keeps increasing and, between 4.5 and 12 km, can more than double the value at 2.5 km. It is mentioned above that area fraction is simplified as monotonically decreasing in this work. For this reason any increase of mass-flux with height is the resulting effect of vertical velocity. Figure 6.1 does not show individual profiles but a small sample of these

can be seen in Figure 5.2, 5.4 and 5.5.

Before presenting how environmental conditions affect the distribution of mass-flux, it can be useful to show the distribution of two sub-groups of profiles arbitrarily obtained using the value of mass-flux at 2.5 km. Of all the bulk profiles, only 25% with the strongest (weakest) values of mass-flux at 2.5 km are taken and their distribution is presented in Figure 6.2.

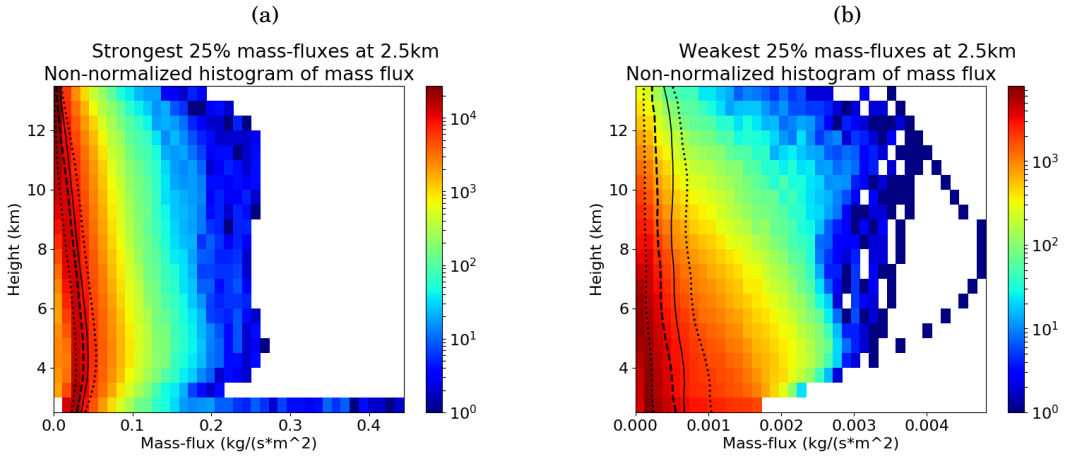

FIGURE 6.2. Probability distribution of mass-flux separate for the profiles with strongest (Figure 6.2(a)) and weakest (Figure 6.2(b)) values at 2.5 km.

The left panel (Figure 6.2(a)) refers to strong mass-fluxes, while the right panel (Figure 6.2(b)) refers to weak mass-fluxes. It can be observed that strong mass-fluxes are more prone to present a bi-modal profile with a first peak at around 4.5 km and a second peak at 11 km. As one would expect, weak bulk mass-fluxes are less likely to reach high altitudes. This fact can be seen in the decay rate of probability with elevation. Despite the magnitude of the mass-flux, the colour suggests that it is more likely to find a profile at 12 km in Figure 6.2(a) than it is in Figure 6.2(b). The statistics (mean and quartiles) tell that the few profiles reaching altitudes higher than 10 km in Figure 6.2(b) have, on average, similar intensity to the larger number of weak mass-fluxes at the base.

Another, clearer way of seeing the decrease with height of the number of times convection is observed, is by looking at the percentage of profiles reaching a certain height. Figure 6.3 shows this percentage on the x-axis. The black line refers to all instances of time, the blue line to the 25% of times with weak mass-flux at 2.5 km and the red line to the times with the strongest 25% mass-fluxes at 2.5 km. It is clear to see that, overall, less than 50% of the times convection reaches 12 km but it is also clear that this percentage is strongly dependent on the magnitude of the mass-flux at 2.5 km. More than 80% of the bulk mass-flux profiles with a strong value

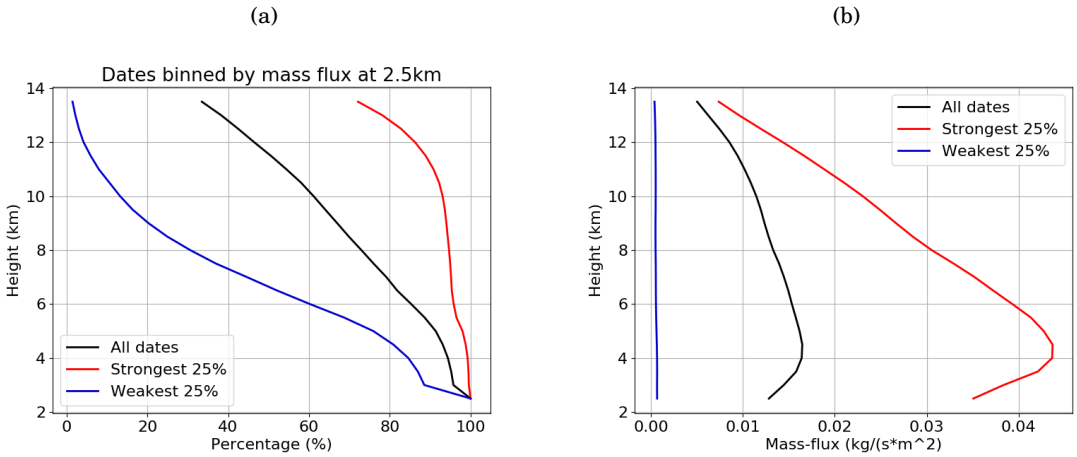

FIGURE 6.3. The black line refers to the entire data set, the red line to the sub group of 25% strongest mass-fluxes at 2.5 km and the blue line to the sub group of 25% weakest mass-fluxes at 2.5 km. In Figure 6.3(a) the percentage of bulk convective mass-flux profiles reaching a certain height. In Figure 6.3(b) the mean mass-flux profiles for each sub-group.

at the base still have some convective pixels at 12 km, the value drops to less than 10% when considering bulk profiles with weak mass-flux at 2.5 km.

Another piece of information given by Figure 6.3 is that almost all the strong profiles hit the 10 km elevation and the percentage decrease rapidly from 10 to 12 km. Differently, for the weak profiles, the percentage drops fast between 5 and 9 km but the few profiles with weak mass-flux at the base that reach 10 km, are likely to reach 12 km too.

This preliminary analysis of the data provides important information on the relevance of mass-flux at 2.5 km. The value at this height appears to be crucial for the magnitude and shape of the entire profile: bulk clouds with strong mass-flux at the base grow taller than bulk clouds with weak values of mass-flux at the base. Furthermore Figure 6.3(a) is useful to remind that the amount of data available to perform statistics at high levels is smaller than then one available at 2.5 km.

6.2 Mass-flux and environmental condition

In this section the mutual influence of environmental condition and mass-flux is presented. Although the long data set would allow for a more reliable analysis, numerous studies have already investigated this relationships. For this reason and for clarity reasons, only mean profiles are shown here. The main focus is to ensure that the methods produce solid results and to verify

what stated in the literature.

(a) RH_{500}

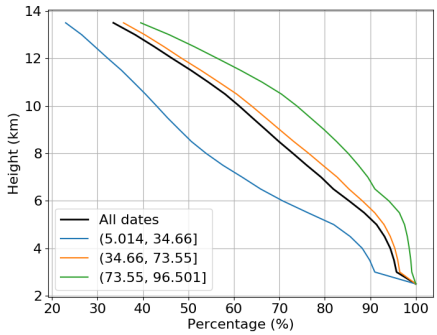

(b) CAPE

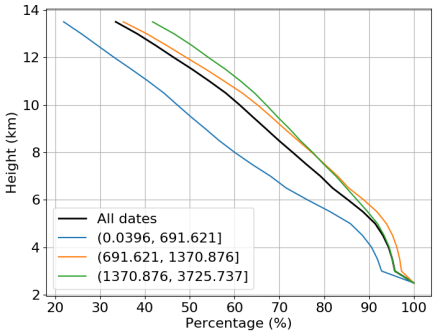

(c) CIN

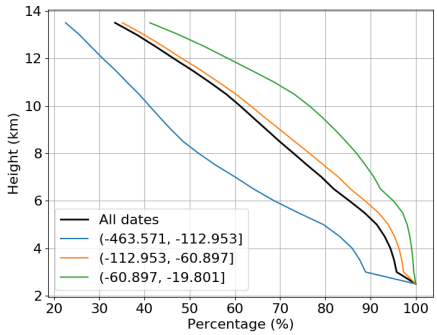

(d) Ω_{500}

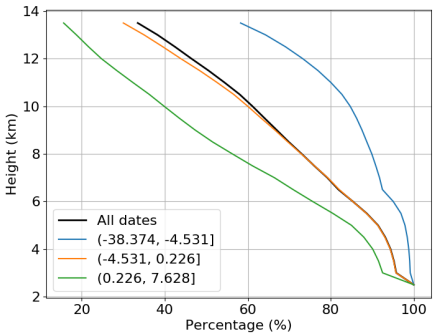

(e) $\overline{\chi_{\text{crit}}}$

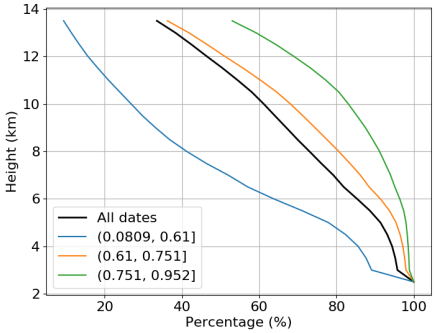

FIGURE 6.4. Percentage of bulk convective mass-fluxes reaching a certain height. Different sub group of mass-fluxes are shown. The black line refers to the entire data set (same as in Figure 6.3). The blue line refers to mass-fluxes occurring with low values of an environmental parameter, the orange and green lines are respectively for mid and high values of a parameter. Each panel refers to one environmental parameter.

It is mentioned above that a mean mass-flux is computed at every height using only instances of time with at least one convective pixel at that height. This implies the need to investigate the importance of large scale parameters in controlling the maximum height of convection (see Figure 6.4). Similarly to Figure 6.3, the lines show the percentage of time convection reaches a certain height for each sub-group of dates. The black line refers to all instances of time together, the blue line to the instances of time with values of the parameter in the lower 25% of the parameter's distribution, the orange line is for values of the parameter between the first and third quartile and the green line for instances of time with values of the parameter higher than the third quartile.

In all cases the orange line reasonably follows the black line; while, when extreme environmental conditions are taken into account, the highest ETH in the domain varies considerably depending on the parameter. CAPE seems to have the smallest effect in determining the height of bulk convection since all lines in Figure 6.4(b) are close to the mean. Differently, CIN, Ω and χ_{crit} play an important role in determining the probability for a bulk convection to reach a certain height. Taking $\overline{\chi_{\text{crit}}}$ as example; when small fractions of environmental air are enough to make the convection neutrally buoyant it is, as expected, difficult to find mass-flux profiles extending to high altitudes. This situation is described by the blue line in Figure 6.4(e): the percentage of profiles with active convective pixels drops quickly after 6 km.

Figure 6.4 is particularly important to understand the results shown in the next sections. It gives information on how many bulk mass-fluxes are used to obtain a mean. For example, the blue line in Figure 6.4(a) suggests that, when selecting instances of time with dry environment, the mean mass-flux at 10 km can be calculated with only half the number of profiles compared to the one available at 2.5 km under the same dry condition. Although this approach makes it wrong to interpret the mean profiles shown in following sections as climatological profiles of all dates with convection, it allows to characterise mass-flux inside convection at each level independently. This also means that the number of times with shallow bulk convection does not influences the mean mass-flux computed at high levels.

6.2.1 Mass-flux magnitude

Here the role of environmental condition on mass-flux magnitude is investigate. The methods and the graphs used necessarily take into account profiles shape too but the latter is better studied in a further section (Chapter 6.2.2).

Dates binned with parameters' distribution

As already mentioned in Chapter 5, mass-flux profiles are firstly grouped according to the value of some selected parameters (RH_{500}, CAPE, CIN, Ω_{500}, $\overline{\chi_{\text{crit}}}$) and the mean for each group calculated

at every level; results are shown in Figure 6.5.

(a) RH_{500}

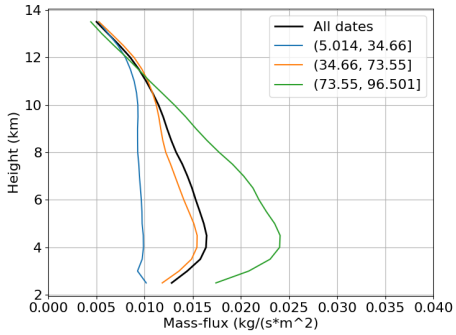

(b) CAPE

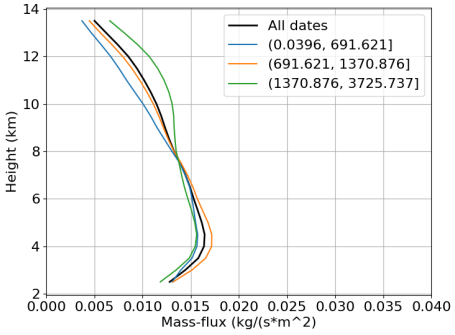

(c) CIN

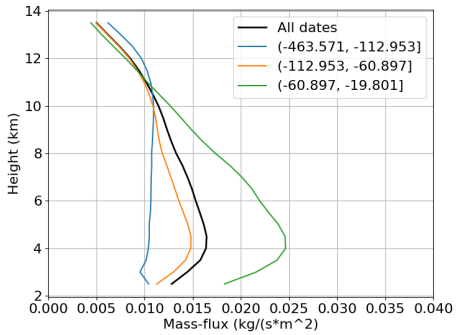

(d) Ω_{500}

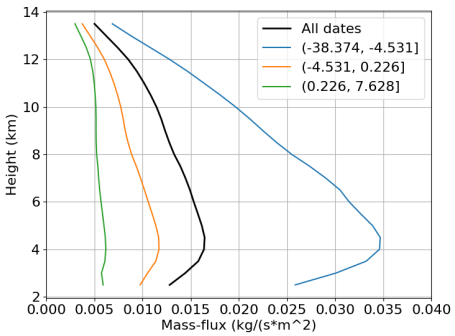

(e) $\overline{\chi_{\text{crit}}}$

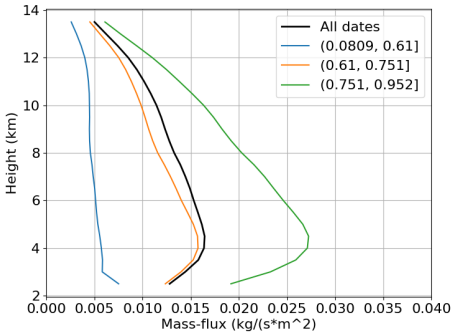

FIGURE 6.5. How environmental parameters affect mean mass-flux at each level.

The colours refer to groups of dates in the same way as explained for Figure 6.4: the orange line is the mean taken from 50% of the profiles, while the blue and the green line refers to only 25% of the total number of profiles. Furthermore, the amount of profiles available to perform the mean decreases with height following the curves shown in Figure 6.4.

The relevance of computing the mean at one level using only instances of time with active convection at this level can be better appreciate with an example. Figure 6.5(c) tells that bulk mass-fluxes at 10 km have similar strength when CIN is very large (blue line) and when CIN has values close to the median of its distribution (orange line). Despite the number of profiles reaching this height in one or the other group, this piece of information suggests that CIN does not influences mass-flux values at 10 km. If all instances of time with low CIN and no convection at 10 km were taken into account in computing the mean at this level, the resulting mean mass-flux would be considerably lower. This is suggested by the blue line in Figure 6.4(c): under very negative CIN only 40% of the bulk profiles active at 2.5 km are still active at 10km. Since this percentage is different for mid-values of CIN (ca. 60%), the orange line in Figure 6.5(c) would be shifted towards zero less than the blue line.

The five panels in Figure 6.5 are analysed one by one. It must also be mentioned that, differently form Figure 6.1(c), here the mass-flux is shown on a linear x-axis.

- RH_{500}: Up to 8 km, Figure 6.5(a) shows a sensible distinction of mass-flux magnitude linked to the humidity of the environment. Between 3 and 6 km the mean mass-flux under wet condition (green line) is more than double compared to the mass-flux observed under dry condition. This can be explained because the area fraction at low elevations is expected to be large with high RH. On the contrary, low values of RH are associated with few, very strong, convective plumes whose bulk effect is limited at low levels because of the small area fraction. Another interesting thing that can be observed from this figure, is that the bulk mass-flux seems to change little over height under dry condition, while the magnitude of mass-flux in wet condition drops fast after 4 km. This phenomenon is linked to the fact that with a humid environment precipitating clouds can form easily but do not necessarily have the buoyancy to reach high elevation. The result is a large area fraction at low levels and a smaller area fraction at higher levels (see Appendix B). Differently, under dry condition, in the rare cases where convection reaches the condensation level, it is pushed by a strong updraft that keeps the cloud tower rising to high elevations.

- CAPE: Kumar et al. (2015) and Davies et al. (2013) already showed that CAPE has little to no influence in determining the magnitude of mass-flux. This can be observed also in Figure 6.5(b) since, regardless of the interval of CAPE values, the mean bulk mass-flux never deviate evidently from the mean obtained with all instances of time.

- CIN: The high correlation between CIN and RH_{500} observed in Figure 5.12(c) can largely explain the similarities of Figure 6.5(c) with Figure 6.5(a). When the energy available to inhibit convection is large (blue line), bulk mass-flux profiles show small magnitudes at low levels. Nevertheless, the few occasions (percentage given by Figure 6.4(c)) with enough

strength to bring convection above 10 km have mass-flux greater than average at high levels. The opposite occurs when CIN is close to zero (green line); in this cases the mass-flux becomes, on average, relatively strong around 4 km and then decrease rapidly. Lastly, it is interesting to notice that the blue line shows a stronger mean mass-flux at 11 km than at 3 km. This does not indicate that mass-flux increases with height up to 11 km. More likely, the profiles used to compute the mean at 11 km are stronger at 3 km but not enough to considerably influence the mean at 3 km. As a result, if bulk mass-flux is measured at 11 km with large values of CIN, this will have, on average, a value of $0.011 \mathrm{kg\,s^{-1}\,m^{-2}}$. If bulk mass-flux is measured at 3 km under the same environmental condition, it will have, on average, a value lower than $0.01 \mathrm{kg\,s^{-1}\,m^{-2}}$

- Ω_{500}: The large scale vertical motion seems to be the most important parameter in determining the magnitude of bulk mass-flux. Subsiding motion (green line in Figure 6.5(d)) is characterised by very weak and constant profiles, on average around $5 \times 10^{-3} \mathrm{kg\,s^{-1}\,m^{-2}}$ at all heights. Strong upward vertical motion (blue line) are, on the contrary, associated with strong mass-fluxes that on average reach $35 \times 10^{-3} \mathrm{kg\,s^{-1}\,m^{-2}}$ at 4 km. Similarly to what said for Figure 6.5(a), the reason why one tail of the distribution shows profiles constant with height and the other tail shows a decreasing mean profile after 4 km is that, when environmental air is subsiding, only few but very tall towers manage to develop. This is reflected in low and constant values of area fraction (see Appendix B) which, as demonstrated in previous works (Kumar et al., 2015), is the main factor in determining the bulk mass-flux magnitude and, as it will be stated in a further chapter, is the main driver for mass-flux shape above 6 km.

- $\overline{\chi_{\mathrm{crit}}}$: The last panel in Figure 6.5 gives information on how well χ_{crit} can be used to group bulk mass-fluxes. It appears that, on average, when a rising convection can be stopped and made neutrally buoyant by mixing it for less than 60% with environmental air (blue line), the bulk mass-flux never increases from its value at 2.5 km. When the fraction of environmental air needed to make the convection neutrally buoyant is greater than 75% (green line), the bulk mass-flux is, on average, stronger and shows a more familiar shape: increasing up to 4 km and then decreasing.

Dates binned with K-means clustering

In Chapter 5 the K-means clustering algorithm is introduced as a way of grouping similar mass-flux profiles. Here the distribution of large scale parameters is analysed for each of the cluster identified with this method. Figure 6.6 shows box-plots to summarise the mentioned distributions. The colours and group names correspond to the one used in Figure 5.13, the black and grey colour are used when considering all instances of time together. The solid line refers to the mean, the dashed line to the median, the box edges coincide with the first and third quartiles and the

whiskers show the range of the data.

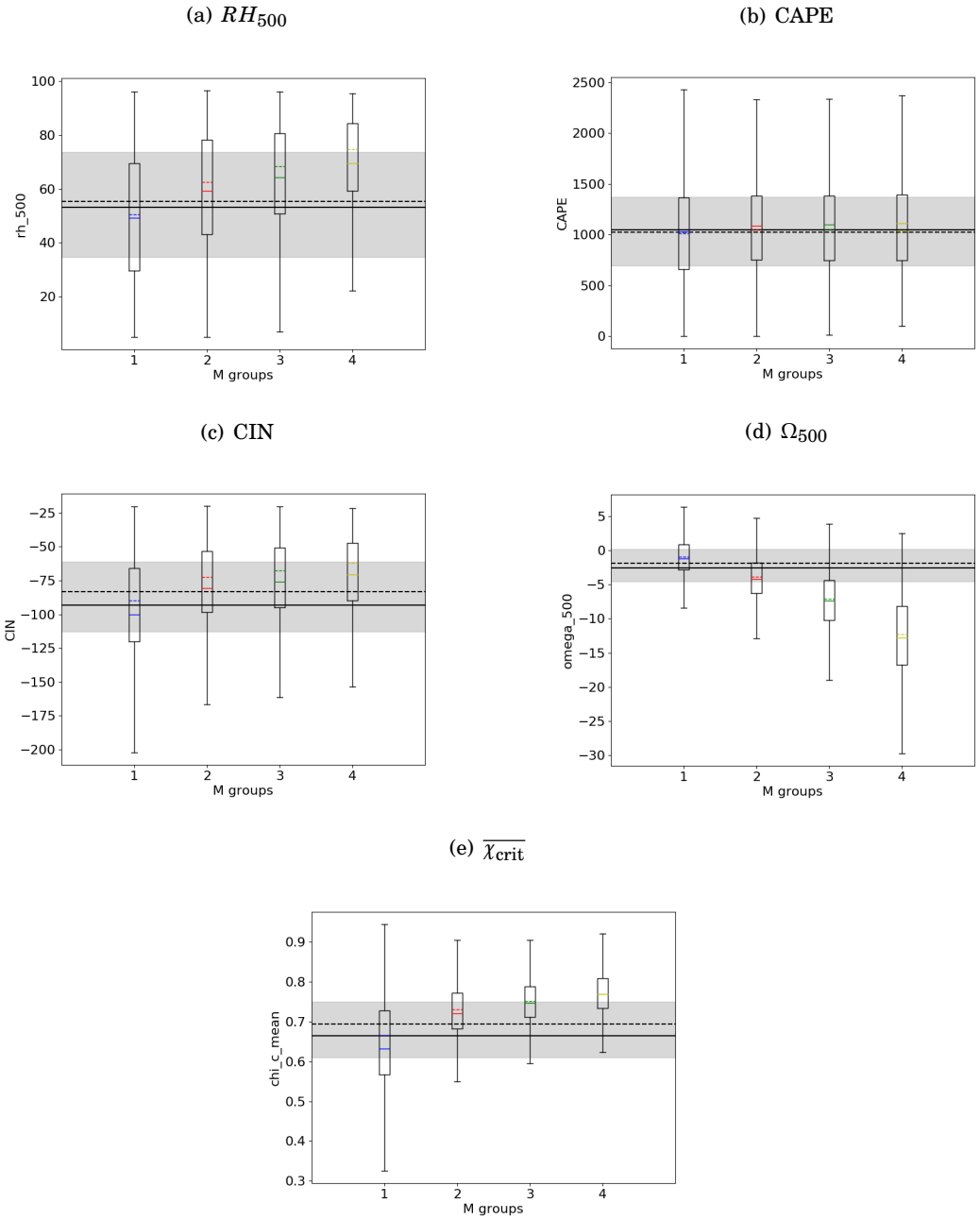

FIGURE 6.6. Parameters' distribution. Each panel shows the distribution of a parameter using all instances of time in the data set (black lines) and using groups of times identified applying the K-means clustering algorithm to the mass-flux profiles. Colours are assigned to groups as done in Figure 5.13.

Without describing all the panels individually, some general information can be taken from

Figure 6.6. Recalling Figure 5.13, the first group (blue) comprise more than 68% of the observed dates with convection; for this reason, a great spread around the mean is expected from the first box on the left of each sub-figure. Similarly, the fourth group (yellow) represent only 1.7% of all bulk profiles so, a more limited range of parameter's values is expected in this group. This is not the case for Figure 6.6(b) and Figure 6.6(d): the first shows that, regardless of the magnitude of mass-flux (different for each group), CAPE can assume any value and its distribution does not change. Differently, the distribution of Ω_{500} (Figure 6.6(d)) changes considerably from one group to the other, the mean goes from close to zero (no large scale vertical motion) for weak mass-fluxes, to -15 hPa/hour (pronounced upward vertical motion) for the fourth group. Nonetheless, all the numerous dates falling in the first group can only acquire few value of Ω_{500}. Apart from CAPE, all other parameters vary their distribution with the four clusters. As one would expect from Figure 6.5, the mass-flux magnitude is mostly affected by Ω_{500} and $\overline{\chi_{\text{crit}}}$; the latter proves again to be an important parameter in describing bulk mass-flux.

It must be recalled that some of the parameters used in this work are height dependent and the value at 500 hPa (Ω_{500} and RH_{500}) or the column mean ($\overline{\chi_{\text{crit}}}$) are arbitrarily chosen to represent the large scale environmental condition. It is interesting to look at how the parameters' distribution changes with the cluster groups at different heights. For this reason, in Figure 6.7, the mean value of Ω, RH and χ_{crit} is presented at all heights, for each of the four clusters.

It appears that the choice of using 500 hPa as representative measurement level is reasonable and effective since the profiles, especially for Ω differ the most around this height. χ_{crit} does not present very distinct values at 500 hPa for the four groups, this explains why using the column mean ($\overline{\chi_{\text{crit}}}$) turns out to be a better choice than $\chi_{\text{crit,500}}$ (not shown in this work) to present the results. Figure 6.7 is also useful to acquire a rough idea of how vertical profiles of RH, Ω and χ_{crit} are: RH has its maximum close to the surface and Ω tends to zero at the vertical boundaries. Reasonably and how explained by de Rooy et al. (2012), χ_{crit} is inversely proportional to RH.

6.2.2 Mass-flux shape

In the previous section the environmental condition and the corresponding bulk mass-flux are analysed with attention to the mass-flux magnitude. In order to distinguish the relationship of large scale parameters on profile' shape from the one on magnitude, mass-flux profiles are nondimensionalized (see Chapter 5). The results are organised as in Chapter 6.2.1.

Dates binned with parameter's distribution

Figure 6.8 shows, for each group of large scale condition, the mean nondimensionalized mass-flux with the same colour convention used above. This figure helps understanding how much stronger or weaker the bulk mass-flux is at every level compared to its value at 2.5 km.

(a) RH (b) Ω

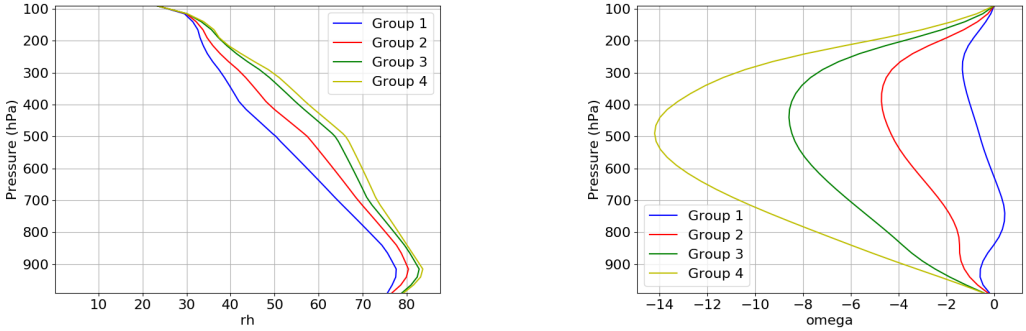

(c) χ_{crit}

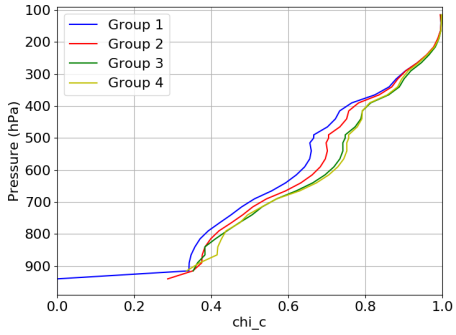

FIGURE 6.7. Mean vertical profiles of environmental parameters grouped according to Figure 5.13.

- RH_{500}: Figure 6.8(a) suggests that under dry condition the bulk mass-flux has, on average, its maximum a 2.5 km. The blue line is, indeed, lower than 1 at all heights. For other values of RH_{500}, the bulk mass-flux is, on average, greater than its value at 2.5 km up to 6 km or 7 km for wet condition. Differences can be seen mainly at the level where the mass-flux peaks (4 km). Under wet condition the value at 4 km is, on average, more than 1.2 times the value at the base. This factor is about 1 when RH is lower than 34.7%.

- CAPE: When looking at the effect of CAPE on the overall profile of mass-flux (Figure 6.6(b)) it was concluded that it has little to no influence in determining its magnitude. Here, by looking solely at the shape of mass-flux, it is possible to argue that CAPE affects, to a certain extent, the bulk-mass flux profile. Although all lines in Figure 6.9(b) have their maximum at 4 km and the values at this height range only between 1.05 (blue line) and 1.2 (green line), the height at which the mass-flux becomes lower than its value at 2.5 is greatly different for the three sub-groups: 5 km for low CAPE, 6 km for mid CAPE and almost 7 km for high CAPE. Differently from other environmental parameters, the effect of

(a) RH_{500}

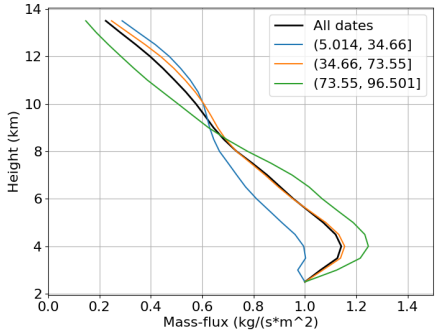

(b) CAPE

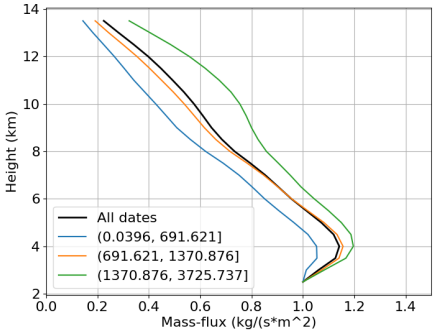

(c) CIN

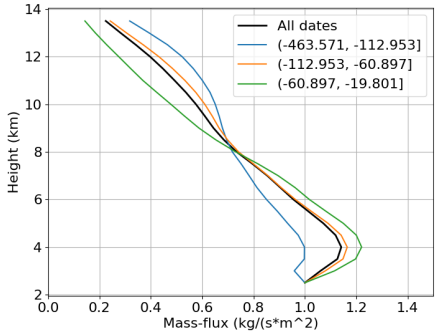

(d) Ω_{500}

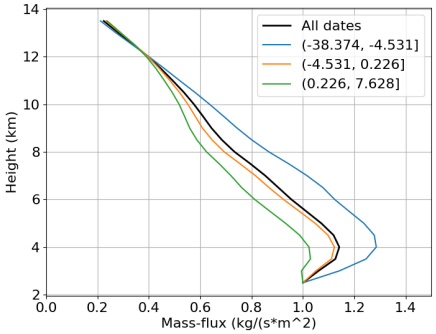

(e) $\overline{\chi_{\text{crit}}}$

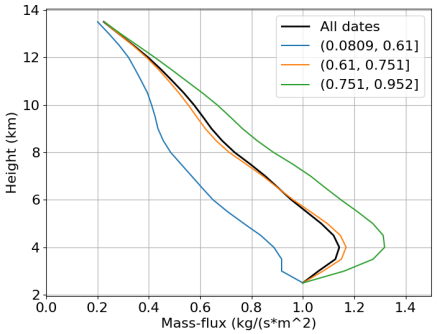

FIGURE 6.8. How environmental parameters affect mean nondimensionalized mass-flux at each level.

CAPE on the strength of mass-flux relative to its value at the base is pronounced also at high levels.

- CIN: The similarities between the effect of CIN and RH_{500} on bulk mass-flux already recorded, can be noticed in Figure 6.8 too. A comparison with Figure 6.5(c) confirms what

hypothesised above: when the absolute value of CIN is large (blue line), bulk mass-fluxes are weaker at 11 km than at the base, although this is not evident in Figure 6.5(c).

- Ω_{500}: Although considerable, the differences between the mean profiles of the three subgroups identified by Ω_{500} are not pronounced at all heights. It appears that Ω_{500} is no longer the most important parameter when looking at mass-flux shape. It must also be recalled that, above 10km, the green line in Figure 6.9(d) is obtained from less than 40% of the profiles used at the base (see Figure 6.4(d)). For this reason, it is reasonable to think that the few profiles extending to this level under subsiding condition behave differently from what shown at low levels by the green line. Indeed, the latter is obtained with a majority of weak mass-fluxes at low altitudes.

- $\overline{\chi_{\text{crit}}}$: Differently from what stated for Ω_{500}, it can be noticed that $\overline{\chi_{\text{crit}}}$ performs very well in distinguishing bulk mass-fluxes for their shape, other than for their magnitude. From Figure 6.9(e) it can be argued that when $\overline{\chi_{\text{crit}}}$ is greater than 0.75 the peak of mass-flux (at 4 km) is stronger than in other condition, this is on average more than 1.3 times stronger than the mass-flux at 2.5 km. If $\overline{\chi_{\text{crit}}}$ is in the lower part of the distribution (blue line), the mass-flux is on average monotonically decreasing from 2.5 km and, at 8 km, is already 50% of its initial value.

Dates binned with K-means clustering

The way of showing results from K-means clustering of mass-flux profiles is repeated and used here for nondimensionalized mass-flux profiles. In Figure 6.9 the colour and group names refer to the clusters identified in Figure 5.14.

The fourth group (yellow) contains 11.2% of the dates in the data set and the most numerous is Group 2 (red) with 33% of all instances of time. Group 1 (blue) is made of profiles with monotonically decreasing mass-flux; Group 3 (green) is characterised by mass-fluxes strongly increasing up to 4 km and then rapidly decreasing; the fourth group shows an even greater mean increase of mass flux at low levels but a slow decrease of this after 4 km and a second peak of mass-flux at 11 km. These four groups of profiles are associated with different distribution of large scale parameters.

It can be observed in Figure 6.8(b) that, when the bulk mass-flux profile presents a bimodal shape (Group 4), CAPE's distribution is shifted to greater values. In light of what stated so far about the role of Ω_{500} on the mass-flux magnitude and looking at Figure 6.8(d), it is spontaneous to assume that bulk profiles with no increase in magnitude (blue group) are also the weakest and indeed, associated with values of Ω_{500} close to zero as shown in Figure 6.9(d). On the same line, it is possible to formulate the hypothesis that the value of mass-flux at 2.5 km (used for the

(a) RH_{500}

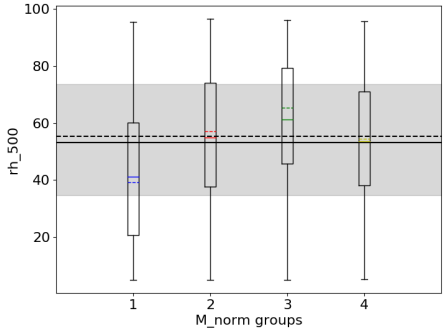

(b) CAPE

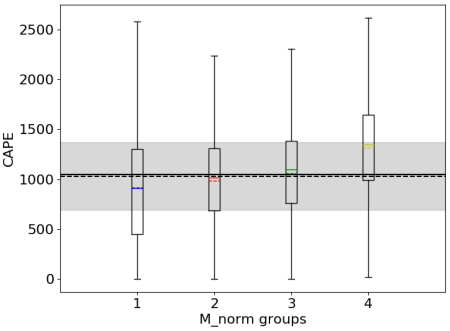

(c) CIN

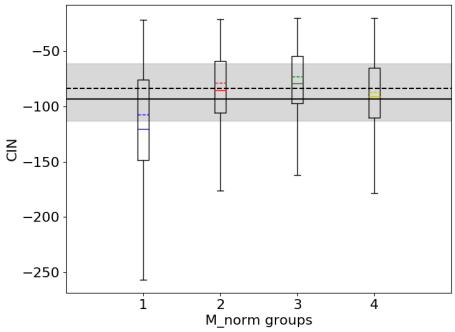

(d) Ω_{500}

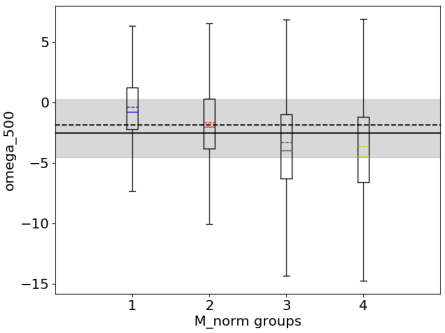

(e) $\overline{\chi_{\text{crit}}}$

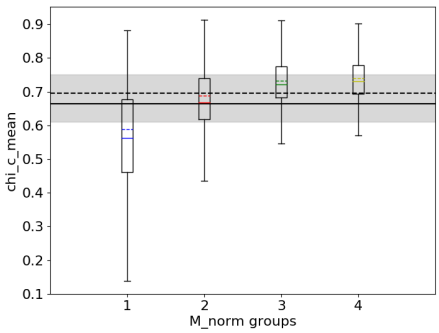

FIGURE 6.9. Parameters' distribution. As in Figure 6.6 but groups are identified applying the K-means clustering algorithm to the nondimensionalized mass-flux profiles. Colours are assigned to groups as done in Figure 5.14.

normalisation) determines how much this will increase in the next few kilometres. The relevance of mass-flux at 2.5 km is already, briefly investigated at the beginning of this chapter and here is confirmed.

Looking at how the distribution of $\overline{\chi_{\text{crit}}}$ changes with the four clusters (Figure 6.8(e)), it is further validated the fact that the shape of mass-flux is deeply linked to $\overline{\chi_{\text{crit}}}$. The greater the increase of mass-flux from 2.5 to 4 km, the greater is $\overline{\chi_{\text{crit}}}$. The small difference between the distribution of this parameter in Group 3 and Group 4 tells that the shape at higher levels is less related to $\overline{\chi_{\text{crit}}}$ (already noticeable in Figure 6.8(e)).

To correctly interpret the results, it must be reminded that the value of mass-flux at 2.5 km was proven to be representative of the entire profile. This makes believe that normalising mass-fluxes by their value at the base and subsequently grouping similar profiles (K-means algorithm), does not completely exclude a dependency on mass-flux magnitude. A further step in trying to decouple the shape of a mass-flux profile from its magnitude is taken by performing partial derivatives.

Mass-flux derivative

The vertical derivative of mass-flux is calculated for each bulk profile and normalised at every level by its value of mass-flux obtaining, for all instances of time, the quantity $\frac{1}{M}\frac{\partial M}{\partial z}$. The results, grouped using the five parameters already introduced, are presented in Figure 6.10 as temporal means.

To interpret Figure 6.10 it is useful to recall that positive values of $\frac{1}{M}\frac{\partial M}{\partial z}$ imply increasing mass-flux, while negative values result from a decreasing mass-flux, this is because in this work M is always positive. The more negative the derivative, the less pronounced is the decrease with height of mass-flux, while when positive, the grater the derivative, the faster is the increase of mass-flux with height. Nevertheless, because of the normalisation, the quantity in Figure 6.10 represents the increase or decrease of mass-flux relatively to its strength. It is also important to remember that the derivatives shown are not directly obtained differentiating the profiles in Figure 6.5 but are mean values of profiles obtained performing the derivative at each instance of time. The time averaging is performed, as done for all other profiles shown above, at each level individually. The expression $\frac{1}{M}\frac{\partial M}{\partial z}$ has no mathematical (and physical) meaning at heights where there is no convection, for this reason the number of instances available to perform the mean decreases with height.

As anticipated, CAPE appears to be relatively important in determining the shape of bulk mass-flux, especially above 6 km. On the contrary, Figure 6.10(d) suggests that Ω_{500} is not relevant for mass-flux shape, this can be said because all the lines are close to each other. This result is not in line with what shown in Figure 6.8(d) but confirms the hypothesis formulated above regarding the role of mass-flux at 2.5 km and the fact that the profiles of Figure 5.14, although dimensionless, carry information about the intensity of mass-flux.

(a) RH_{500}

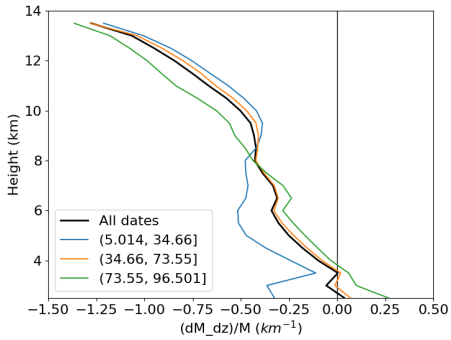

(b) CAPE

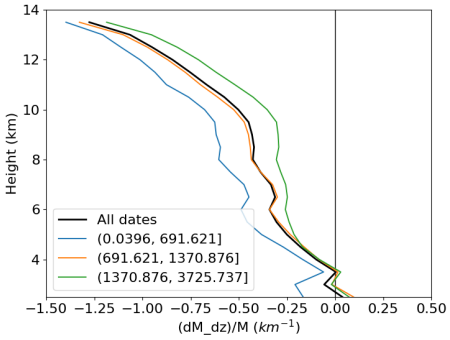

(c) CIN

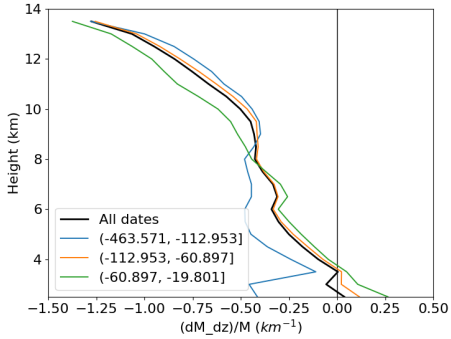

(d) Ω_{500}

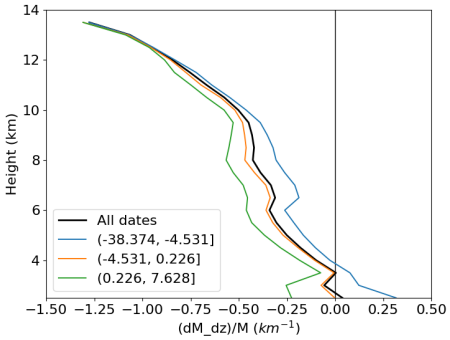

(e) $\overline{\chi_{\text{crit}}}$

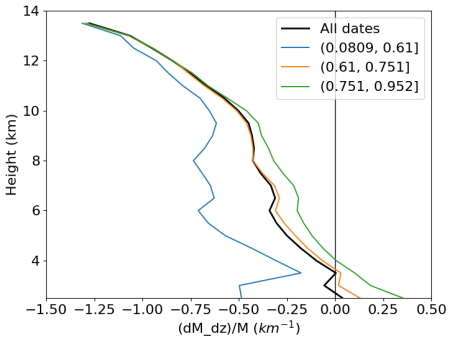

FIGURE 6.10. Mean mass-flux derivative. The quantity $\frac{1}{M}\frac{\partial M}{\partial z}$ is grouped using the parameters' distribution and different colours are assigned to the mean of each group as done in Figure 6.5.

The correlation between RH_{500} and CIN is confirmed to be important also for the role that these two parameters have on the shape of mass-flux. In both cases (Figure 6.10(a) and Figure 6.10(c)) the mean profile associated with the lower tail of the parameter's distribution (blue line) is more negative than in other conditions up to 8 km. After 8 km, in both the sub-figures, the blue

line crosses the mean black line and becomes less negative than other profiles. The behaviour described confirms the fact that for both RH_{500} and CIN the blue line refers to bulk mass-fluxes decreasing slowly below 8 km but relatively fast above 8 km. Under the same environmental conditions, it can be noticed that mass-flux has its maximum value at 2.5 km because always decreasing from this level.

The parameter that seems to be most linked to the mass-flux derivative, at least up to 10 km, is $\overline{\chi_{\text{crit}}}$. Low values of this parameter are common to bulk profiles slowly decreasing with height. The fact that the blue line in Figure 6.10(e) is always negative confirms that, on average, the mass-fluxes falling in this group, have their maxima at 2.5 km.

In Chapter 5.5 it is mentioned that the quantity $\frac{1}{M}\frac{\partial M}{\partial z}$ coincides with the net effect of fractional entrainment and detrainment. Therefore, what stated in this section demonstrates that entrainment processes are partially related to environmental condition. Among the parameters used in this work, the most relevant to this relationship are $\overline{\chi_{\text{crit}}}$ and CAPE. More insights can be gained by looking at entrainment processes using the entraining plume equation introduced in Chapter 5.5.

6.3 Entraining plume equation

One of the most interesting findings of this work comes from the analysis of the entraining plume equation (Equation 5.26). Thanks to the long data set and reliable measurements of updraft vertical velocity and area fraction, it is possible to study the distribution of net fractional entrainment, as well as the distribution of velocity and area components.

In Figure 6.11, the probability distribution of $\frac{1}{M}\frac{\partial M}{\partial z}$, $\frac{1}{A}\frac{\partial A}{\partial z}$ and $\frac{1}{\rho w}\frac{\partial \rho w}{\partial z}$ is depicted using a series of histograms: the probability density function is defined at every height so that, differently from Figure 6.1, the sum of probability is one for each level. The height of histogram bars is given by the colour: where red is more intense, more profiles belong to the histogram bar. With this type of figure no information regarding the amount of profiles at each level is provided. However, it becomes easy to see if the distribution of the quantity on the x-axis changes with height.

Figure 6.11(a) clearly shows that, below 4.5 km, entrainment dominates over detrainment: almost 75% of the profiles are positive as indicated by the only slightly negative first quartile (dotted line). Above this level it becomes hard for bulk convection to experience net entrainment although the probability of net entrainment increases again at 10 km. In general the overall effect is of small and constant detrainment between 5 and 10 km and strong, increasing detrainment at higher levels.

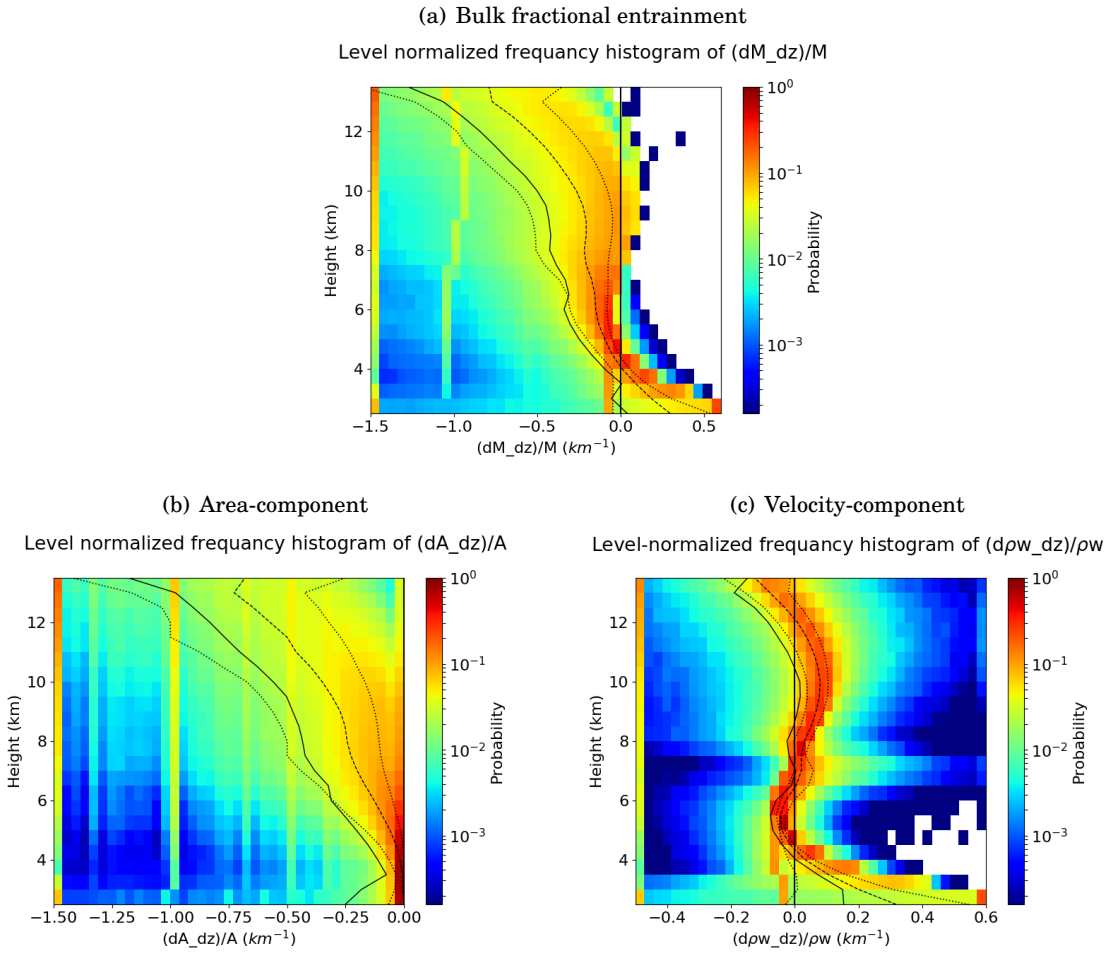

FIGURE 6.11. Probability distribution of $\frac{1}{M}\frac{\partial M}{\partial z}$ (Figure 6.11(a)), $\frac{1}{A}\frac{\partial A}{\partial z}$ (Figure 6.11(b)) and $\frac{1}{\rho w}\frac{\partial \rho w}{\partial z}$ (Figure 6.11(c)) at different heights. The solid line is the mean of the distribution, the dotted lines show the lower and upper quartiles and the dashed line the median. Differently from Figure 6.1, the sum of probabilities is one at each level

A surprising result is highlighted by the probability distribution of $\frac{1}{M}\frac{\partial M}{\partial z}$ around 4.5 km. All the quartiles become particularly close to each other and consequently, the probability density of the mode increases. The 4.5 km level marks, for the large majority of bulk plumes, the height at which $\frac{1}{M}\frac{\partial M}{\partial z}$ goes from positive to negative. This finding is particularly important because demonstrates that height of a bulk plume and environmental condition are not relevant in determining the height at which a plume stops being entrained and starts being detrained.

To further understand the interesting shape of net entrainment shown in Figure 6.11(a), the quantity $\frac{1}{M}\frac{\partial M}{\partial z}$ is broken down into area component of entrainment and velocity component of

entrainment (Figure 6.11(b) and Figure 6.11(c)).

What firstly comes to one's attention is how $\frac{1}{M}\frac{\partial M}{\partial z}$ is mostly similar to $\frac{1}{\rho w}\frac{d\rho w}{dz}$ (right panel) in the lower 6 km, while it follows the distribution of $\frac{1}{A}\frac{dA}{dz}$ (left panel) at higher levels. This makes mathematical sense because the area component is close to zero at low levels for most of the times. Nevertheless, this has several important physical meanings. First of all, it is clear that a convective plume with constant radius is less prone to detrainment than a plume with size varying over height. A second interesting finding is related to the fact that the vertical evolution of area fraction controls the entrainment processes above 6 km, while the shape of vertical velocity profiles dominates the net entrainment in the lower part of a bulk plume. Figure 6.11 also tells that the spread around the mean below 4 km is limited in the area component but not for the velocity component and the opposite occurs above 5 km, where the three quartiles of $\frac{1}{\rho w}\frac{d\rho w}{dz}$ are very close to each other but far apart for the distribution of the area component. The result is that, as noticed above, around 4.5 km the standard deviation of $\frac{1}{M}\frac{\partial M}{\partial z}$ is the smallest.

Another piece of information is retrieved from calculating, at each level, the probability of detrainment. This is obtained summing the probabilities that $\frac{1}{M}\frac{\partial M}{\partial z}$ is negative. The mentioned probability of detrainment is calculated separately for the three sub-set of dates identified with the parameter's distribution and the result is presented in Figure 6.12. For explanatory reasons only CAPE and $\overline{\chi_{\text{crit}}}$ are used here. These two parameters already proved to be the most relevant in analysing $\frac{1}{M}\frac{\partial M}{\partial z}$.

(a) CAPE

(b) $\overline{\chi_{\text{crit}}}$

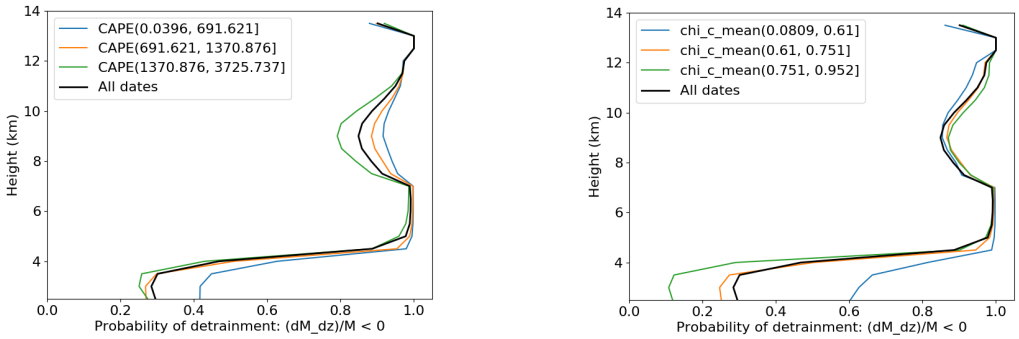

FIGURE 6.12. Probability of detrainment. Each panel refers to one environmental parameter and its effect on the probability of observing detrainment.

Under all circumstances, between 4.5 and 7 km, detrainment dominates over entrainment and the probability of detrainment is close to one. This can be concluded since, at this heights, all lines in Figure 6.12 collapse and take the unity value. At other levels, environmental conditions can

control the probability of having net detrainment, as suggested by the fact that in each panel the three lines are far apart. Figure 6.11 already suggested that the probability of net entrainment increases again around 10 km, this can now be seen clearly in Figure 6.12. Between 7.5 and 12 km the probability of detrainment decreases guided by the value of large scale parameters, but never falls lower than 0.8. As already mentioned, the lowest probabilities of detrainment occur at low levels (2.5 to 3.5 km).

Figure 6.12 further adds to Figure 6.11 the information that environmental conditions are crucial at some levels to determine the sign of $\frac{1}{M}\frac{\partial M}{\partial z}$. In particular, when considering high values of $\overline{\chi_{\text{crit}}}$ (blue line in Figure 6.12(b)), it appears that, at 3 km, it is more likely to have net detrainment than it is to have net entrainment despite the fact that only around 25% of all plumes are detraining at this height (see Figure 6.11(a)).

In line whit what stated above, CAPE is not particularly relevant for entrainment processes at low levels, nevertheless it plays a role around 10 km. Indeed, Figure 6.12(a) suggests that, with very strong CAPE the probability of detrainment falls to 0.8, while for other conditions is around 0.9. Another interesting result disclosed by Figure 6.12 is that, differently from CAPE, $\overline{\chi_{\text{crit}}}$ highlights an inverse proportionality between the probability of detrainment below 4 km and the one around 10 km. Under low $\overline{\chi_{\text{crit}}}$ (blue line) the probability of detrainment at low levels is greater than all other condition but, at 10 km, it is smaller. For CAPE, the blue line indicates higher probability of detrainment both at low levels and around 10 km. Profiles in Figure 6.12 are similar to the detrainment frequency distribution showed by Johnson et al. (1999). This confirms the reliability of the results shown in the present work.

Driving the attention back on Figure 6.11(c), it can be stated that, the probability of measuring detrainment is close to one between 5 and 7 km because the quantity ρw decreases with height in this layer. After a strong increase in vertical velocity in the lower few kilometres (positive values of $\frac{1}{\rho w}\frac{d\rho w}{dz}$), the product ρw becomes constant or slightly decreases around 5 km. This level coincides with the level at which the probability of detrainment is one for most of the bulk plumes and marks an evident threshold height above which detrainment is the dominant process.

Analysing the behaviour of $\frac{1}{\rho w}\frac{d\rho w}{dz}$ above 4.5 km, it can also be stated that this corresponds to the freezing level: after freezing takes place at 4.5 km, vertical velocities start increasing again, driven by the latent heat released with the change of physical state.

Figure 6.13 allows to visualise in one panel the mean profiles of all the components in the entraining plume equation. Numerical approximations are introduced when computing partial derivatives. The residual in Figure 6.13 is defined as

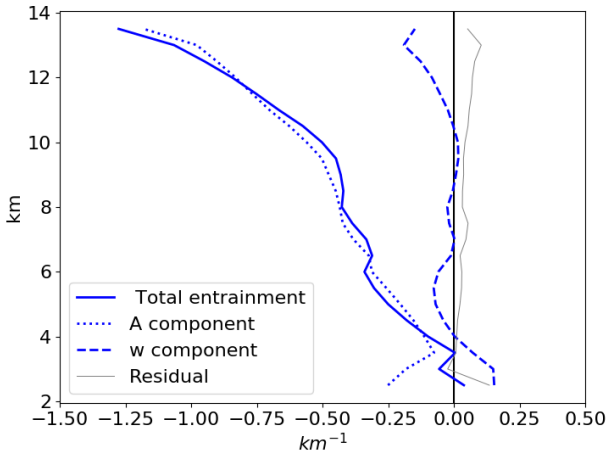

FIGURE 6.13. Mean profiles of bulk entrainment components as described for Equation 5.26.The residual, resulting from discretization errors, is the difference between the solid line and the sum of the dotted and dashed lines.

$$\text{Residual} = \frac{1}{M}\frac{\Delta M}{\Delta z} - \left[\frac{1}{A}\frac{\Delta A}{\Delta z} + \frac{1}{\rho w}\frac{\Delta \rho w}{\Delta z}\right], \tag{6.1}$$

6.4 Contribution of different cloud modes

Previous sections aimed at analysing the bulk mass-flux in light of environmental condition and mass-flux components. Here sub-ensembles are considered and the bulk mass-flux is split into mass-flux from congestus, deep, and overshooting cloud modes. Environmental parameters are not considered in this section, which only sets the starting point for further studies.

In the 13 years of data used for this work and among the cloud modes considered, the most common are deep convective clouds: about 54% of all objects identified are classified as deep convective, 40% are congestus and only 2% overshooting. Despite the overall number of clouds for each mode, congestus clouds are detected in more instances of time (91%) compared to deep convective and overshooting clouds which are observed, respectively, in 77% and 17% of the dates. Table 6.1 summarises the statistics mentioned above and also presents some conditional probabilities: the probability of observing a cloud mode under the condition of having at least one overshooting cloud in the domain ($P_{(mode|\text{over})}$), the probability of having an overshooting cloud given the existence of another cloud mode in the domain ($P_{(\text{over}|mode)}$), the probability of having at least one congestus cloud under the condition of no other cloud modes occurring ($P_{(\text{cong}|\text{no}-mode)}$).

As one would expect, when very tall, overshooting convective towers occur, the probability of

Table 6.1: Cloud mode statistics

	Congestus	Deep	Overshooting
Frequency of occurrence	90.6%	77.3%	16.9%
$P_{(mode)}$	40.0%	53.8%	2.2%
$P_{(mode\|\text{over})}$	93.5%	99.5%	100%
$P_{(\text{over}\|mode)}$	9.8%	10.9%	100%
$P_{(\text{cong}\|\text{no}-mode)}$	$P_{(\text{cong}\|\text{alone})}$: 22.3%	22.6%	75.61%

having other form of clouds in the domain area is high and greater than 90% for both congestus and deep convection. On the contrary, only about 10% of the times with congestus or deep clouds have an overshooting convection too. Interestingly, an exceptional 22.3% of the times, congestus clouds occur in the domain without any other type of precipitating convection ($P_{(\text{cong}|\text{alone})}$)

6.4.1 Mass-flux

The first way of looking at mass-flux under a spectral approach is to show, for each of the three sub-ensembles, its probability distribution, as done for the bulk mass-flux. Figure 6.14 uses a logarithmic scale on the x-axis and the sum of probabilities in the two dimensions (horizontal and vertical axes) is one, allowing to notice a reduction in the number of profiles with height.

Figure 6.14 is firstly analysed for the magnitude of mass-flux. The first and third quartiles (dotted lines) help visualising what range of magnitude majority of the profiles acquire for each of the sub-ensembles. At 2.5 km, the overall mass-flux from congestus clouds is hardly greater than $3 \times 10^{-3}\text{kg}\,\text{s}^{-1}\text{m}^{-2}$. Differently, for deep and overshooting sub-ensembles, 75% of the profiles are, respectively, greater than $2 \times 10^{-3}\text{kg}\,\text{s}^{-1}\text{m}^{-2}$ and $4 \times 10^{-3}\text{kg}\,\text{s}^{-1}\text{m}^{-2}$. It is interesting to notice that the difference in magnitude at low levels is not very pronounced between deep and overshooting modes. This might be linked to the number of objects that comprise the sub-ensembles: an instance of time with deep clouds has, on average, 10.1 objects classified as deep, while an instance of time with overshooting clouds has, on average, 1.3 objects classified as overshooting. The mass-flux of individual clouds is not analysed in this work but the collective effect of clouds belonging to the same mode investigated.

By definition, all profiles in Figure 6.14(c) extend higher than 15 km, this implies that there is no reduction in the sum of probabilities over the levels shown in the figure. Another thing that should be kept in mind when looking at Figure 6.14 is the fact that the number of profiles available is different for each of the three panels: for example, overshooting clouds do not occur in many of the instances of time where other cloud modes are observed.

The statistics presented in Table 6.1 suggest that the three cloud mode sub-ensembles have a different relative contribution to the mean bulk mass-flux. Indeed, the temporal mean of bulk

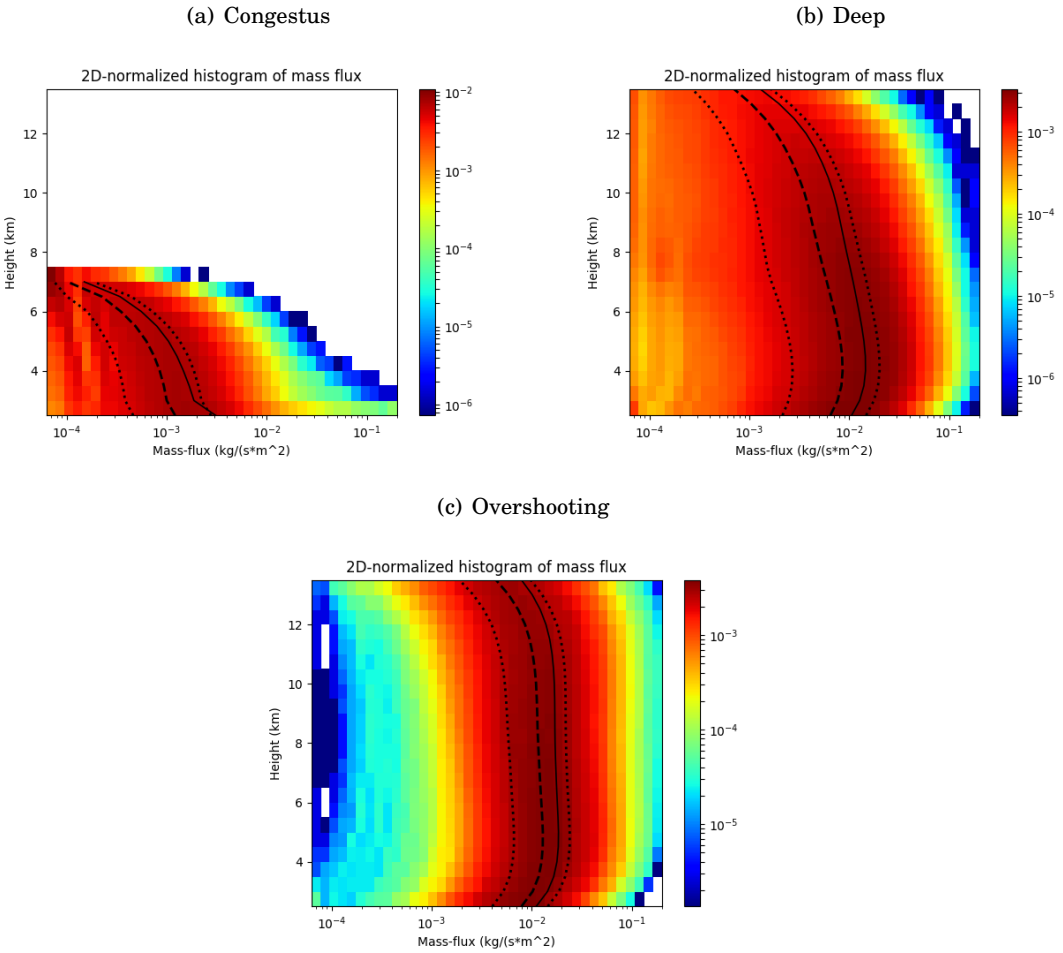

FIGURE 6.14. Probability distribution of mass-flux for three sub-ensembles: congestus, deep and overshooting convection.

mass-flux is not simply the sum of the mean mass-fluxes from congestus, deep and overshooting clouds. The relationship involves a weighting factor:

$$\overline{M} = \sum_{mode} \frac{\overline{M_{mode}} T_{mode}(z)}{T(z)}. \tag{6.2}$$

In Equation 6.2, $T_{mode}(z)$ refers to the number of times a convective mode is observed in the domain at height z and $T(z)$ is the total number of instances of time used to compute the bulk mean at level z. The quantity $\frac{T_{mode}}{T}$ at 2.5 km is listed in Table 6.1 under "Frequency of occurrence".

The relative contribution from the three cloud modes to bulk area fraction, vertical velocity, mass-flux and net entrainment is shown in Figure 6.15. It is interesting to notice how little is the contribution of overshooting convective clouds to the overall bulk mass-flux. Although this

cloud mode is associated with exceptionally strong mass-fluxes inside a single object, the number of object that can occur in one instance of time and the number of times where such clouds are observed are very limited. On average, below 3 km, the collective mass-flux from congestus clouds is larger than the one from overshooting. Nevertheless, the magnitude of mean mass-flux at high altitudes is dominated by the overshooting mode because congestus and deep sub-ensembles reduce in number with height.

(a) Area fraction

(b) Vertical velocity

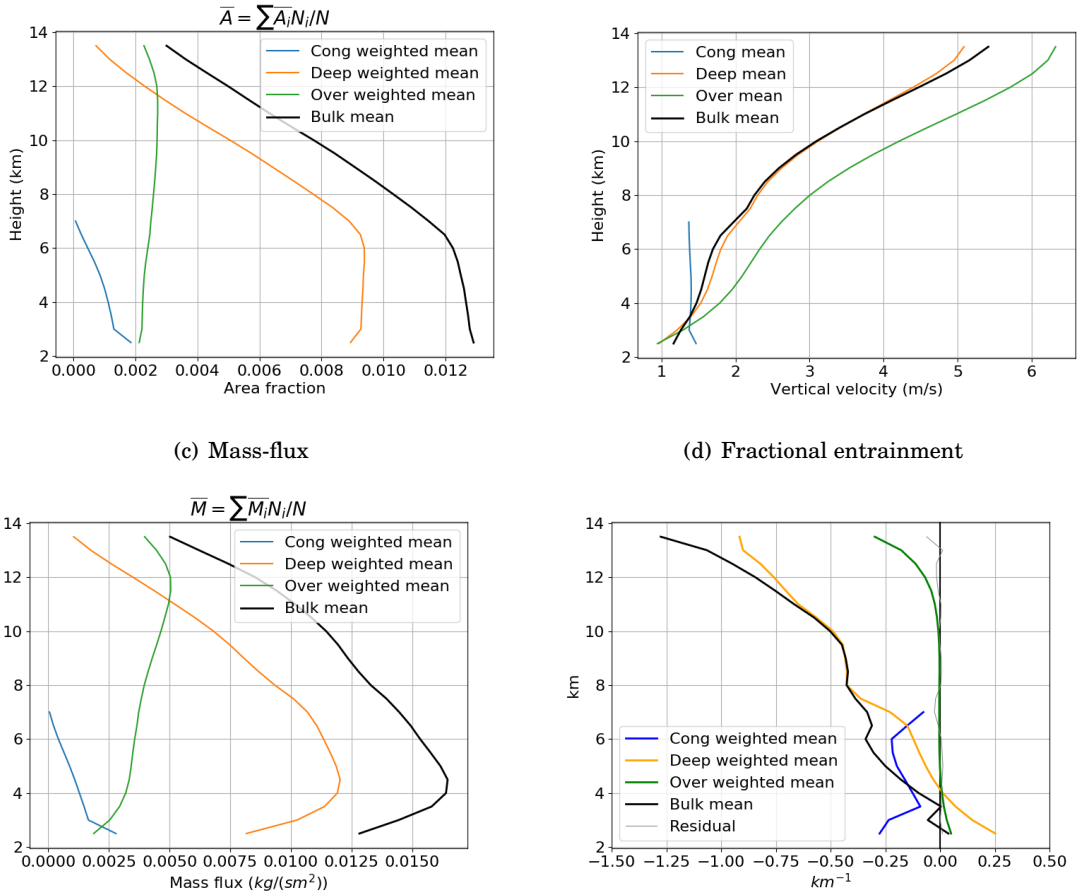

(c) Mass-flux

(d) Fractional entrainment

FIGURE 6.15. Mean relative contribution of cloud sub-ensembles to bulk area fraction (Figure 6.15(a)), vertical velocity (Figure 6.15(b)), mass-flux (Figure 6.15(c)) and fractional entrainment (Figure 6.15(d)). The contribution of each cloud mode ensemble is weighted by its frequency of occurrence where specified by the legend.

Looking at area fraction (Figure 6.15(a)) and vertical velocity (Figure 6.15(b)) for the different cloud modes, it is possible to notice again the role of vertical velocity to the shape of mass-flux at low levels. Taking deep convection as example, the weighted mean area fraction stays more or less constant up to 7 km but, because of an increasing vertical velocity, the weighted mean

mass-flux of this mode increases from 2.5 to 4 km.

Figure 6.15(d) shows the relative contribution of congestus, deep and overshooting modes to the bulk fractional entrainment. A detailed description of the quantity $\frac{1}{M}\frac{\partial M_{mode}}{\partial z}$ is presented in the next section. Here it can be noticed that also for the entraining processes deep clouds give the greatest contribution. Nevertheless, congestus mode is relevant at low levels and overshooting above 12 km. Congestus clouds, where present, drive the bulk fractional entrainment to negative values. As one would expect, small clouds (congestus) are more prone to mixing with the environment because of their smaller ratio volume/surface. This, together with their frequency of occurrence, makes congestus very important.

6.4.2 Entrainment and detrainment

Similarly to what done in the bulk approach, the shape of mass-flux for each cloud mode' sub-ensemble can be studied using the first order partial derivative of M_{mode}. In particular, the three terms on the right hand side of Equation 5.29 are presented in Figure 6.16 using the same type of plot as in Figure 6.11.

Looking at Figure 6.16(a), it is possible to state that the monotonically decreasing trend of mass-flux under congestus mode, is common to all profiles and is not just a mean effect seen in Figure 6.15. Deep and overshooting clouds, rarely have mass-fluxes decreasing with height below 4 km. The level at 4.5 km marks, for both these sub-ensembles, an important threshold. As observed for the bulk approach, the spread of $\frac{1}{M}\frac{\partial M}{\partial z}$ around the mean becomes small around this height and majority of the mass-flux profiles stop increasing. In the case of deep convection, the quantity $\frac{1}{M}\frac{\partial M_{\text{deep}}}{\partial z}$ is, on average, increasingly negative above 4.5 km but the first and third quartiles diverge considerably, indicating that mass-flux profiles can stay constant or even increase. Differently, when looking at the distribution of $\frac{1}{M}\frac{\partial M_{\text{over}}}{\partial z}$, it can be noticed that little variability exists between 4.5 and 10 km. The spread around the mean is limited and the value of the quantity suggests a constant mass-flux between the two levels. In this type of clouds the increase of vertical velocity compensates the decrease of area fraction (and density) with height.

It is mentioned in a previous section that the quantity used to describe mass-flux shape coincides with the net fractional entrainment. This allows to further comment on this mixing process and study it for different cloud modes. Congestus sub-ensembles appear to be always subject to net detrainment above 2.5 km. One hypothesis is that this type of clouds experience entrainment close to cloud base but this is located too far below 2.5 km. Deep clouds seem to have an area where entrainment occurs (below 4.5 km) and an area where detrainment dominates (above 4.5 km). Lastly, three well separated regions are visible for net entrainment in the overshooting sub-ensemble: an area dominated by entrainment (below 4.5 km), one with no net effect

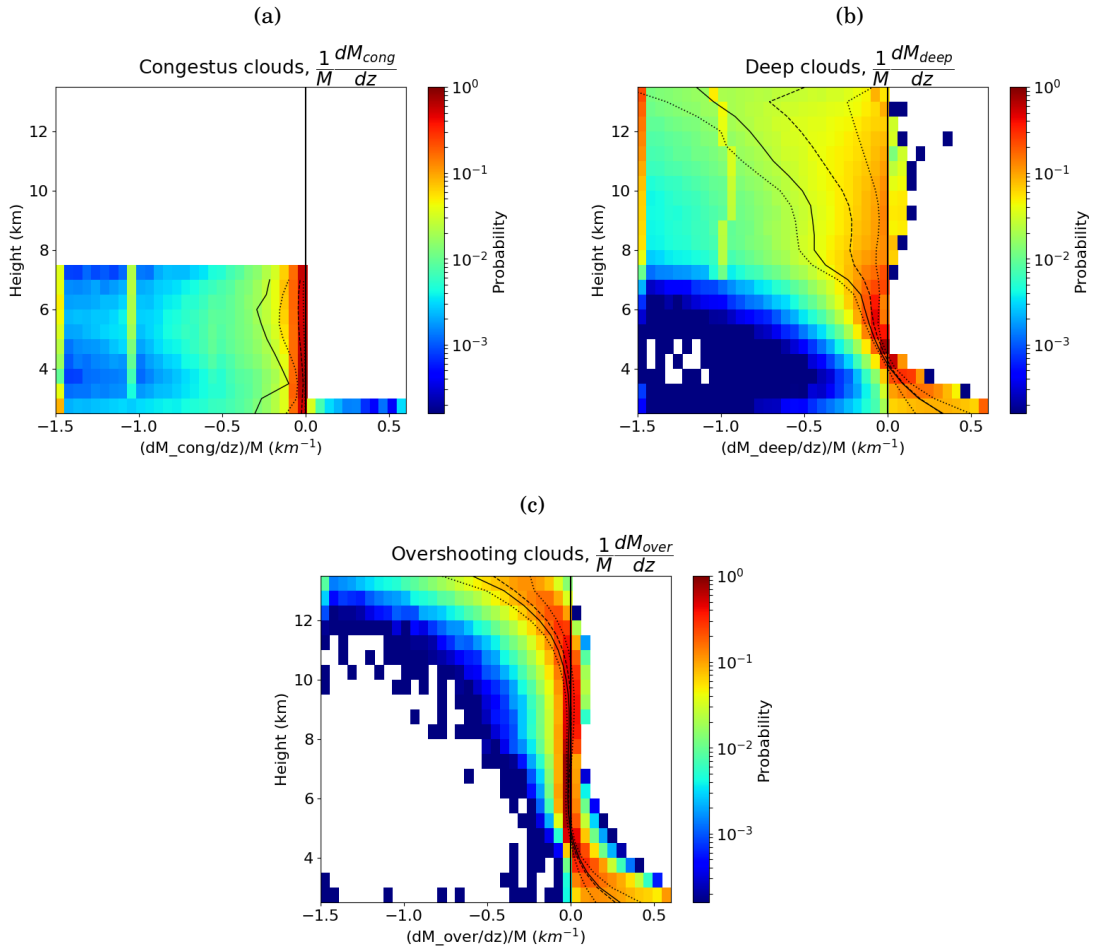

FIGURE 6.16. Probability distribution of $\frac{1}{M}\frac{\partial M_{mode}}{\partial z}$ at different heights for three sub-ensembles: congestus, deep and overshooting convection.

of mixing on the mass-flux (between 4.5 and 10 km) and a top region where detrainment is the strongest mixing process (above 10 km).

CHAPTER 7

DISCUSSION

The sensitivity of mass-flux to environmental conditions presented here is in large agreement with previous studies (Kumar et al., 2015; Davies et al., 2013; Derbyshire et al., 2004). There is evidence that mass flux responds differently to various environmental parameters, making it difficult to relate mass flux itself to only one of them.

Kumar et al. (2015) suggests that CIN influences the bulk area fraction while RH_{500} is more linked to vertical velocity. This correspondence is not noticed in the present work (see Appendix B) but the role of both parameters is recognised as significant to both magnitude and shape of mass-flux.

The previous chapter confirmed the weak effect of CAPE on the bulk mass-flux, nevertheless it is proven that CAPE is relevant to the mass-flux shape and so to the entrainment rate. Previous studies also suggest that CAPE has a negligible role in determining bulk area fraction of convection but it is, instead, linked to cloud growth dynamics and vertical velocity. Figures in Appendix B confirm this and allow to formulate the hypothesis that vertical velocity is linked to the shape of bulk mass-flux while area fraction determines the intensity.

It is noticeable that the findings from Kumar et al. (2015) are in alignment with the role of large scale vertical motion. Above, it is shown that Ω_{500} largely determines the magnitude of mass-flux but it is less relevant than other parameters to the shape of mass-flux.

It appears clear that mass flux magnitude is driven by Ω_{500}, which is a measurement of large scale convergence. As shown by Kumar et al. (2015) and confirmed in Appendix B, Ω_{500} is strongly related to the area fraction and poorly related to the vertical velocity. This supports

the idea that mass-flux magnitude is driven by area fraction, while mass-flux shape by vertical velocity.

To the author's knowledge, no other studies have analysed mass-flux intensity and shape as a function of $\overline{\chi_{\text{crit}}}$. This parameter is most commonly used to infer detrainment rates in convective parameterizations (de Rooy et al., 2008; Kain et al., 1990). As mentioned above, mass-flux shape is linked to entrainment by Equation 2.7; for this reason, it is not surprising that $\overline{\chi_{\text{crit}}}$ relates well to the vertical dynamic of mass-flux. Interestingly, this parameter also appears to be important for mass-flux magnitude. A possible explanation for this can be found in the correlation between $\overline{\chi_{\text{crit}}}$ and RH_{500} (see Figure 5.12(j)).

In their work, Kumar et al. (2015) suggest potential benefits from treating area and velocity separately in future cumulus parameterization approaches. Here it is confirmed that the two components act on different characteristics of mass-flux: magnitude and shape. This work further suggests that vertical velocity should not be disregarded in such parameterizations since it is relevant to determine mass-flux dynamics and, in turn, entrainment. Studies mentioned above hardly make a separation between magnitude and shape of mass-flux profiles. For this reason, it is often suggested the tempting, but simplistic, conclusion that mass-flux characteristics can be modelled only through convective area fraction.

The results presented above show that the mean bulk mass-flux increases from 2.5 km to 4 km and then gradually decreases with height. Differently, Kumar et al. (2015) concluded that the bulk mass-flux peaks around 6 km: above the freezing level (see Figure 7.1). The mismatching

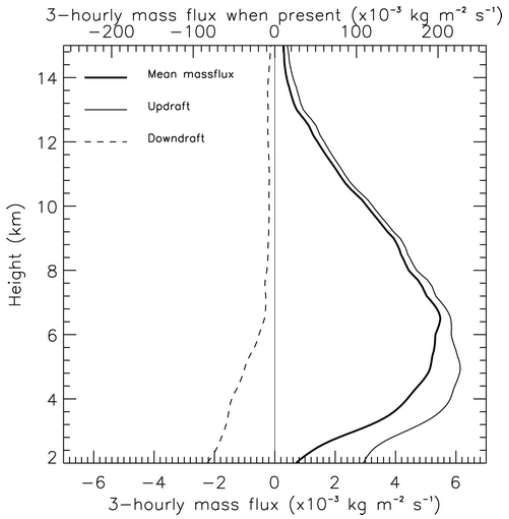

FIGURE 7.1. Mean mass-flux profiles obtained by Kumar et al. (2015). The downdrafts are taken into account.

height of maximum mass-flux might be linked to the fact that the present research disregards any downdraft vertical velocity. According to Kumar et al. (2015), the bulk mass-flux from only updrafts peaks at 4.5 km, this result is more in line with what is shown in Chapter 6. Another study from Giangrande et al. (2016) applies a similar analysis in the Amazon and states that the ensemble mass-flux profiles increase from cloud base and peak near 8 km. The mean profiles are dominated by updrafts except from low levels where downdrafts play a greater role. Downdrafts act to reduce mass-flux at low levels and they smooth the updraft peak.

Some of the results shown in Chapter 6 go beyond the initial goals and hypothesis of this work. Unexpectedly, the shape of vertical velocity profiles (see Figure 6.11(c)) appears to be showing a persistent freezing level at 4.5 km. This stable layer, commonly observed in tropical regions (Johnson et al., 1996), is usually investigated through energy balances and heat dynamics. One of the few studies using vertical velocity profiles to detect vertical mass convergence and relate it to levels where net latent heating occurs is from Posselt et al. (2008). Vertical mass convergence is associated with significant vertical moisture convergence, which leads to a spike in the latent heating profiles. In line to what shown in the mentioned article, averaged vertical velocities peak just below the freezing level, reduce to a local minimum at 4.5 km and increase again up to 10 km. Posselt et al. (2008) also noticed that cooling occurs below the freezing level in a limited vertical space, while radiative warming occurs above, up to around 10 km. Although results from Posselt et al. (2008) come from means of only 10 simulated days, the characteristics of the stable layer near the freezing level under radiative convective equilibrium (RCE) are well captured. The present research demonstrates that the same stratification and profile can be observed using domain and time average over a considerably longer data set.

The vertical derivative of mass-flux calculated every 10 minutes for 13 wet seasons and shown in this work adds important information to what is known regarding the atmosphere inside the tropics. Firstly, the bulk approach (Figure 6.11) allows to comment on the different roles of area component and velocity component of entrainment. The area fraction appears relevant to determine detrainment above 5 km while the shape of vertical velocity dominates the mixing processes below the freezing level and leads to net entrainment.

The parameter χ_{crit} can be used to further investigate the links between mass-flux components and mixing processes. It was mentioned above and can be seen in Appendix B that $\overline{\chi_{\text{crit}}}$ is more strongly related to the area fraction than it is to the vertical velocity. de Rooy et al. (2008) also noticed that χ_{crit} is considerably more relevant to determine detrainment than it is for entrainment.

It is tempting to conclude that detrainment determines area fraction while entrainment determines vertical velocity but it has to be recalled that in this work two approximations are made:

area fraction can only decrease with height and downdraft velocities are excluded. Nevertheless it can be said that entrainment dominates below 4.5 km while detrainment is the main mixing process above this level.

A spectral approach allows to further investigate entrainment and detrainment. According to the results of this work, a sub-ensemble obtained by grouping together only congestus clouds never experiences entrainment above 3 km. The overshooting sub-ensemble presents a thick layer between 5 and 10 km where no net mixing occurs (constant mass-flux with height). The deep convection sub-ensemble shows a probability distribution of $\frac{1}{M}\frac{\partial M}{\partial z}$ more similar to the one observed in the bulk approach. Results from the spectral approach point at the conclusion that deep convective clouds are on average the most important in determining the overall mass-flux and entrainment process in a 70.000km^2 domain over the tropics.

CHAPTER 8

CONCLUSIONS

In this work, an exceptionally long data set from the C-band polarimetric radar in Darwin (Australia) is used to estimate vertical velocity inside convection. Subsequently mass-flux over a domain similar to the size of a GCM grid box is derived. The method to obtain mass-flux from radar reflectivity measurements has been described and evaluated by Kumar et al. (2016). In the present thesis the accuracy of the estimates is not further tested, although limitations of the method are reported and taken into consideration. The aim is to evaluate, through this observational data set, the relationship between mass-flux and large scale environmental conditions in a tropical region, over a period of 13 wet seasons.

A first conclusion concerns the value of mass-flux at 2.5 km, this is proven to be critical in characterising the profile at all levels. The retrieval of mass-flux at few critical heights could be sufficient for a satisfactory description of mass-flux over a large domain.

The large scale parameters drive different aspects of mass-flux. For instance, CAPE is proven to be relevant for vertical velocity but is not playing a role in determining area fraction. The opposite is observed for Ω_{500}. It can be confirmed that large scale environmental conditions are strictly linked to the vertical transport of mass inside convection. Parameterizing area fraction and vertical velocity as independent components of mass-flux could allow for more exhaustive representations of the process. Multiple parameters of the large scale forcing are required to capture all aspects of mass-flux in a parametric model.

With the results shown in this study it is possible to further conclude that the selected parameters also affect mass-flux shape and magnitude. This suggests a relatively unexplored correlation be-

tween area fraction and mass-flux magnitude and between vertical velocity and mass-flux shape. A combination of the parameters used here could be taken to put forward a parameterization of mass-flux. Shape and magnitude of the profile should be kept separate when designing this convective scheme.

A parameter borrowed from the buoyancy sorting concept (χ_{crit}) is also used to characterise mass-flux and its components. Differently from all other parameters used, the column mean fraction of environmental air needed to make a rising parcel neutrally buoyant ($\overline{\chi_{\mathrm{crit}}}$) is substantially affecting both mass-flux magnitude and shape. The results show that, when $\overline{\chi_{\mathrm{crit}}}$ is greater than 0.75, bulk mass-flux can become considerably strong and convection can more easily reach high altitudes. Under the same condition, mass-fluxes show a great increase up to 4.5 km and a strong decrease at higher levels, compared to a slow decrease of mass-flux occurring already at 2.5 km in the cases of small $\overline{\chi_{\mathrm{crit}}}$. It is suggested that $\overline{\chi_{\mathrm{crit}}}$ is a key parameter in determining mass-flux and future parameterizations should take it into account.

Partial derivatives are also used to characterise mass-flux shape. This is proven to be strongly dominated by the vertical gradient of ρw below 4.5 km and more largely affected by changes in area fraction at higher levels.

While previous studies (Majda et al., 2013; Kumar et al., 2015) have suggested to parameterize mass-flux using only area fraction, the analysis proposed here suggests that this idea, although tempting, is biased by the fact that area fraction dominates mass-flux magnitude. After decoupling shape and magnitude of mass-flux profiles, it is here concluded that vertical velocity is crucial to define levels of increasing or decreasing mass-flux. A first order characterisation of mass-flux using only area fraction would largely misrepresent the shape of the profile and also lead to poor estimates of dynamical entrainment processes.

Entrainment hardly occurs above 4.5 km but it largely prevails over detrainment below this level. When present, the transition between a dominant entraining process to a dominant detraining process occurs remarkably often at 4.5 km. Under all conditions the layer between 4.5 and 7 km experiences detrainment. This highlights the presence of a stable layer, also known as freezing level, at 4.5 km.

This work clearly demonstrates the great potential to estimate convection, through the use of observational estimates of mass-flux, from radar reflectivity measurements.

8.1 Recommendations

In light of the assumptions and limitations described in Chapter 5.6, future works should add details and try to reduce the errors resulting from these approximations. An equation describing downdrafts inside convection as function of radar measurements can be added to Equation 5.5 to make vertical velocity profiles more realistic. To this extent, the use of machine learning is promising in finding patterns and correlations between vertical velocity and radar reflectivities. This approach would, perhaps, reduce fundamental limitations of this work deriving from the use of Equation 5.5.

More insights on the role played by environmental condition on convective mass-flux can be gained using the five large scale parameters (RH_{500}, CAPE, CIN, Ω_{500} and $\overline{\chi_{\text{crit}}}$) to analyse the cloud sub-ensembles. A similar method to the one used for bulk-mass fluxes can be used on the spectral approach. Numerous more analysis can also be performed on the CPOL data set when grouping together clouds of the same mode.

To further investigate the presence and importance of a freezing level at 4.5 km in the study area, atmospheric stability and radiative processes should be taken into account in future works. A more in depth study should aim at understanding if the environmental conditions determine the height of the freezing level.

Temporal variability is disregarded in the present work and quantities such as mass-flux are investigated at every level independently: the instances of time with active convective pixels at 10km are less than the instances of time with active convective pixels at 2.5 km. Appendix C shows initial results from an approach that defines the total number of instances at 2.5 km and keeps it constant with height. Different insight can be acquired if the mean mass-flux at a level is calculated assigning zero when convection is not measured at that level. This approach allows to retrieve a climatological mass-flux profile regardless of the height of convection.

A temporal analysis of the available data set could help answering questions related to seasonal variability, diurnal cycle of convection and even the evolution of individual convective systems. Johnson et al. (1999) already noticed some inter-seasonal oscillation of cloud mode population in tropical areas.

In addition to what suggested above, the exceptionally long data set provides a unique opportunity to investigate inter-annual variability of mass-flux. It should be questioned if the number of days with convection has increased since 2001 or if there has been a change in the intensity of mass-fluxes and area fraction cover. Answering these questions can help to understand the role of a changing climate on tropical convection and, perhaps, the feedback of the latter on

weather and climate.

APPENDIX A

CRITICAL FRACTION OF ENVIRONMENTAL AIR

This appendix shows an analytical derivation of the quantity, χ_{crit}, used above as a parameter to describe environmental conditions. χ_{crit} represents the concentration of environmental air for which the buoyancy of a rising air mixture is just zero. In Chapter 5, this parameter is approximated with the following equation:

$$\chi_{\text{crit}}(h) = \frac{\Delta\theta_{\text{v}}}{\beta\Delta\theta_{\text{l}} + \frac{(\beta-\alpha)L}{c_{\text{p}}\pi}\Delta q_{\text{t}}}. \tag{A.1}$$

This formulation was proposed by de Rooy et al. (2008) and the steps followed to derive it are here repeated.

If χ is the fraction of environmental air in a mixture, the virtual potential temperature of this mixture reads:

$$\theta_{\text{v},\chi} = \theta_{\chi}\left[1 + \lambda q_{\text{v},\chi} - q_{\text{l},\chi}\right] \tag{A.2}$$

where the subscript χ is used for properties of the air mixture; $\lambda = R_{\text{v}}/R_{\text{d}} - 1$ with $R_{\text{v}} = 461.39$ J/(kgK) being the gas constant for moist air and $R_{\text{d}} = 287$ J/(kgK) the gas constant for dry air. q_{v} is the water vapour specific humidity, q_{l} is the liquid water specific humidity.

The aim of this derivation is to describe $\theta_{\text{v},\chi}$ as a function of cloudy or purely environmental properties. χ_{crit} will be attained equating this function to $\theta_{\text{v,e}}$. Where the subscript e refers to the fact that the variable is measured in the environment. Similarly the subscript c will be used for cloudy properties.

From Equation A.2 it is possible to eliminate q_{v} and θ in favour of moist conserved variables: q_{t} and θ_{l}. The following relations are used:

$$\begin{aligned} q_{\mathrm{t}} &\equiv q_{\mathrm{v}} + q_{\mathrm{l}}, \\ \theta_{\mathrm{l}} &\approx \theta - \frac{L q_{\mathrm{l}}}{c_{\mathrm{p}} \pi}. \end{aligned} \tag{A.3}$$

$L = 2264$ J/kg is the latent heat of vaporisation, $c_{\mathrm{p}} = 1004$ J/(kgK) is the specific heat capacity of dry air and $\pi = (\frac{p_0}{p})^{(-R_d/c_p)}$ is the Exner function.

Equation A.2 becomes:

$$\theta_{\mathrm{v},\chi} = \theta_{\mathrm{l},\chi}\left[1 + \lambda q_{\mathrm{t},\chi} - (1+\lambda) q_{\mathrm{l},\chi}\right] + \frac{L}{c_{\mathrm{p}} \pi} q_{\mathrm{l},\chi}. \tag{A.4}$$

Conserved variables mix linearly, as a result, it is possible to write

$$\begin{aligned} q_{\mathrm{t},\chi} &= q_{\mathrm{t,c}} - \chi \Delta q_{\mathrm{t}}, \\ \theta_{\mathrm{l},\chi} &= \theta_{\mathrm{l,c}} - \chi \Delta \theta_{\mathrm{l}}. \end{aligned} \tag{A.5}$$

To find an expression for $q_{\mathrm{l},\chi}$ as a function environmental and in-cloud variables, the quantity has to be written as function of total specific humidity ($q_{\mathrm{t},\chi}$) and saturation specific humidity ($q_{\mathrm{s}}[p, T(\chi)]$):

$$q_{\mathrm{l},\chi} = q_{\mathrm{t},\chi} - q_{\mathrm{s}}[p, T(\chi)]. \tag{A.6}$$

Equation A.6 is valid when $q_{\mathrm{l},\chi} > 0$, this is the case with $0 \leq \chi \leq \chi_{\mathrm{crit}}$.

The second term on the right hand side of Equation A.6 can be approximated with a Taylor series calculated around $T(\chi = 0) \equiv T_{\mathrm{c}}$:

$$q_{\mathrm{s}}[p, T(\chi)] \approx q_{\mathrm{s}}(T_{\mathrm{c}}) + \left[T_\chi - T_{\mathrm{c}}\right] \left.\frac{\partial q_{\mathrm{s}}}{\partial T}\right|_{T_{\mathrm{c}}}. \tag{A.7}$$

After defining

$$\begin{aligned} \gamma &= \frac{L}{c_{\mathrm{p}}} \left.\frac{\partial q_{\mathrm{s}}}{\partial T}\right|_{T_{\mathrm{c}}}, \\ \frac{\partial q_{\mathrm{s}}}{\partial T} &= q_{\mathrm{s}} \frac{L}{T^2 R_{\mathrm{v}}}. \end{aligned} \tag{A.8}$$

Equation A.6 can be written as:

$$q_{\mathrm{l},\chi} = q_{\mathrm{l,c}} - \chi \frac{1}{1+\gamma}(\Delta q_{\mathrm{t}} - \gamma \Delta \theta_{\mathrm{l}}). \tag{A.9}$$

Finally, substituting Equation A.9 and Equation A.5 into Equation A.4 the following is found.

$$\theta_{\mathrm{v},\chi} = \theta_{\mathrm{v,c}} - \chi \left[\beta \Delta \theta_{\mathrm{l}} + (\beta - \alpha) \frac{L}{c_{\mathrm{p}} \pi} \Delta q_{\mathrm{t}} \right], \tag{A.10}$$

with

$$\begin{aligned} \alpha &\equiv \frac{c_{\mathrm{p}} \pi}{L} \theta_{\mathrm{l,c}}, \\ \beta &\equiv \frac{1}{1+\gamma} \left[1 + (1+\lambda)\gamma\alpha \right]. \end{aligned} \tag{A.11}$$

Equation A.10 defines $\theta_{\mathrm{v},\chi}$ as a function of purely environmental an cloudy variables, when $\theta_{\mathrm{v},\chi} = \theta_{\mathrm{v,e}}$ then $\chi = \chi_{\mathrm{crit}}$ and Equation A.1 is obtained.

APPENDIX B

ADDITIONAL FIGURES

This appendix shows mean profiles of mass-flux components.

Similarly to what done in Chapter 6 (Figure 6.5) for mass-flux, here the mean area fraction and vertical velocity are presented as function of environmental parameters. It is important to notice that the quantity represented in Figure B.1 is the product of vertical velocity and density.

Figure B.1 confirms the hypothesis that CAPE has a small impact on the bulk area fraction while large scale vertical motion is crucial to determine this term. $\overline{\chi_{\text{crit}}}$ also appears to be driving area fraction.

Figure B.2 shows that vertical velocity inside convection is not affected by Ω_{500}, while it is related to the value of RH_{500} and CIN. CAPE is also relevant to vertical velocity, especially at high altitudes. $\overline{\chi_{\text{crit}}}$ appears to be only marginally linked to vertical velocity.

(a) RH_{500}

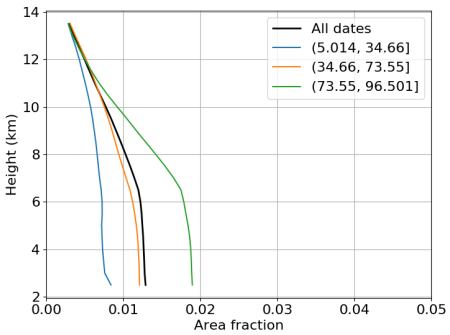

(b) CAPE

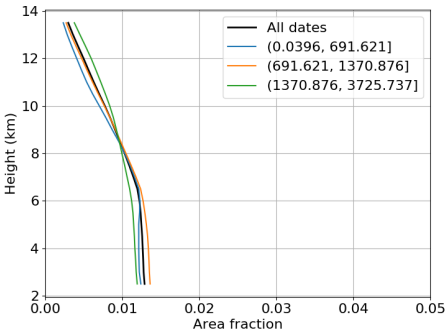

(c) CIN

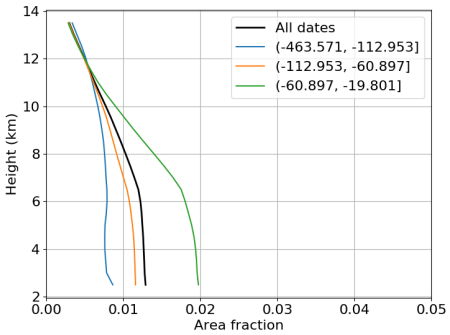

(d) Ω_{500}

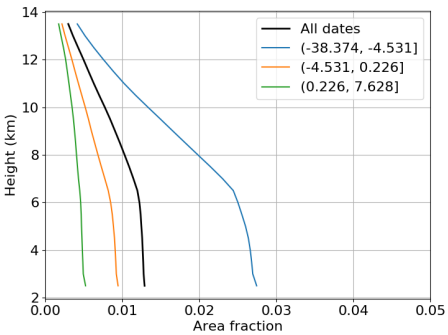

(e) $\overline{\chi_{\text{crit}}}$

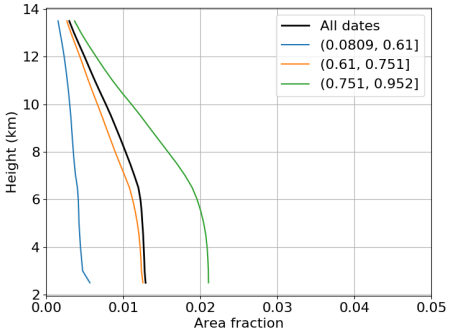

FIGURE B.1. How the mean bulk area fraction profile is influenced by the environmental parameters

(a) RH_{500}

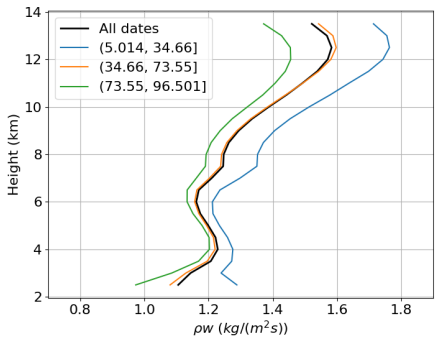

(b) CAPE

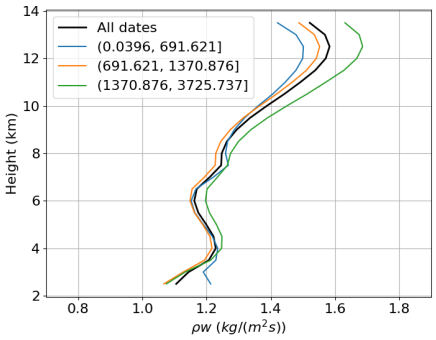

(c) CIN

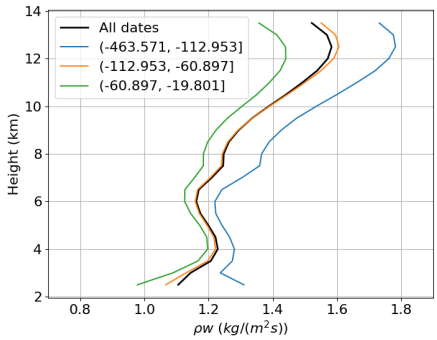

(d) Ω_{500}

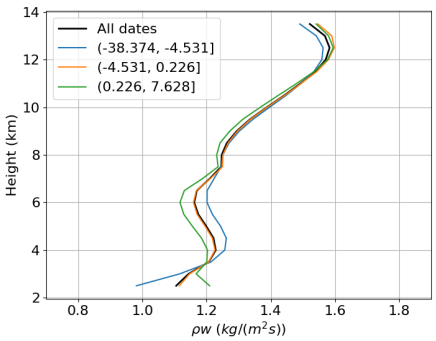

(e) $\overline{\chi_{\text{crit}}}$

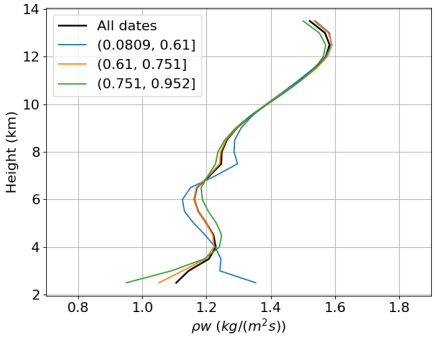

FIGURE B.2. How the mean profile of the product ρw is influenced by the environmental parameters

APPENDIX C

TEMPORAL AVERAGING

This appendix suggests a variation to the methods used above.

The alternative method regards the way of defining a sub-set of dates within the wet seasons to be used for statistical analysis. Chapter 5 shows how this is done at each height independently using the condition that at least one pixel in the domain, at the selected height, is convective.

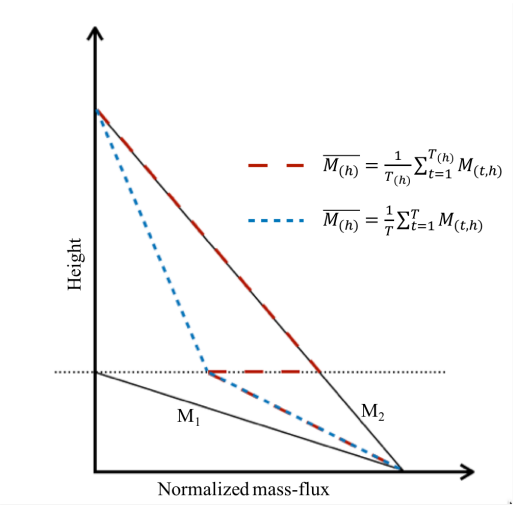

FIGURE C.1. Sketch showing two approaches of averaging mass-flux. Red dashed line is obtained excluding, at each height, instances of time with no convection occurring. Blue dashed line is obtained assigning zero to the value of mass-flux at heights where convection is not occurring.

Instead of selecting, for each height level, only the instances of time where convection is recorded, a constant number of instances can be defined for all levels. In this appendix an instance of time is included in the data set of all levels if it shows convection at 2.5 km. Another alternative might be to use in the statistics all instances of time with precipitation at the surface. This allows to take into account convection with ETH lower than 2.5 km.

In this appendix, statistics (e.g. mean) are computed assigning zero to the value of area fraction and mass-flux of above the level of 0-dBZ ETH.

Defining T as the number of instances in the data set, the temporal mean computed with the two approaches described can be expressed with the following equations.

$$\overline{M(h)} = \frac{1}{T(h)} \sum_{t=1}^{T(h)} M(t,h) \tag{C.1}$$

$$\overline{M(h)} = \frac{1}{T} \sum_{t=1}^{T} M(t,h) \tag{C.2}$$

Equation C.1 is used to produce results shown in Chapter 6 and $T(h)$ indicates that T is a function of height. Less instances of time are used at high altitudes compared to the one used at 2.5 km because convection does not always reach certain heights.

Equation C.2 is used to produce results shown in this appendix. In this case T is constant with height and it is equal to the number of instances showing convection at 2.5 km ($T = T(2.5)$.

Figure C.1 further helps to understand the implication of computing temporal mean in two different ways. Two idealised and linearly decreasing mass-flux profiles (M_1 and M_2) belong to two different instances of time ($t = 1$ and $t = 2$). M_1 has its 0-dBZ ETH lower than M_2. The red dashed line results from computing the mean if M_1 is excluded from the data set above its 0-dBZ ETH. The blue dashed line is the mean mass-flux if M_1 is included at all heights and considered zero above its 0-dBZ ETH.

It has to be noticed that when analysing temporal mean quantities different from area fraction and mass-flux, the method explained here (blue line) has some limitations. For example the quantity $\frac{1}{M}\frac{\partial M}{\partial z}$, used to characterise mass-flux shape and entrainment rates, can only be defined inside the convection, where $M > 0$. Also from a physical point of view, is has little meaning to define fractional entrainment where no clouds occur.

C.1 Results

(a) RH_{500}

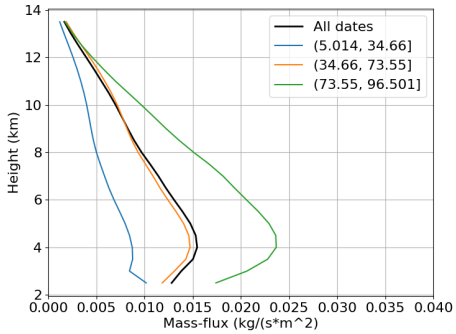

(b) CAPE

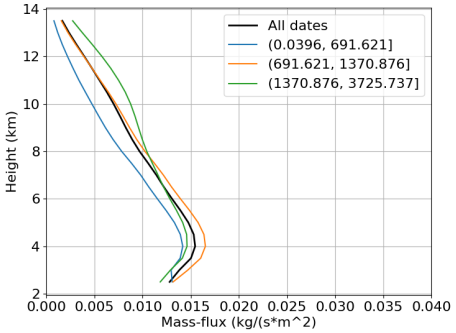

(c) CIN

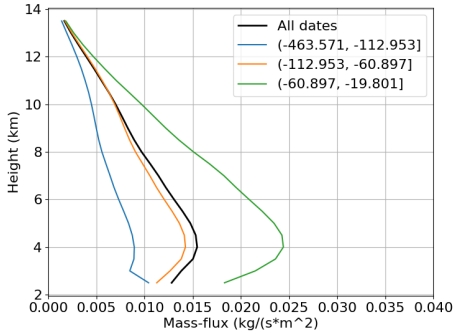

(d) Ω_{500}

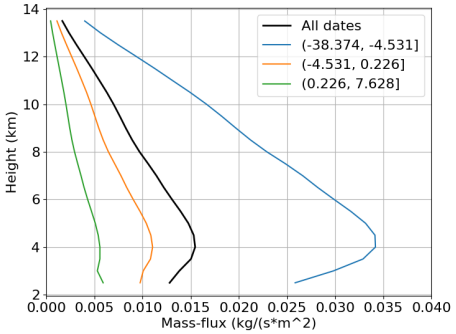

(e) $\overline{\chi_{\text{crit}}}$

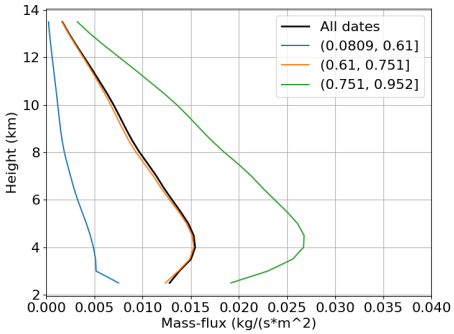

FIGURE C.2. How environmental parameters affect mean bulk mass-flux profiles.

(a) RH_{500}

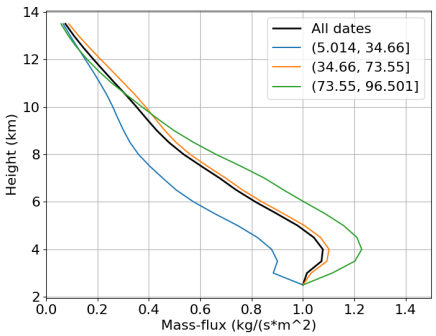

(b) CAPE

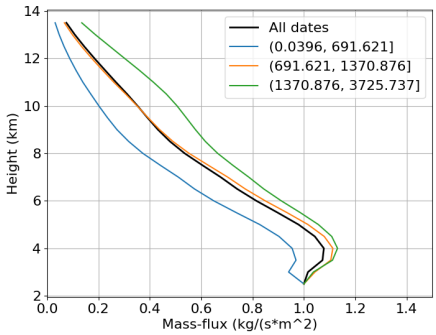

(c) CIN

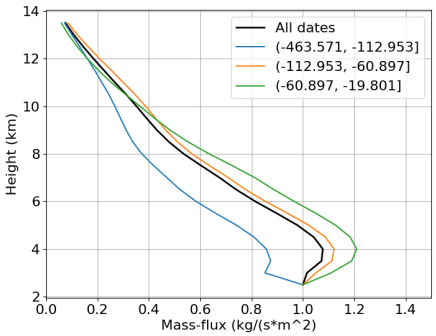

(d) Ω_{500}

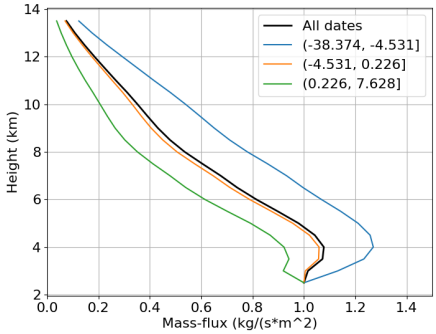

(e) $\overline{\chi_{\text{crit}}}$

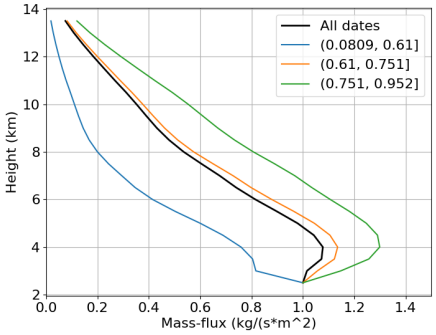

FIGURE C.3. How environmental parameters affect mean bulk nondimensionalized mass-flux profiles.

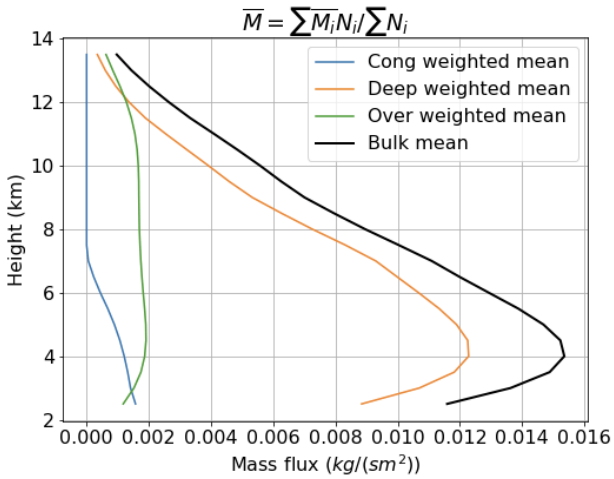

FIGURE C.4. Mean relative contribution of cloud sub-ensembles to mean bulk mass-flux profile when weighting factor is constant with height.

BIBLIOGRAPHY

Arakawa, A. (2004).
The cumulus parameterization problem: Past, present, and future.
Journal of Climate, 17(13):2493–2525.

Arakawa, A., Schubert, W. H., Arakawa, A., and Schubert, W. H. (1974).
Interaction of a Cumulus Cloud Ensemble with the Large-Scale Environment, Part I.
Journal of the Atmospheric Sciences, 31(3):674–701.

Bechtold, P., Bazile, E., Guichard, F., and Mascart, P. (2001).
A mass-flux convection scheme for regional and global models.
Quarterly Journal of the Royal Meteorological Society.

Böing, S. J., Siebesma, A. P., Korpershoek, J. D., and Jonker, H. J. (2012).
Detrainment in deep convection.
Geophysical Research Letters.

Carter, D. A., Gage, K. S., Ecklund, W. L., Angevine, W. M., Johnston, P. E., Riddle, A. C., Wilson, J., and Williams, C. R. (1995).
Developments in UHF lower tropospheric wind profiling at NOAA's Aeronomy Laboratory.
Radio Science.

Casey, S. P. F., Fetzer, E. J., and Kahn, B. H. (2012).
Revised identification of tropical oceanic cumulus congestus as viewed by CloudSat.
Atmospheric Chemistry and Physics, 12(3):1587–1595.

Davies, L., Jakob, C., May, P., Kumar, V. V., and Xie, S. (2013).
Relationships between the large-scale atmosphere and the small-scale convective state for Darwin, Australia.
Journal of Geophysical Research Atmospheres, 118(20):11534–11545.

De Lavergne, C., Palter, J. B., Galbraith, E. D., Bernardello, R., and Marinov, I. (2014).
Cessation of deep convection in the open Southern Ocean under anthropogenic climate change.
Nature Climate Change.

de Rooy, W. C., Bechtold, P., Fröhlich, K., Hohenegger, C., Jonker, H., Mironov, D., Pier Siebesma, A., Teixeira, J., and Yano, J. I. (2012).
Entrainment and detrainment in cumulus convection: An overview.
Quarterly Journal of the Royal Meteorological Society, 139(670):1–19.

de Rooy, W. C., Siebesma, A. P., de Rooy, W. C., and Siebesma, A. P. (2008).
A Simple Parameterization for Detrainment in Shallow Cumulus.
Monthly Weather Review, 136(2):560–576.

Derbyshire, S. H., Beau, I., Bechtold, P., Grandpeix, J. Y., Piriou, J. M., Redelsperger, J. L., and Soares, P. M. (2004).
Sensitivity of moist convection to environmental humidity.
Quarterly Journal of the Royal Meteorological Society.

En.climate-data.org (2012).
Web Page.

Giangrande, S. E., Toto, T., Jensen, M. P., Bartholomew, M. J., Feng, Z., Protat, A., Williams, C. R., Schumacher, C., and Machado, L. (2016).
Convective cloud vertical velocity and mass-flux characteristics from radar wind profiler observations during GoAmazon2014/5.
Journal of Geophysical Research: Atmospheres, 121(21):12,891–12,913.

Grabowski, W. W. and Smolarkiewicz, P. K. (1999).
CRCP: a Cloud Resolving Convection Parameterization for modeling the tropical convecting atmosphere.
Physica D: Nonlinear Phenomena, 133(1-4):171–178.

Hartigan, J. A. and A., J. (1975).
Clustering algorithms.
Wiley.

Hartigan, J. A. and Wong, M. A. (1979).
Algorithm AS 136: A K-Means Clustering Algorithm.
Applied Statistics, 28(1):100.

Houghton, H. G. and Cramer, H. E. (1951).
A THEORY OF ENTRAINMENT IN CONVECTIVE CURRENTS.
Journal of Meteorology.

Johnson, R. H., Ciesielski, P. E., and Hart, K. A. (1996).
Tropical inversions near the 0°C level.
Journal of the Atmospheric Sciences, 53(13):1838–1855.

Johnson, R. H., Rickenbach, T. M., Rutledge, S. A., Ciesielski, P. E., Schubert, W. H., Johnson, R. H., Rickenbach, T. M., Rutledge, S. A., Ciesielski, P. E., and Schubert, W. H. (1999).
Trimodal Characteristics of Tropical Convection.
Journal of Climate, 12(8):2397–2418.

Kain, J. S., Fritsch, J. M., Kain, J. S., and Fritsch, J. M. (1990).
A One-Dimensional Entraining/Detraining Plume Model and Its Application in Convective Parameterization.
Journal of the Atmospheric Sciences, 47(23):2784–2802.

Keenan, T., Glasson, K., Cummings, F., Bird, T. S., Keeler, J., Lutz, J., Keenan, T., Glasson, K., Cummings, F., Bird, T. S., Keeler, J., and Lutz, J. (1998).
The BMRC/NCAR C-Band Polarimetric (C-POL) Radar System.
Journal of Atmospheric and Oceanic Technology, 15(4):871–886.

Khairoutdinov, M. F. and Randall, D. A. (2001).
A cloud resolving model as a cloud parameterization in the NCAR Community Climate System Model: Preliminary results.
Geophysical Research Letters, 28(18):3617–3620.

Kim, D. and Kang, I. S. (2012).
A bulk mass flux convection scheme for climate model: Description and moisture sensitivity.
Climate Dynamics.

Kumar, V. V., Jakob, C., Protat, A., May, P. T., and Davies, L. (2013).
The four cumulus cloud modes and their progression during rainfall events: A C-band polarimetric radar perspective.
Journal of Geophysical Research: Atmospheres, 118(15):8375–8389.

Kumar, V. V., Jakob, C., Protat, A., May, P. T., and Williams, C. R. (2015).
Mass-Flux Characteristics of Tropical Cumulus Clouds from Wind Profiler Observations at Darwin, Australia.
Journal of the Atmospheric Sciences, 72(5):1837–1855.

Kumar, V. V., Protat, A., Jakob, C., and May, P. T. (2014).
On the Atmospheric Regulation of the Growth of Moderate to Deep Cumulonimbus in a Tropical Environment.
Journal of the Atmospheric Sciences, 71(3):1105–1120.

Kumar, V. V., Protat, A., Jakob, C., Williams, C. R., Rauniyar, S., Stephens, G. L., and May, P. T. (2016).
The estimation of convective mass flux from radar reflectivities.
Journal of Applied Meteorology and Climatology, 55(5):1239–1257.

Kumar, V. V., Protat, A., May, P. T., Jakob, C., Penide, G., Kumar, S., and Davies, L. (2012).
On the Effects of Large-Scale Environment and Surface Types on Convective Cloud Characteristics over Darwin, Australia.
Monthly Weather Review, 141(4):1358–1374.

Labbouz, L., Kipling, Z., Stier, P., Protat, A., Labbouz, L., Kipling, Z., Stier, P., and Protat, A. (2018).
How Well Can We Represent the Spectrum of Convective Clouds in a Climate Model? Comparisons between Internal Parameterization Variables and Radar Observations.
Journal of the Atmospheric Sciences, 75(5):1509–1524.

Louf, V., Jakob, C., Protat, A., Bergemann, M., and Narsey, S. (2019a).
The Relationship of Cloud Number and Size With Their Large-Scale Environment in Deep Tropical Convection.
Geophysical Research Letters, 46(15):9203–9212.

Louf, V., Protat, A., Warren, R. A., Collis, S. M., Wolff, D. B., Raunyiar, S., Jakob, C., Petersen, W. A., Louf, V., Protat, A., Warren, R. A., Collis, S. M., Wolff, D. B., Raunyiar, S., Jakob, C., and Petersen, W. A. (2019b).
An Integrated Approach to Weather Radar Calibration and Monitoring Using Ground Clutter and Satellite Comparisons.
Journal of Atmospheric and Oceanic Technology, 36(1):17–39.

Majda, A. J., Khouider, B., Peters, K., Jakob, C., and Davies, L. (2013).
Stochastic Behavior of Tropical Convection in Observations and a Multicloud Model.
Journal of the Atmospheric Sciences, 70(11):3556–3575.

May, P. T., Mather, J. H., Vaughan, G., Jakob, C., McFarquhar, G. M., Bower, K. N., and Mace, G. G. (2008).
The Tropical warm pool international Cloud Experiment.
Bulletin of the American Meteorological Society.

Mcfarlane, N. (2011).
Parameterizations: representing key processes in climate models without resolving them.
Ltd. WIREs Clim Change, 2:482–497.

Moorthi, S. and Suarez, M. J. (1992).
Relaxed Arakawa-Schubert: a parameterization of moist convection for general circulation models.
Monthly Weather Review.

Morton, B. R., Taylor, G. I., and Turner, J. S. (1956).

Turbulent gravitational convection from maintained and instantaneous sources.
Proceedings of the Royal Society of London. Series A. Mathematical and Physical Sciences.

Penide, G., Kumar, V. V., Protat, A., May, P. T., Penide, G., Kumar, V. V., Protat, A., and May, P. T. (2013).
Statistics of Drop Size Distribution Parameters and Rain Rates for Stratiform and Convective Precipitation during the North Australian Wet Season.
Monthly Weather Review, 141(9):3222–3237.

Plant, R. S. and Craig, G. C. (2008).
A stochastic parameterization for deep convection based on equilibrium statistics.
Journal of the Atmospheric Sciences.

Posselt, D. J., van den Heever, S. C., and Stephens, G. L. (2008).
Trimodal cloudiness and tropical stable layers in simulations of radiative convective equilibrium.
Geophysical Research Letters, 35(8):L08802.

Riehl, H. and Malkus, J. S. (1958).
On the heat balance in the Equatorial trough zone.
Geophysica.

Rockel, B. (2015).
The Regional Downscaling Approach: a Brief History and Recent Advances.
Current Climate Change Reports, 1(1):22–29.

Sherwood, S. C., Ingram, W., Tsushima, Y., Satoh, M., Roberts, M., Vidale, P. L., and O'Gorman, P. A. (2010).
Relative humidity changes in a warmer climate.
Journal of Geophysical Research, 115(D9):D09104.

Shutts, G. and Pallarés, A. C. (2014).
Assessing parametrization uncertainty associated with horizontal resolution in numerical weather prediction models.
Philosophical Transactions of the Royal Society A: Mathematical, Physical and Engineering Sciences.

Steiner, M., Houze, R. A., Yuter, S. E., Steiner, M., Jr., R. A. H., and Yuter, S. E. (1995).
Climatological Characterization of Three-Dimensional Storm Structure from Operational Radar and Rain Gauge Data.
Journal of Applied Meteorology, 34(9):1978–2007.

Tiedtke, M. (1989).
A comprehensive mass flux scheme for cumulus parameterization in large-scale models.
Monthly Weather Review.

Wagner, T. M. and Graf, H. F. (2010).
An ensemble cumulus convection parameterization with explicit cloud treatment.
Journal of the Atmospheric Sciences.

Warner, J. (1955).
The Water Content of Cumuliform Cloud.
Tellus.

Whiteman, C. D., Eisenbach, S., Pospichal, B., and Steinacker, R. (2004).
Comparison of vertical soundings and sidewall air temperature measurements in a small alpine basin.
Journal of Applied Meteorology.

Williams, C. R. (2012).
Vertical Air Motion Retrieved from Dual-Frequency Profiler Observations.
Journal of Atmospheric and Oceanic Technology, 29(10):1471–1480.

Xie Shaocheng, Cederwall Richard T., and Zhang Minghua (2004).
Developing long-term single-column model/cloud system–resolving model forcing data using numerical weather prediction products constrained by surface and top of the atmosphere observations.

Yano, J. I. (2010).
Downscaling, parameterization, decomposition, compression: A perspective from the multiresolution analysis.
Advances in Geosciences.

Yano, J.-I. (2014).
Formulation structure of the mass-flux convection parameterization.
Dynamics of Atmospheres and Oceans, 67:1–28.

Yoshimura, H., Mizuta, R., and Murakami, H. (2015).
A spectral cumulus parameterization scheme interpolating between two convective updrafts with semi-lagrangian calculation of transport by compensatory subsidence.
Monthly Weather Review.

Zhang, M. H. and Lin, J. L. (1997).
Constrained variational analysis of sounding data based on column-integrated budgets of mass, heat, moisture, and momentum: Approach and application to ARM measurements.

Journal of the Atmospheric Sciences.